Droplet Microfluidic Systems for Directed Evolution: Aiming at Integration

André Pereira Rodrigues de Faria

(Thesis to obtain the Master of Science Degree in)

Bioengeneering and Nanosystems

Supervisors
Dr. João Pedro Estrela Rodrigues Conde
Dr. Lígia Maria de Oliveira Martins

Examination Committee

Chairperson: Gabriel António Amaro Monteiro
Supervisor: Dr. João Pedro Estrela Rodrigues Conde
Member of the Committee: Dr. Luís Humberto Viseu Melo

November 2018

Contents

Agradecimentos

Em primeiro lugar quero agradecer ao Professor João Pedro Conde pela oportunidade de poder fazer parte deste projecto. Quero agradecer também todo o acompanhamento, prontidão e entusiasmo que partilhou; e à grande abertura que sempre manteve para que eu pudesse experimentar e errar ao longo desta investigação! Quero agradecer também à Professora Lígia Martins pelo seu entusiasmo e disponibilidade para me acompanhar neste projeto, que cada vez caminha mais perto da parte biológica. Ao Guilherme Andrade por todo o caminho que debravou neste projecto, possibilitando-me avançá-lo muito mais rapidamente. A minha sincera gratitude ao INESC-MN, à Dr. Virgínia Chu, aos meus colegas e engenheiros de processo por toda a autonomia dada para poder aprender a construir cada parte deste projeto. Um grande agradecimento em especial aos colegas do grupo: Ruben Soares, InêsPinto, Denis Santos, Eduardo Brás, Ricardo Fradique, Catarina Bombaça e Catarania Caneira, Pebro Monteiro, Tiago Pestana, Tatiana Arriaga, pelo ambiente de entreajuda que todos os dias criam. Pelas suas enormes disponibilidades para ajudar, tirar dúvidas, ensinar e partilhar que sempre tiveram para comigo e todos os alunos desta instituição. Um grande agradecimento ao meu colega Rui Pinto por toda a ajuda e persistência que teve para resolver comigo os misticismos da eletrónica que pareciam não ter solução. Quero agradecer ao IST, por todo o conhecimento que me passou, pelas experiências que proporcionou, pelos excelentes professores que tive. Aos meus colegas que me acompanharam na minha Licenciatura e Mestrado, quero agradecer por toda a ajuda que me deram neste percurso. Quero agradecer aos meus amigos, desde os mais antigos aos mais recentes que sempre tornaram tudo mais leve. Em especial ao Rui Carvalho por todos os momentos que partilhámos, ao Tom Monteiro por sempre me saber escutar quando precisei, ao Siqian Hu por me acompanhar desde quando nem português falava, e ao Zé Luís por ser ele mesmo. Ao Nuno Carvalho que me deu a mão e tanto me ajudou, Obrigado! quero agradecer-te também por teres contribuído para a minha mudança de rumo para este mestrado que tanto me fez feliz. À Sêmele Balduino por toda a dedicação, aprendizagem e por todo o apoio que me deu na transição para este mestrado. Ao Kwenda Lima agradeço-te por tudo o que me tens dado! À Sara, à Graça e agora à Maria, obrigado por todos os momentos partilhados :) A toda a minha família, tias, tios, primos e primas, tantos e tão bons! que sempre me apoiaram no meu percurso, Obrigado! Em especial um Enorme Obrigado à minha Mãe Maria Pereira, ao meu Pai José Faria, ao meu Tio João Ramos e à minha Tia Dolores que incansavelmente todos os dias de tantas maneiras me apoiam de uma maneira incrível!

Resumo

Evolução dirigida veio para ficar. A prova disso é a atribuição do Prémio Nobel da Quimica este ano. Modificações do genoma podem criar enormes bibliotecas que exigem sistemas ultra rápidps de triagem. este trabalho contribui para o desenvolvimento de um sistema de gotas microfluidico integrado para triagem. Vários modulos são necessários: nomeadamente: geração de gotas, detecção e separação. Dois tipos de plataformas de separação foram estudados: pneumatica e electrica por dielectrophorese. Foram comparados electrodos planares e tri-dimensionais. Duas novas geometrias de electrodos 3D foram implementadas com sucesso. Foi construído um circuito de alta voltage alternada (700 V_{pp} em frequencia de kHz) . Foi implementada deteção por photoconductores de a-Si:H filme fino, e foi também desenvolvido um circuito amplificador de transimpedancia. Para contagem e tamanho das gotas foi desenvolvido um script de análise de imagem. Integração de separação electrica e deteção por photoconductores de filme fino foi implementada e respectivos delays foram characterizados, havendo ainda alguns desafios em aberto para tornar o sistema robusto.

Palavras-chave: Microfluídica de gotas, DEP, Photosensores, Integração, Evolução Dirigida.

Abstract

Directed evolution came to change the world. And its proof is the Nobel Prize in Chemistry this year. Genome variations may create huge libraries that ask for high-throughput screening systems. This work contributes to the development of an integrated droplet based microfluidic system. Several modules are required, namely: droplet generation, detection and sorting. Here two different sorting platforms were studied for a flow focusing droplet generator: pneumatic and dielectrophoresis (DEP) based. Planar and three-dimensional electrode's geometries were compared. Two novel 3D electrodes designs were implemented with success. A circuit to power the electrodes with high voltage (700 V_{pp}) and high frequency (till hundreds of kHz) was built. Droplet detection using a-Si:H thin film photoconductors was implemented, also with custom made transimpedance amplifier circuit. Image analysis script was developed to count and measure droplets from microscope recording. Electrical sorting and detection by photoconductors was implemented, with system delays characterized, but still some challenges were left open.

Keywords: Droplet microfluidics, DEP, Photosensors, Integration, Directed Evolution.

Acronyms

CM   Clausius-Mossoti function

DAC   Digital to Analog Converter

DEP   Dielectrophoresis

DI-water   Deionized water

DNA   Deoxyribonucleic Acid

EWOD   Electrowetting-on-Dielectric

FACS   Fluorescence Activated Cell Sorter

HVAC   High Voltage AC Circuit

IPA   Isopropanol

MPC   model predictive control

Op-amp   Operational Amplifier

PBS   Phosphate Buffer Solution

PCR   Polymerase Chain Reaction

PDMS   Polydimethylsiloxane

PGMEA   Propylene glycol methyl ether acetate

SNR   Signal to Noise Ratio

RIE   Reactive Ion Etching

RF   Radio Frequency

TIA   Transimpedance Amplifier

UV   Ultra Violet

List of Figures

Chapter 0

Motivation and Project Organization

This Project aims the design of a microfluidic integrated system for enzyme directed evolution. The project born to attend the challenge made by the Microbial an Enzyme Technology group at Instituto de Tecnologia Química e Biológica (ITQB) to the Thin Film MEMS and BioMEMS group at Instituto de Engenharia de Sistemas e Computadores - Micro e Nano Fabricação (INESC-MN), for an high-throughput screening and low cost microfluidic platform to study directed evolution. I was immediately fascinated by the possibility of working in a project that will help investigators to perform their work more efficiently with affordable costs. And I also enjoy study things in motion, droplets suited like a glove!
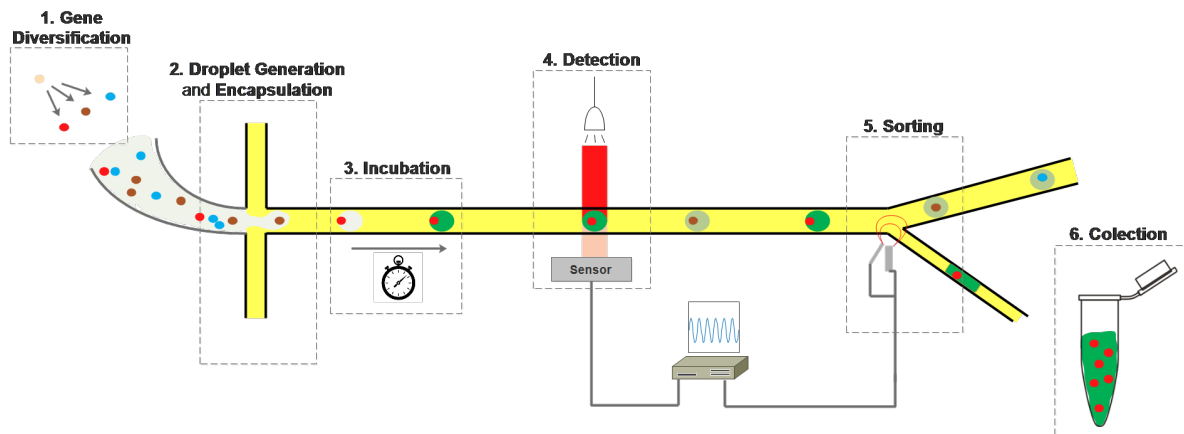
Figure 1: Overall view of an integrated droplet's microfluidic system to perform directed evolution.

Figure 1 illustrate the different modules required for a droplet microfluidic system for directed evolution. (module 1) First a gene library has to be created; (module 2) cells should be injected into microfluidic channels and encapsulated in individual reactors, droplets; (module 3) the desired reaction will take some time, changing some measurable droplet's characteristic; (module 4) screening is done by optical, electrochemical or other method, to infer if the mutation produced noticeable differences compared to the wild type; some date processing will occur till (module 5) droplet sorting; (module 6) genetic information is kept, inserted into cells and the process starts again. Segmenting this multidisciplinary system in modules facilitates the development process. There are three main microfluidic modules: droplet formation and cell encapsulation, detection, and sorting. Because droplets can be much bigger than cells like *E.coli* (40-100 μm *vs* 1 μm), droplet generation, detection and sorting can be studied without cells, not compromising the system integrity. The previous Master student, Guilherme Andrade[1], had already studied and characterized droplet generation, perform cell encapsulation and demonstrated the applicability of thin film photosensors for droplet detection. It was clear that the next steps would be sorting, followed by solidifying detection module and then integrate both. This was the proposal and goal for my contribution into the project.

Chapter 1

State of the Art

1.1 Directed Evolution

Directed evolution (Figure 1.1) has proved to be an effective strategy for improving or altering the activity of biomolecules for research, therapeutic and industrial applications[2]. Genetic diversity is the start base for natural and laboratory evolution. The rate of spontaneous mutation is generally a slow process, and thus not suitable on producing sufficient genetic variance for laboratory evolution. Depending on the desired library of gene variants, several methods are available. In order to have feedback of each gene mutation, genes and gene products should be manipulated in a coupled manner, which requires carefully designed strategies for screening and/or selecting functional variants[2]. These approaches aren't restricted to proteins, they could be used for other biomolecules. Proteins have a crucial role in our body, making them useful for generating novel therapeutics, biocatalysts and reagents[2].
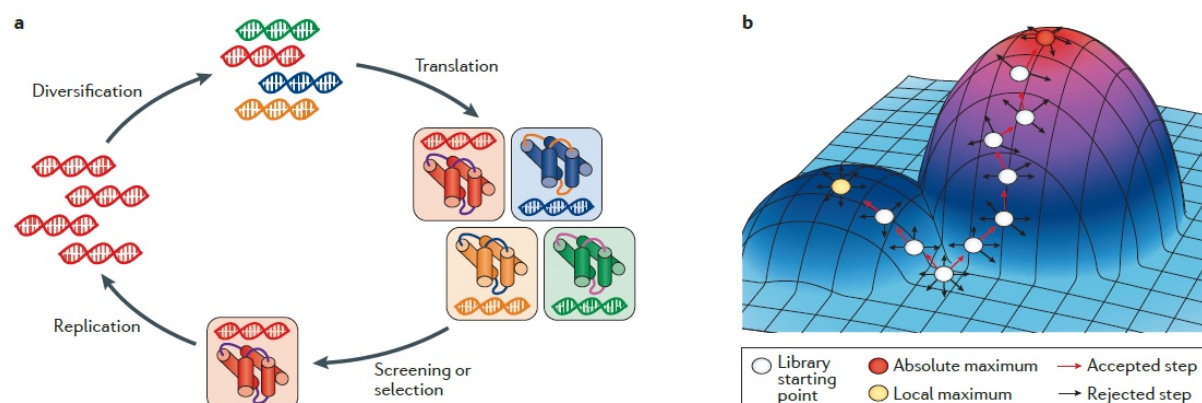
Figure 1.1: (a) Key steps in the cycle of directed evolution, mimicking natural evolution, a diverse library of genes is translated into a corresponding library of gene products which after screening enable to select functional variants. These functional genes are replicated and serve as starting points for next iteration. (b) Conceptual visualization of directed evolution iterative process of maximization of a desired activity. Local maximums can trap the process, if large libraries are not created. Figure reproduced[2].

Different strategies to approach mutagenesis are chosen depending on the application and level of knowledge on the protein behavior[2].
Rational Design. If information about protein struture and function is well known, just by changing one amino-acid at a specific location may improve a activity, binding or other desired spec[3].
Random mutagenesis. Many times the information available about how the protein activity will change with a variant is hard to predict. In these case random mutagenesis is absolutely necessary[2]. Chemical and physical agents could be use to damage DNA, alkylating compounds such as ethyl methanesulfonate (EMS)[4], deaminating compounds such as nitrous acid[5], base analogues such as 2-aminopurine[6], and ultraviolet irradiation[7] are some examples. Some attention should be taken, in order to choose methods that don't have much bias in the mutation spectrum[4, 5]. A non-chemical approach that offers more control on the mutation rate is the error-prone PCR. As mutations accumulate during each PCR cycle,

it's possible to increase the average number of mutations per clone by increasing the number of cycles. All these approaches, specially the random one, create huge libraries of variants that have to be screened. A mere peptide with 10 amino acids yields $21\ aminoacids^{10\ positions} \sim 10^{13}$ different combinations. Directed evolution needs to access the gene which is associated with the phenotype that induced the desired change. Spatial separation of individual mutants preserves the linkage between phenotype and genotype. It is broadly compatible with many assay techniques (optical, nuclear magnetic resonance, liquid and gas chromatography, mass spectroscopy) making in principle any enzymatic activity screenable.
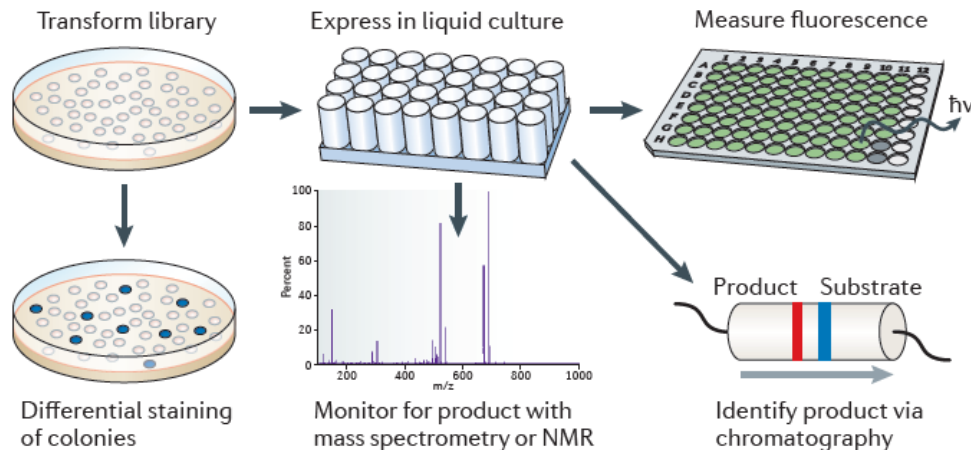
Figure 1.2: Clonally isolated variants are screened as colonies on solid media, or as wells in liquid culture. Fluorescent, chemiluminescence colorimetric reporters are measured by automated microtitre plate readers. Alternatively, lysates can be screened for product formation using chromatography, mass spectrometry or nuclear magnetic resonance (NMR). Figure reproduced[2].

Spacial separation has practical throughput limit of $\sim 10^4$ library members per screening round, which constitutes a time constrain (Figure 1.2). Automated setups, with robotic help work around the tedious workload of these screens (for all the combinations of a 10 peptide it would be 1000 millions of rounds!), still a limitation is kept, bellow 1 μl volumes evaporation and capillary forces become prohibitive to microplate readers[8].

Flow cytometry offers one of the highest capacities of any screening method, achieving up to 10^8 library members screened in < 24 hours [9, 10]. This method rather than separating the clones, starts from a bulk solution of clones and analyses each cell, relying on cell wall or membrane to maintain genotype-phenotype association. This raises some problems if the desired molecules/proteins are extracellular, because some other label should be used to quantify the expression, and due to the possibility of inhomogeneities in the biomolecules medium concentration potentially interfering with gene expression.

Droplet microfluidics works with volumes from nL to pL (thousand times lower that with microplates), at kHz rate, although one order slower than the state-of-art FACS[11]) offers more flexibility and compartmentalizes all the cell's products inside each droplet, creating microreactor for each genotype and respective phenotype.

1.2 Microfluidics

1.2.1 Physics and Dimensionless numbers

Liquid-liquid two-phase microflows are well characterized with incompressible continuity equation for both disperse and continuous phase fluids:

$$\nabla \cdot u_s = 0 \tag{1.1}$$

Where u is the velocity vector and the subscript "s" denotes either disperse, "d", or continuous, "c", phase fluid. The momentum is the Navier-Stokes equation of incompressible Newtonian fluids:

$$\rho_s \frac{\partial \boldsymbol{u_s}}{\partial t} + \rho_s \boldsymbol{u_s} \cdot \nabla \boldsymbol{u_s} = -\nabla p_s + \eta_s \nabla^2 \boldsymbol{u_s} + \boldsymbol{f_s} \tag{1.2}$$

3

Where t denotes time, ρ the fluid density, p the pressure, η the dynamic shear viscosity and f the body force vector per unit of volume. The left side of Equation 1.2 describes time-dependent, $\rho_s \frac{\partial u_s}{\partial t}$, and convective inertial accelerations, $\rho_s u_s \cdot \nabla u_s$, terms. On the right side is the term for diffusion $\eta_s \nabla^2 u_s$ - which is the divergence of viscous stresses $\sigma_s = \eta[\nabla u_s + (\nabla u_s)^T]$, pressure difference, $-\nabla p_s$, and external field forces f_s (gravity, electrical, magnetic, centrifugal). Several interfacial boundary conditions should be imposed: Continuity of normal velocity at the imiscible interface[12]

$$u_d \cdot n = u_c \cdot n \tag{1.3}$$

where n is unit normal vector outward to the interface.
Continuity of the tangential viscous stress, and the normal stress is balanced by capillary pressure:

$$\sigma_d \cdot t = \sigma_c \cdot t \tag{1.4}$$
$$T_d \cdot n - T_c \cdot n = -\gamma k n \tag{1.5}$$

where γ is the interface tension.
As several forces have a role on droplet microfluidic, their relative contribution will describe the behavior of this system, thus six dimensionless numbers will characterize the relative predominance of these forces (Table 1.1)

Table 1.1: Dimensionless parameters in droplet microfluidics.

Symbol	Name	Expression	Physical meaning
Re	Reynolds number	$Re_s = \frac{\rho_s u_s L}{\eta_s}$	inertial force/Viscous force
Ca	capillary number	$Ca_s = \frac{\eta_s u_s}{\gamma}$	viscous force/interfacial tension
We	Weber number	$We_s = \frac{\rho_s u_s^2 L}{\gamma}$	inertial force/interfacial tension
Bo	Bond number	$Bo = \frac{\Delta \rho g L^2}{\gamma}$	buoyancy/interfacial tension
λ	viscosity ratio	$\lambda = \frac{\eta_d}{\eta_c}$	dispersed viscosity/continuous viscosity
ϕ	flow rate ratio	$\phi = \frac{Q_d}{Q_c}$	dispersed flow rate/ continuous flow rate

Reynolds number Re represents the relative importance of inertia to viscous force, usually ranges $10^{-6} - 10$ in microfluidic flows.

$$Re_s = \frac{\rho_s u_s L}{\eta_s} \tag{1.6}$$

Where L denote the characteristic length, usually use the hydraulic diameter[12]. Capillary number Ca is the ratio of viscous stress to capillary pressure

$$Ca_s = \frac{\eta_s u_s}{\gamma} \tag{1.7}$$

The ratio between inertia and capillary pressure yield the Weber number We

$$We_s = \frac{\rho_s u_s^2 L}{\gamma} \tag{1.8}$$

The relative importance of gravity (being g the gravity acceleration) to capillary pressure is described by the Bond number Bo

$$Bo = \frac{\Delta \rho g L^2}{\gamma} \tag{1.9}$$

The viscosity ratio λ and the flow rate ratio ϕ of disperse to continuous phase fluid are also relevant numbers

$$\lambda = \frac{\eta_d}{\eta_c} \tag{1.10}$$

$$\phi = \frac{Q_d}{Q_c} \tag{1.11}$$

1.2.2 Materials and technology

Different materials can be used for microfluidic devices. From glass to polymers, the choice should consider certain aspects as: easyness of fabrication, cost, optical and mechanical properties and bio-compatibility[13]. For its optical transparency in the visible, bio-compatibility and low complexibility of fabrication, PDMS is widely used in microfluidic prototipage[14]. PDMS is a viscoelestic organic polymer of the silicone family (structure in Figure 1.3) that can be process by soft lithography tecniques. Depending on the quality of the process sub-micron resolution could be achieved[15].
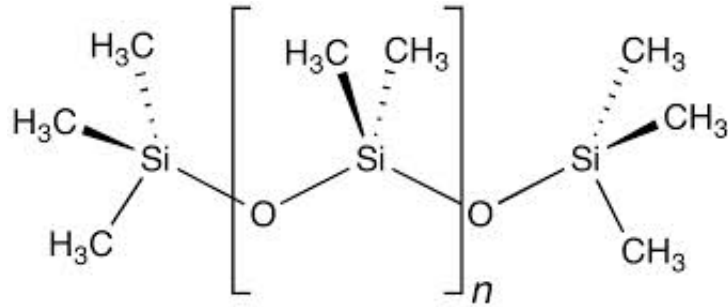
Figure 1.3: Chemical structure of PDMS.

1.2.3 Digital microfluidics

Digital microfluidic, droplets, are a key feature of the microfluidic systems. They occur when shear stress is capable of breaking interfacial tension. They're generation rate, size and distribution, stability to avoid coalescence, or not, immiscibility with the continuous phase, are features that will influence and be influenced by the first stage of these systems: droplet generator. Depending on the fact of using or not external forces to give and energy input in promoting interfacial instabilities at the droplet generation, the methods are classified as active or passive.
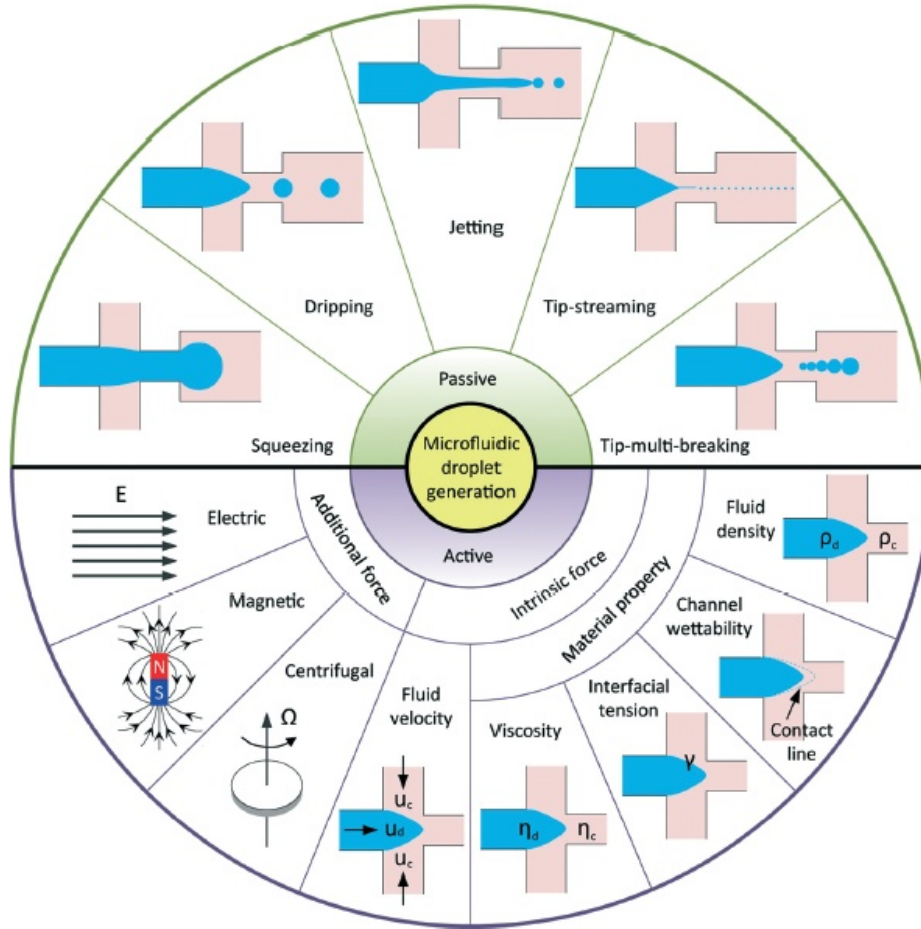
Figure 1.4: Schematic of active and passive methods in droplet generation microfluidics. In passive methods, depending on the relative proportion of capillary, viscous, and inertial forces different modes of droplet generation arise: squeezing, dripping, jetting, tip-streaming and tip-multi-breaking. Active control for droplet generation apply external forces from electrical, magnetic and centrifugal fields, or modify forces by tuning fluid velocity and material properties such as viscosity, interfacial tension, channel wettability and fluid density. Figure reproduced[12].

Active techniques offer more control modulating droplet formation with the aid of addition energy, than just by the pressure applied by syringe pumps in passive techniques[12]. Apart the advantage of a faster response time, active methods are indispensable in some extreme applications as breaking fluid threads in aqueous two-phase systems (ATPS) with ultra-low interfacial tension[16], producing droplets from highly viscous liquids[17], and on demand droplet generation, for example, to encapsulate cells in a deterministic way[18]. Those forces could be electrical, magnetic, sonora, centrifugal. But also intrinsic parameters as flow velocity, profile and material properties will give control over the droplet formation process (Figure 1.4).

In passive devices, the introduction of an immiscible fluid into another leads to different droplet formation modes(Figure 1.4): squeezing[19], dripping[20], jetting[20], tip-streaming[21] and tip-multi-breaking[22].

1.2.4 Generator geometries

Transversal to both active and passive droplet generation methods, microfluidic geometries will influence droplet breaking off. The three most frequently used geometry types are: cross-flow, co-flow and flow-focusing[12]. The others employ variations of channel confinement: step emulsification, microchannel emulsification and membrane emulsification[12].
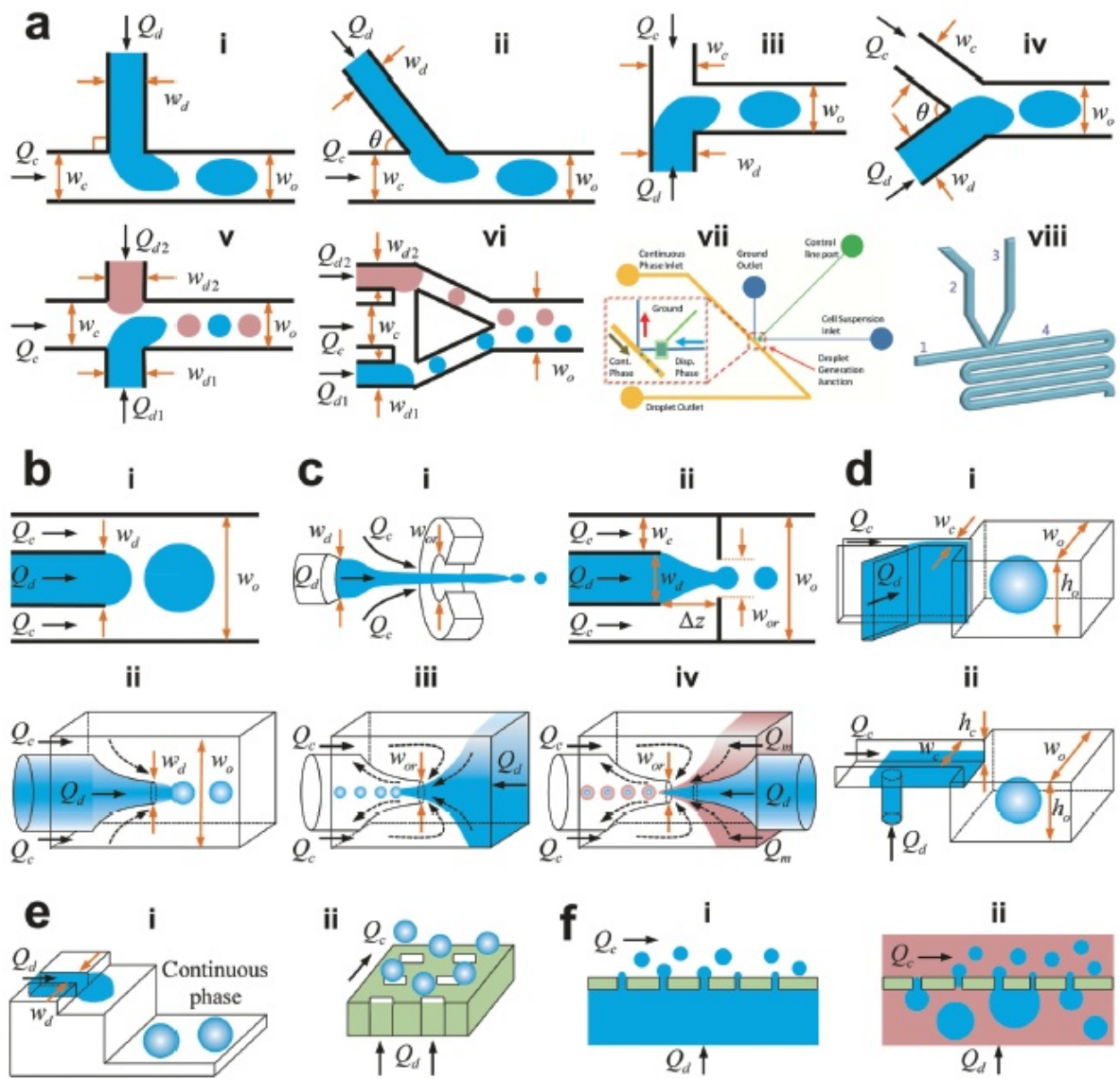
Figure 1.5: Schematics of microfluidic device geometries (not to scale). (a) Cross-flow geometries: (i) T-junction. (ii) T-junction with intersection angle different from 90°. (iii) "Head-on" geometry. (iv) Y-shaped junction. (v) Double T-junction that produces droplets at the same location. (vi) Double T-junction that produces droplets at different locations. (vii) "K-junction". (viii) "V-junction". (b)Co-flow (i) Quasi-2D planar co-flow. (ii) 3D co-flow. (c) Flow-focusing. (i) Axisymmetric geometry. (ii) Planar geometry. (iii) Microcapillary flow-focusing device. (iv) Microcapillary device combining co-flow and flow-focusing geometries. (d) Step emulsification. (i) Horizontal step. (ii) Vertical step.(e) Microchannel emulsification. (i) Grooved-type microchannel. (ii) Straight-through microchannel. (f) Membrane emulsification. (i) Direct membrane emulsification. (ii) Premix membrane emulsification. Q, w, h, and Δz denote the volumetric flow rate, channel width, channel height, and horizontal distance from the end of the disperse microchannel to the orifice entrance, respectively. The subscripts "c", "d", "o", and "or" stand for the continuous phase, disperse phase, outlet channel, and orifice, respectively. Figure reproduced [12].

Cross-flow

In cross-flow geometries, continuous and disperse phase meet at an angle $0° < \theta < 180°$ (Figure 1.5-a,i-iv)). Many variations are used, but T-junctions are the most frequently implemented, they have a coefficient of variations, CV[1], of droplet radius usually less than 2 %. Double T-junctions are also used to create a stable alternation of droplets with different compositions[23] (Figure 1.5-a,v), and the size ratio

---

[1]CV, is defined as the ratio of standard deviation to the mean of droplet radius

between droplets could also be controlled[24] (Figure 1.5-a,vi). Other conformations as K-junctions[25, 26] (Figure 1.5-a,vii) and V-junctions[27, 28] (Figure 1.5-a,viii) are also used to meet some requirements as frequency, a size of droplets in biological assays.

Co-flow

In co-flow geometry, the continuous and disperse phase fluids meet in parallel streams. Configurations could be quasi 2D (Figure 1.5-b,i) or having radial symmetry[29](Figure 1.5-b,ii). The dispersion on droplet size in co-flow geometries depends on the flow conditions: in dripping mode, monodispersity is high ($CV < 3$ %[30]); and in jetting mode are polydisperse[20]).

Flow-focusing

Flow focusing devices are better to achive smaller droplets[12]. The geometry is similar to the co-flow, with the addition of a constriction. They could also be categorized in 2D and 3D symmetry[12] (Figures 1.5-c,ii and c,i), the 3D configuration has the advantage of avoiding issues like wetting of the channel walls by the disperse phase, and thus producing monodisperse droplets ($CV < 5\%$) with higher throughputs[31]. Other configurations for the flows, where the disperse phase flows in opposite direction to the continuous phase flow, meeting at a narrow orifice, also produces monodisperse multiple emulsions in a single step[29, 32] (Figures 1.5-c,iii and a,iv).

Step, microchannel and membrane emulsifications

Step emulsification (Figures 1.5-d,i and d,ii) have the highest monodispersity ($CV < 1\%$ for step and $CV < 0.1\%$ for a gradual transition in channel high[33]), and also it's less sensitive to flow rate fluctuations[12].

Microchannel emulsification forces the disperse phase through the inlet channel and then droplets form at the end of the channel. These geometries can be divided into two groups[34, 35] grooved-type microchannel (Figures 1.5-e,i) and straight-through microchannel (Figure 1.5 e,ii). To achieve high-throughput, microchannel arrays are usually implemented[36].

Membrane emulsification (Figures 1.5-f,i and f, ii) enables a huge parallelization of droplet generation, but, because many factors take role -pore morphology, size, spacial arrangement; surface wettability; material properties of fluids; and dynamic parameters- mono-dispersity is hard to achieve (CV$\sim$ 20%)[37].

1.2.5   Passive droplet generation

In passive methods, the two-phase flows are controlled by either syringe pumps that supply constant flow rates or pressure regulators[38].

Five fundamental modes of droplet generation have been observed in droplet generators: squeezing, dripping[30], jetting [39], tip-streaming[19] and tip-multi-breaking[22].

To the present date, the first three have been observed in cross-flow, co-flow, and flow-focusing geometries; the last two have not been reported in cross-flow yet[12].
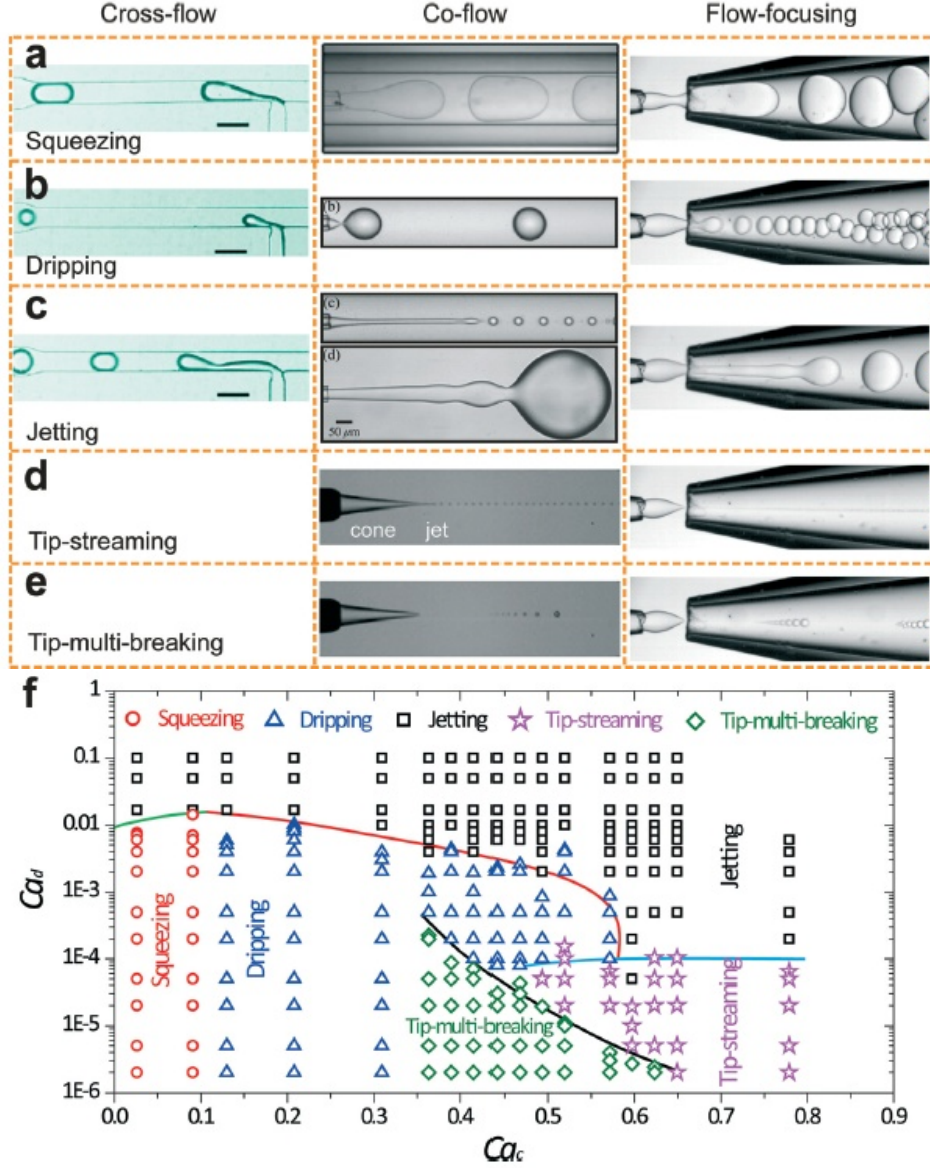
Figure 1.6: Different modes in passive droplet generation, with different geometries: cross-flow, co-flow and microcapillary flow-focusing. (a) Squeezing mode. (b) Dripping mode. (c) Jetting mode. (d) Tip-streaming mode. (e) Tip-multi-breaking mode. Neither tip-streaming nor tip-multi-breaking modes have been reported in cross-flow geometry. (f) Phase diagram in Capillary numbers for continuous and disperse phase plane (Ca_c, Ca_d) for various modes observed in microcapillary flow-focusing devices. Figure Reproduced[12].

Squeezing

Droplets generated with squeezing mode are larger than the channel dimension and highly monodisperse (Figure 1.6-a)). This regime occurs at low capillary number ($Ca_c < O(10^{-2}$ in T-junctions)[12].

Dripping

Dripping regime generates droplets just a bit smaller than channel dimension and monodisperse (Figure 1.6-b)). The squeezing dripping transition was found to occur $Ca_c \sim O(10^{-2}$[12] (Figure 1.6-f)).

Jetting

In jetting, droplets are polydisperse (Figure 1.6-c)). This regime occurs by increasing either the continuous or disperse fluid flow rate, dripping to jetting transition can occur, where disperse liquid extends

through the common channel and breaks up into droplets at the end of the jet due to Rayleigh–Plateau instability[20].

Tip-streaming

Tip-streaming regime can generate droplets as small as submicrometer-scale and monodisperse (Figure1.6-d)). To this mode four conditions are sufficient[40]: no flow separation should exist between the continuous flow and the drop interface, requiring creeping flow condition, $Re_c \ll 1$. In order to stretch the disperse fluid into a conical shape, the continuous-fluid viscous stress must overcome the capillary pressure at the injection nozzle, requiring $Ca_c > Ca_{cri}$ [2]. For the extremely thin jet form at the tip of the cone, $\phi \ll 1$ should be maintained. The final condition $Re_d \ll 1$ ensures that the average disperse velocity equals continuous velocity in the thin jet region due to large momentum diffusion, assuring almost cylinder form for the fine jet after the cone[12].

Tip-multi-breaking

In tip-multi-breaking, droplets come out polydisperse but in sequence, a geometric-progression in size (Figure 1.6-e)). Transitions between different modes can be achieved by changing disperse and/or continuous phase capillary numbers[12].

1.2.6 Active droplet generation

Active droplet generation methods[3] offer additional handles and higher flexibility in the control of droplet size and production rate(in passive methods is almost impossible to independently control both, as they are correlated by mass balance[12]). Also the system response time, the time needed for stabilized droplet production is much shorter in active control than in passive method (can be down to several milliseconds in an active approach compared with several seconds or even minutes in a passive method).
The addition input energy could come in different ways: electric, magnetic and centrifugal; and by modifying the intrinsic inertial, viscous and capillary forces. The mechanism of active control could be different even for the same energy input[12].
In **electrical control** for example, electrowetting effect could be used by competition between electrical stresses and surface tension[41]. Other effects like dielectrophoresis, electrochemical, electrocapillary and electrorheological can be used[12]. **Magnetic control** takes advantage of ferrofluids (coloidal systems with magnetic particles) to control droplet generation with the applied fields [12]. The **centrifugal control** will require much attention to the microfluidic design, as the applied force is always radial to the axis of rotation, but has the advantage of potential avoiding syringe and pressure pumps[42]. **Optical control** with laser pulse could be used to locally increase pressure by inducing cavitation bubbles at high rates (10 kHz) with high monodispersity ($CV < 1$ %)[43]. **Mechanical control** could be implemented on-chip (microvalves, piezoelectric actuation) and off-chip (also with valves or with mechanic vibration thru the disperse phase microtubing)[12]. One could also control the system by **material properties control**, interfacial tension could be controlled by thermal, optical and electrical regulation; and channel wettability could vary with the use of photosensitive surfactants, or with applied electrical field[12]. As passive methods guarantee appropriate droplets volumes for directed evolution (<50 pL) with small dispersion (1-3 %), and require simpler setups, the project should base on those generation methods.

1.2.7 Single cell encapsulation

In a single-fluid phase, the environment is controlled at a global scale, but is not controllable in the immediate vicinity of an individual cell[18]. Droplet microfluidics systems provide a natural barrier to diffusion (oil-water interface). Even with significant concentration gradients dilution is minimized[18].

For passive encapsulation methods, the droplet occupancy by cell is statistical, characterized by the Poisson distribution

$$p(k, \lambda) = \frac{\lambda^k e^{-k}}{k!} \tag{1.12}$$

---

[2]Ca_{cri} is a critical constant of the order of unity

[3]This work will not focus on explaining with detail the working principle of each active generation strategy, but gives a general idea on the available possibilities, potential advantages and limitations. This because this types of control increase the complexity of the system, and the kind of control that they add is not needed yet.

where k is the number of particles in a droplet and λ the product between the concentration of cells in the pre-encapsulation solution with the average droplet volume. This distribution has the form showed in Figure 1.7. In order to minimize the number of droplets with more than one cell, low values of λ should be used. To obtain 98% of droplets with one cell $\lambda = 0.05$ meaning that on 5% of droplet will have cells. If the goal is to maximize the number of droplets with one cell, $\lambda = 1$ should be chosen, but even in this case only $\sim 58\%$ droplets will have cells, being just 36% containing one cell. Some times the cell waste may be a secondary concern, the volumes involved are at the pico and nano liter scale, but the time spent producing wasted droplets reduce maximum throughput by at least an order of magnitude[18].
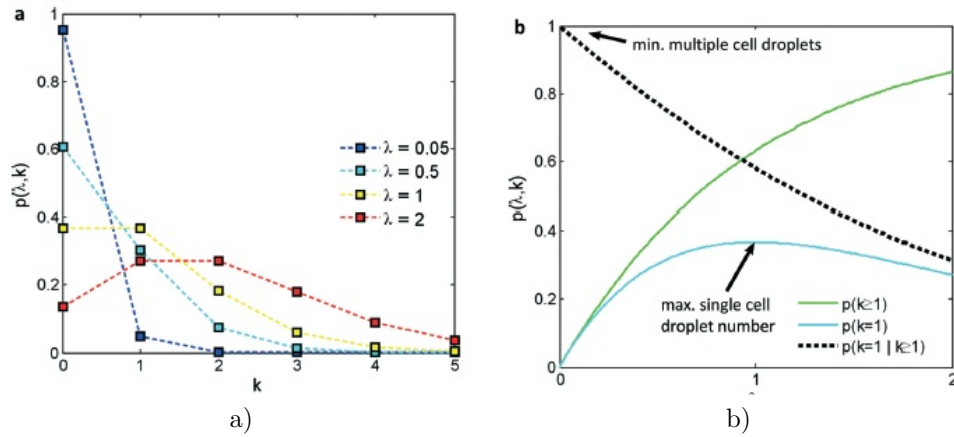
Figure 1.7: (a) Poisson distribution p(λ, k) for cell distribution in droplets. Different distributions of droplets containing a given number of cells k for discrete values of λ. (b) Droplet proportion containing at least one cell, $p(k \geq 1)$, exactly one cell, $p(k \geq 1)$, and the proportion of droplets containing cells that contain exactly one, $p(k = 1|k \geq 1)$. Single cell throughput is maximised when $\lambda = 1$, where only ~ 58 % of droplets with cells and ~ 36 % of all droplets will contain only one cell. Figure reproduced[18].

There are many methods[18] (dielectrophoresis, traveling and standing acoustic wave, optical trapping) that can detect the number of cells in each droplet, and sort by this criteria, but those do not avoid the time wasting problem. Inertial ordering (Figure 1.8) doesn't obey to Poisson distribution, thus distribution of one cell per droplet up to 80 % are achievable[44]. Has a strong restriction, requires high flow rates (velocities of the order $\sim 0.1 - 1ms^{-1}$, corresponding to 2 kHz-12 kHz generation rate) which can limit other microfluidic processes, or at least requires some strategies to avoid those limitation.
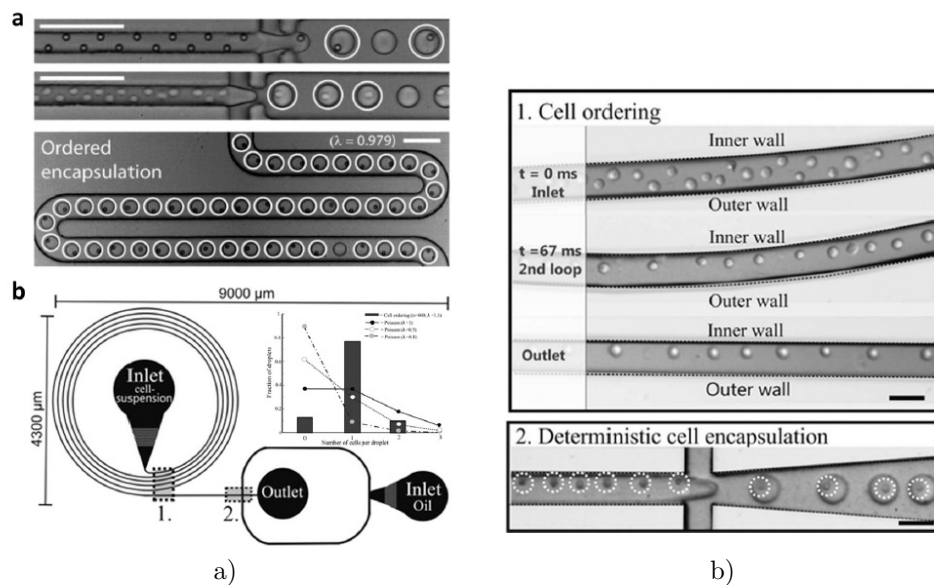
Figure 1.8: Inertial ordering microfluidic devices to encapsulate single cell, using (a) straight or (b) curved microchannels. Particles can be focused at discrete locations laterally and ordered longitudinally. Scale bars denote (a)100 μm and (b)50 μm. Figures reproduced[44].

1.3 Sorting methods applied to droplet microfluidics

In contrast to passive sorting, based on hydrodynamic features, active sorting methods allow on-demand droplets control. Similar to active droplet generation, many different strategies can be used: electrical, magnetic, pneumatic, acoustic and thermal (Figure 1.9-a)). Figure 1.9-b) compares those strategies according to six performance categories: response time and throughput, ease of fabrication, cost of the experimental setup, accuracy and selectivity, device lifetime, and dependence on the droplet size. In the scale 5 represents the highest score, bigger areas correspond to overall better performances. Two oustand, electric for its fast response time and throughput, and pneumatic for its great biocompatibilirty. Magnetic control has a big drawback due to the need for magnetic materials, either on fluid or in droplets, causing potential biocompatibility problems[45]. Thermal methods explore the advantage of thermocappilary effects on microscale, either by heating up the liquid reducing its hydraulic resistance or using a laser beam to block droplets passage[45]. Acustic control have good biocompatibility and can steer liquid plugs[4][46]. Its major drawback is the complexity on implementation[45].
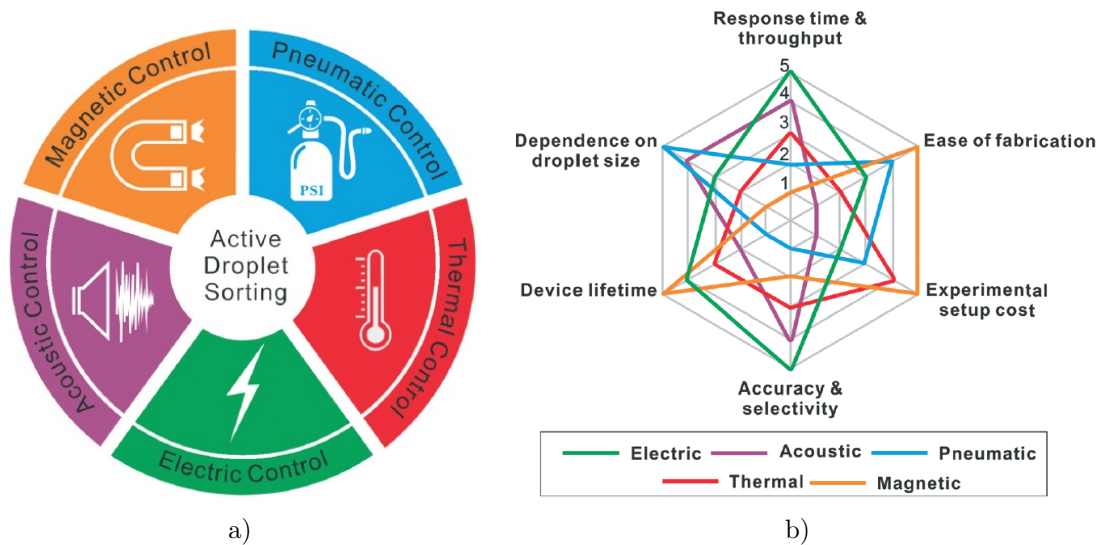
Figure 1.9: a) Classification of the different active droplet sorting methods. b) Schematic to compare among different active methods of droplet sorting. Figures reproduced[45]

1.3.1 Electrical

Electric methods typicaly have very fast actuation times, at the order of microseconds. They can be classified according to the type of current applied to the electrodes (either direct current, DC, or alternating current, AC)[45].

---

[4]Liquid plugs are defined as large droplets in contact with all four wall of a microchannel.
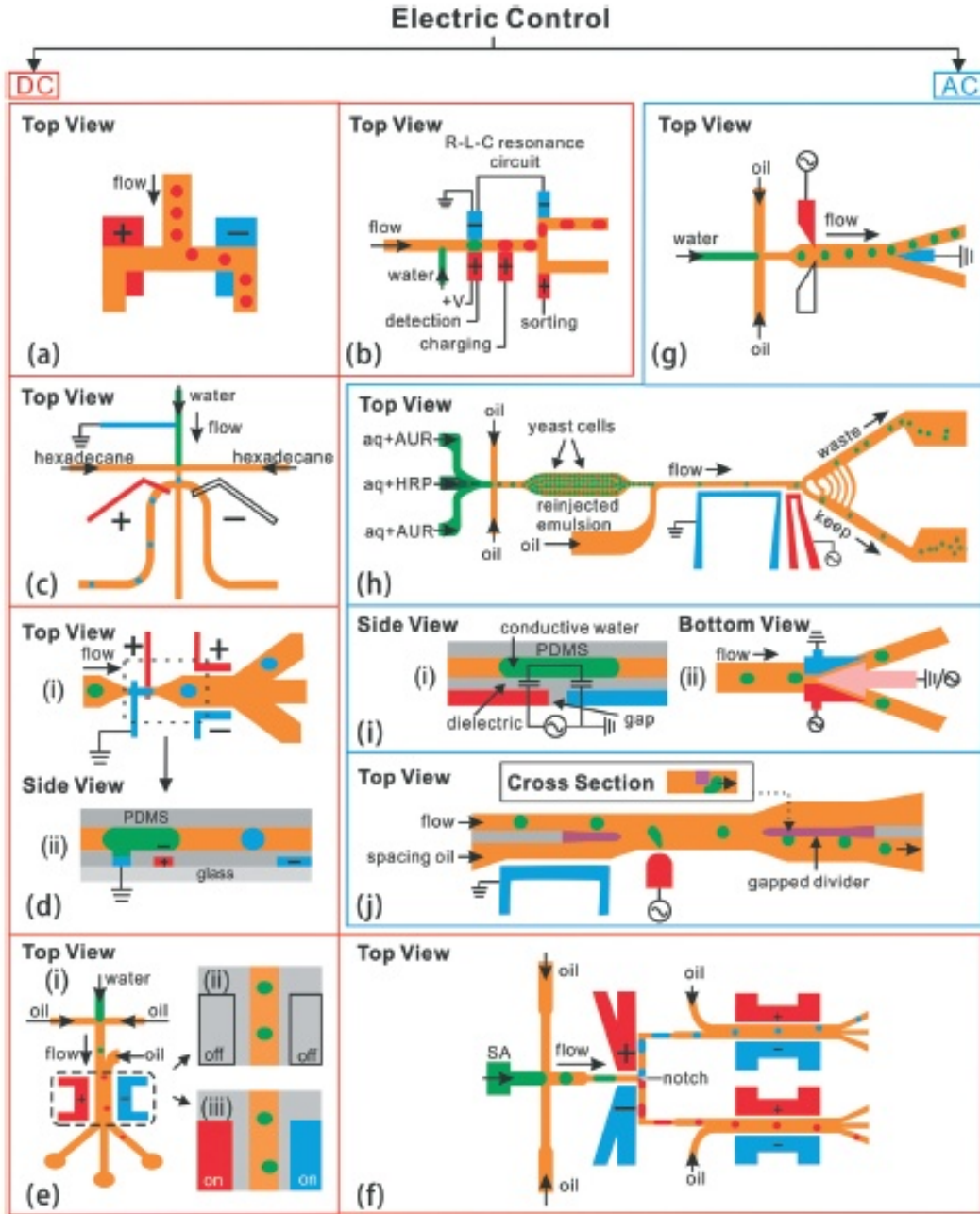
Figure 1.10: Schematic sketches and classification (direct and alternating current, DC and AC) of droplet sorting with electric methods. The orange and green parts represent oil and aqueous phases, respectively. The green droplets are electrically neutral, blue and red droplets are negatively and positively charged, respectively. For the DC/AC electric field, the red and blue electrodes represent positive and negative/-grounded charging, respectively. Inactive electrodes are blank. Figure reproduced[45].

Direct current

For charged droplets, a positive and a negative electrodes are sufficient to sort them[47] (Figure 1.3.1-a). The applied force, $\boldsymbol{F}$, could easy be estimated in terms of the electrode distance, d, by the relations eqs. (1.13) and (1.14).

$$|\boldsymbol{E}| = \frac{V}{d} \tag{1.13}$$

$$\boldsymbol{F} = q\boldsymbol{E} \tag{1.14}$$

With $\boldsymbol{E}$, being the applied electrical field to the droplet with charge q. Requiring droplets positively or negatively charged is a restriction, but if the droplets are subjected to an energized electrode, they acquire positive surface charge allowing to sort with simple electrodes (Figure 1.3.1-b). A not so useful strategy for direct evolution, combines both electrical droplet generation and sorting[48] (Figure 1.3.1-c). Other geometries for pre-charging of droplets are also possible[49](Figure 1.3.1-d). A phenomena called "droplet self-charging" can be used to sort droplets[50] (Figure 1.3.1-e), there has been no consensus on the mechanism behind this phenomena, droplets became positively charged and deflect to the negative side. A very useful design is to fabricate the electrodes in a three dimensional way using microfluidic channels filled with molten silver paste[51](Figure 1.3.1-f), this avoids alignment problems, and the electrical field is stronger and more homogeneous along the channel height.

Alternating current: Dielectrophoresis

AC electrical field can be used in droplet sorting taking advantage of dielectrophoresis (DEP), no charged particle is needed. The force is caused by the induction of an electrical dipole, $\boldsymbol{m}$ that will be actuated by a spacial non-uniform field. The force is given by

$$\boldsymbol{F} = \boldsymbol{m} \cdot \nabla \boldsymbol{E} \tag{1.15}$$

For a spherical particle of radius r, with electrical conductivity $sigma_p$ and electrical permittivity ϵ_p^*, inside a medium with electrical conductivity $sigma_m$ and electrical permittivity ϵ_m^* the conventional[5] dielectrophoresis force based on classical Maxwell theory is given by Equation 1.16[52].

$$\boldsymbol{F_{DEP}} = 2\pi r^3 \epsilon_m Re[f_{CM}] \nabla \boldsymbol{E}_{rms}^2 \tag{1.16}$$

The force shows dependence on the particle size, r^3 term, with the medium and particle materials at a given frequency, $\epsilon_m Re[f_{CM}]$, and with the gradient of the squared Electric field, $\nabla \boldsymbol{E}_{rms}^2$, if AC is the root mean squared field. $Re[f_{CM}]$ is the real part of the Clausius-Mossoti function given by Equation 1.17.

$$f_{CM}(\omega) = \frac{\epsilon_p^* - \epsilon_m^*}{\epsilon_p^* + 2\epsilon_m^*} \tag{1.17}$$

Where the complex permittivities, dependent of electric field angular frequency ω, are described by Equation 1.18.

$$\epsilon^* = \epsilon - j\frac{\sigma}{\omega} \tag{1.18}$$

When designing the electrodes, strong gradient fields are desired. DEP force was first reported for droplet microfluidic sorting in 2006[53] using metal electrodes (Figure 1.3.1-g). But similar to previous examples, strategy of using microfluidic channels with liquid metal can be used -avoiding alignment issues, and field loss through height-[54] (Figure 1.3.1-h) . Also metal electrodes could be substituted in some case by salt solutions (NaCl 5 M) and used in similar geometries (some capacitance effects should be taking in account when designing the electrodes channels). Taking in advantage the microfluidic part, designing a gap divider for DEP sorting allow the highest sorting rate reported ($\sim 30\ kHz$)[55, 56, 57] (Figure 1.3.1-j). At lower sorting rates (100 Hz-1.2 kHz) electrowetting-on-dielectric, EWOD, could be implemented for droplet microfluidics (Figure 1.3.1-i).

1.3.2 Pneumatic

Pneumatic sorting is based on channel deformation, having good bio-compatibility, but high sorting rates are hard to achieve with precision, and durability is low due to the deterioration of the membranes[45].

---

[5]Conventional refer to neglecting the electrorotation term. This term refer to a rotational torque created if the electric field rotates at the same angular velocity that the particle does[52].
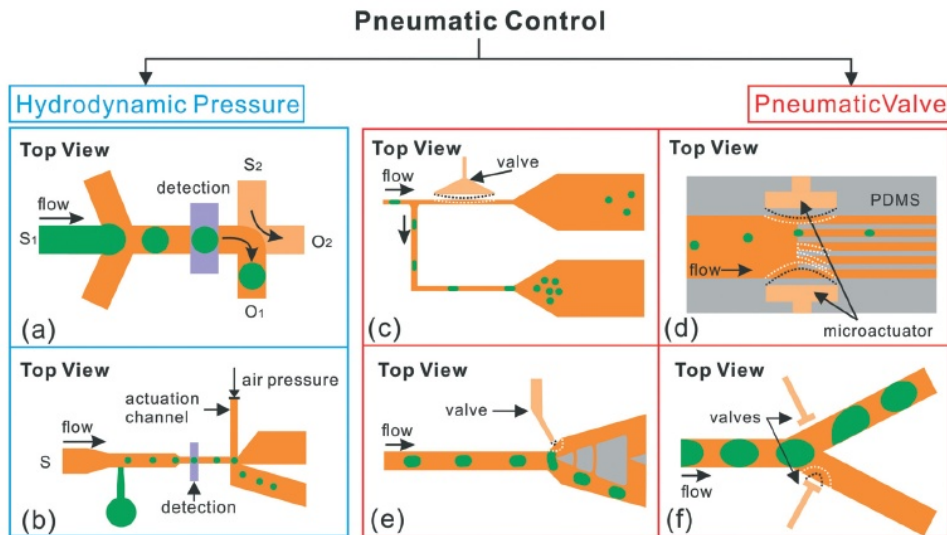
Figure 1.11: Schematic with classification of droplet sorting with pneumatic control. The orange parts represent oil fluid and the green parts represent aqueous fluid. The deformation of valves and that of channels are represented by black and white dotted lines, respectively. (a) Hydrodynamic gating occurs by connecting outlet 1 (O1) and outlet 2 (O2) to a negative pressure system. The relative pressure ratio will sort the droplets. (b) Target droplets are sorted to the lower collection channel when the air pressure is increased. (c) Single-layer valve is at one branch of the sorter with a flexible elastomeric membrane separating two microchannels. (d) Four parallel walls separate the main channel into five sampling channels and two microactuators are patterned at two sides, The proportion on the actuation of each actuator will determine which channel receives the droplet; (e) Single-layer membrane valve consisting of an air channel almost touching one of the channels bifurcation. (f) PDMS walls deformed by pneumatic pressures. Figure Reproduced[45].

Pneumatic actuation could be performed by imposing an external pressure, where a fluid will be pumped into/out the channels deflecting the droplets[58, 59] (Figures 1.3.2-a,b); or by the implementation of membrane valves, taking in the advantage of PDMS elasticity[60, 61, 62] (Figures 1.3.2-c,d,e). Lateral valve fabrication has some constriction on the design (because channels cannot cross each others) but avoids complexity in the fabrication process due to the requirement of multilayers[45].

1.4 Detection

Detection is a core element of the integrated system. It will influence the throughput ability of droplet processing, as to sort droplets they will have bo screened first by a detection method. Impedance based sensors can be use to detect droplets, they are easy to fabricate but requires electrodes in direct contact with the solution, making reusability more difficult. Also detection frequency has some limitations, ranging from Hz till almost 100 Hz[63]. Optical detection overcomes speed limitation.Absorbance, chemiluminescence or fluorescence can be used to detect droplets. High speed cameras can be couplet to microscope, covering droplet frequency range (from Hz to tens of kHz) and not requiring direct contact with droplet system. They have a big disadvantage in cost[63]. Thin film photosensors can be easily miniaturized to droplets dimension and can be arrayed giving spacial resolution[64]. They do not require direct contact with fluids but alignment is required.

Chapter 2

Materials and Methods

In this chapter are described the different fabrication techniques used to fabricate all the devices developed for the project, and the setups used to study each part. Some setups were created or modified to optimize conditions, for those cases the explanation is on the Results and Discussion section. Three different type of structures were built, microfluidic channels, planar and 3D electrodes. Four different types of study were performed with different setups: droplet generation, electrical sorting, pneumatic sorting and detection with photosensor.

André Pereira Rodrigues de Faria

Supervisors:

João Pedro Estrela Rodrigues Conde

Lígia Maria de Oliveira Martins

2.1 Fabrication

2.1.1 Microfluidic

All the microfluidic structures used in his work were built using PDMS made by soft lithography methods. The fabrication of a microfluidic structure can be described in five main steps: design, hard mask fabrication, mold fabrication, PDMS casting and sealing. Figure 2.1 exemplifies the process overview.
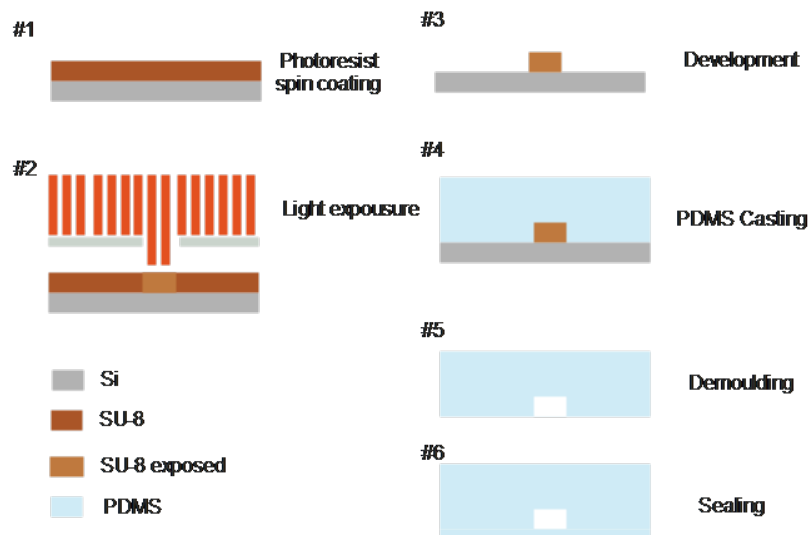
Figure 2.1: Process overview of microfluidic mold and PDMS channel fabrication.

Design

All microfluidic structures, and also the electrodes, were designed using AutoCAD® software. The design is bi-dimensional, with closed polylines.

Hard mask fabrication

Substrates of glass 5 cm × 5 cm were used for mask fabrication - transparency required - with useful dimensions 4 cm × 4 cm due to handling and process limitations. Substrates were clean firstly rinsed with DI-water, acetone, IPA, DI-water, followed by a 20 min Alcanox® solution bath at 65°C, then rinsed with DI-water and dried with compressed air.

The following steps were performed inside a class 10 cleanroom. 200 nm Al deposition by sputtering in Nordiko 7000. 1.5 μm of positive photoresist (PFR7790G) was spin coated on top of Al layer and backed at 85°C for 60 s. Then was patterned by exposing to 442 nm using Heidelberg DWL II (direct write laser lithography equipment), followed by a 60 s bake at 110 °C and 30 s cool down. Developing solution (TMA 238 WA) was applied on the sample for 60 s reaction, stopped with DI-water, and then dried. Wet etching process is used to pattern the Al layer, the sample is immersed for few minutes into Al etchant (Tecnietcg Al80) to remove the areas that don't have photoresist. The process can be paused or stopped by washing the sample with IPA followed by DI-water. The photoresist is removed with acetone followed by IPA and DI-water. Process is similar to electrode fabrication differing just on the type of etching (here is wet, for electrodes is RIE), and can be seen on Figure 2.2.

Mold fabrication

The mold is made on top of 5 cm × 5 cm Si substrates. Substrates were clean firstly rinsed with DI-water, acetone, IPA, DI-water, followed by a 20 min Alcanox® solution bath at 65°C, then rinsed with DI-water and dried with compressed air. Oxigen plasma treatment at level high for 5 min 800 mTorr, Harrick Plasma PDC-002-CE, is used to improve adhesion of the following layer. The mold determine the microfluidic channel height. Inside a laminar flow hood, SU-8 50 (Michrochem) was spin coated (Laurel WS-650-23); each height requires specific (see Table 2.1) time, rpm and aceleration, followed by proper pre-bake time (for solvent evaporation) and soft bake (solidify the film). The Hard mask is placed on top of the SU-8 sample, Al facing the SU-8 -minimizes light difraction- and then exposed to UV light (inducing the polymerization and hardening of the exposed polymer). The hard mask is removed and the SU-8 sample goes to a post-expousure bake followed by development by immersion in PGMEA 99 % solution. The process can stopped by rinsing with IPA. After assuring proper development by optical inspection a 150 °C hard bake for 15 min is performed. The height is measured on a profilometer (Tencor Alpha-Step 200).

Table 2.1: Parameters for SU-8 50 mold fabrication.

Height (μm)	Spinner		Pre-bake
	step 1	step 2	
39.97 ± 0.02	500 rpm 100 rpm/s, 10 s	2300 rpm 300 rpm/s, 37 s	3 min 65 °C + 8 min 95 °C
99.7 ± 0.5	500 rpm 100 rpm/s, 10 s	100 rpm 300 rpm/s, 33 s	10 min 65 °C + 30 min 95 °C

Height (μm)	Exposure	Pos-bake
$40 \pm xx$	18 s	1 min 65 °C + 7 min 95 °C
$100 \pm xx$	43 s	1 min 65 °C + 10 min 95 °C

PDMS casting and sealing

Microfluidic structures consists in two parts: one with the channels and a another to seal against. The part with with the channels was fabricated by pouring PDMS (SYLGARD 184 silicon elastomer kit) -mixed 1:10 with reticulate agent and degased in vaccum chamber- over the SU-8 mold. The PDMS was left to polymerize in an oven at 70 °C for 90 min, then peeled off from the mold. The holes for inlets and outlets are punched with a blunt needle. The structures that were not used with sensors, the other part was a PDMS membrane of 2-3 mm thick made by the same procedure above. For the ones that integrate with sensors, to reduce at maximum the optical path between the bottom of the channel and the sensor, a $100\mu m$ thick glass coverslip is spin coated on both sides[1] with 3.56 ± 0.14 μm PDMS membrane (recipie in Table 2.2).

---

[1]Note that one side will ensure symmetry in the channel, walls floor and ceiling made of PDMS; and the other prevents photosensor scracthing.

Table 2.2: Parameters for PDMS covered glass coverslip.

Height (μm)	Spinner			Bake
	step 1	step 2	step 3	
3.56 ± 0.14	500 rpm 100 rpm/s, 15 s	3000 rpm 500 rpm/s, 30 s	6000 rpm 1200 rpm/s, 4 min	15 min 150 $^\circ C$

Both parts of the structure were treated with oxygen plasma 60 s, level high, 800 mTorr, and immediately pressed to each other.

2.1.2 Planar Electrodes

Microfluidic structures that were used to perform droplet sorting had integrated electrodes. Electrode fabrication and integration of can be divided in four main steps: design, metal deposition and patterning, PCB mounting and wire bonding, alignment and sealing. The Design part is as described in Section 2.1.1-Design.

Metal Deposition and Patterning

Substrates of glass[2] 5 cm × 5 cm were cleaned using the same protocol as in Section 2.1.1-Hard Mask Fabrication, followed by oxigen plasma treatment[3] at level high for 5 min 800 mTorr, Harrick Plasma PDC-002-CE. Inside cleanroom class 10, a 145 ± 2 nm layer of TiW ($\rho = 253.37$ $\mu\Omega.cm$) was deposited at Nordiko 7000. Then a lithography process by DWL (similiar as described in Section 2.1.1-Hard Mask Fabrication) protects the TiW areas that will contain the electrodes. Followed by a reactive ion etching (RIE) with $SF_6 + CHF_3$ for 300 s (etch rate ~ 0.6 nm/s) to remove all the TiW that don't form the electrodes. To remove the photoresist, an acetone bath is enough, followed by DI-water. Overall process is exemplified on Figure 2.2.
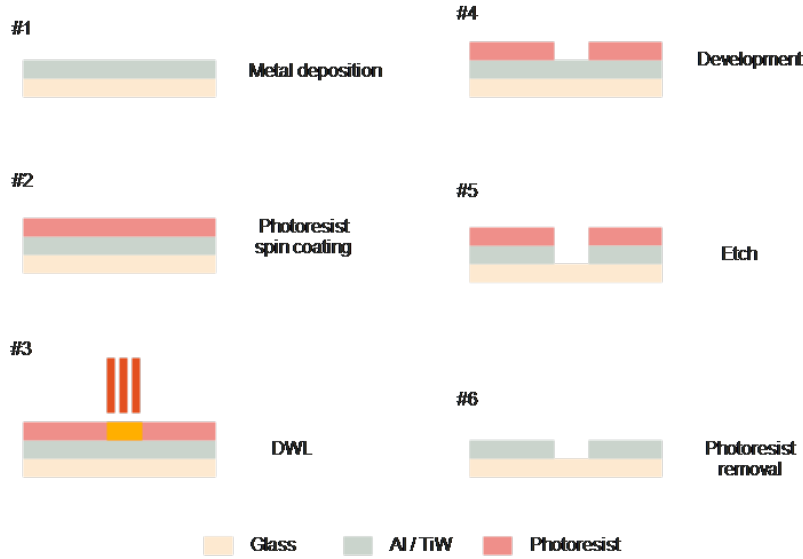
Figure 2.2: Fabrication scheme of TiW electrodes and AL mask

PCB mounting and wire bonding

With the electrodes patterned on glass, they are ready to be mounted in a PCB that will enable to communicate with the AC High voltage supply. The glass substrate was fixed to the PCB with cyanoacrylate glue, and after drying, wire bonding (Al 40 μm diameter) was performed between TiW and PCB pads. To protect the wires, a silicon layer was poured on top of the wires. As could be seen in Figure 2.3

---

[2]Glass was chosen due to non conductive properties.

[3]This step is crucial for the electrodes be reusable. Improves the adherence of TiW layer allowing to scrape of the PDMS structure after use with major damage to the electrodes.
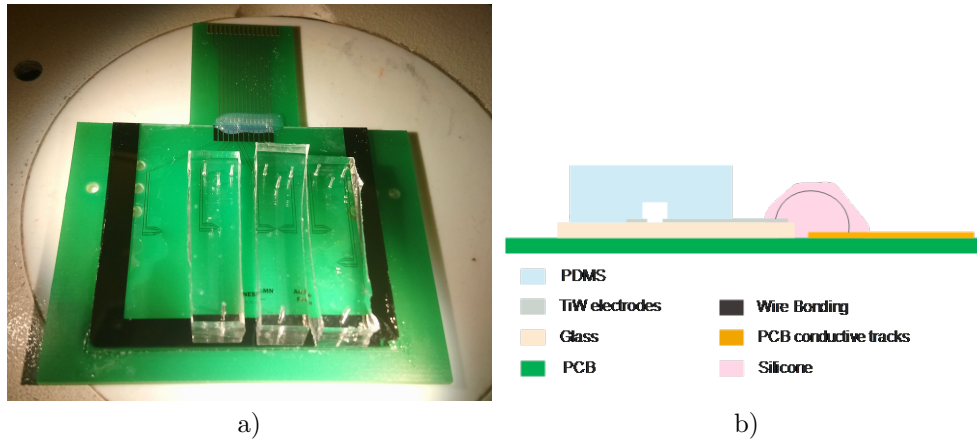
Figure 2.3: a)TiW electrodes fixed on a PCB, with wire bonding protected by a silicone layer. Integrated with microfluidic structure. b) Illustration of left image.

Alignment and sealing

Both Electrode (mounted on PCB) and microfluidic structure suffer oxygen plasma treatment for 60 s 800 mTorr level high, Harrick Plasma PDC-002-CE. Immediately after, under the microscope are aligned and pressed to each other. Typically 2-3 structures were done by batch, because the sealing won't be effective if process lasted more than 4 min.

2.1.3   3D electrodes

The tree-dimensional electrodes consists on two microfluidic channels, each one with one outlet and one inlet, filled with a conductive fluid metal, Gallium-Indium eutectic, $EGa_{75.5}In_{24.5}$ by weight ($\rho \sim 29.4 \cdot 10^{-6}\ W \cdot cm$, mp = 15.7 $°C$[65]) purchased from Merck. The injection is made with microfluidic tube, syringe and connectors. Electrical continuity was assured with a multimeter.

2.2   Experimental Setups

2.2.1   Droplet generation

To perform experiments with droplets, two immiscible phases were used. They had to be injected to the designed microfluidic structures and optically monitored to extract information about their behaviour.

Reagents

To perform droplet generation experiments two immiscible solutions were used. For the continuous phase was used a commercial fluorocarbon solution, $C_9H_5F_{15}O$ (Figure 2.4), of HFE-7500 Engineering Fluid ($3M^{TM}Novec^{TM}$) with added 2 $wt.$ % 008-FluoroSurfactant (RAN Biotechnologies). The choice of this oil-surfactant combination was due to the experience of the previous student work on droplets -the oil allows stable droplets formation and storage without coalescence- and to take advantage of the available stocks.
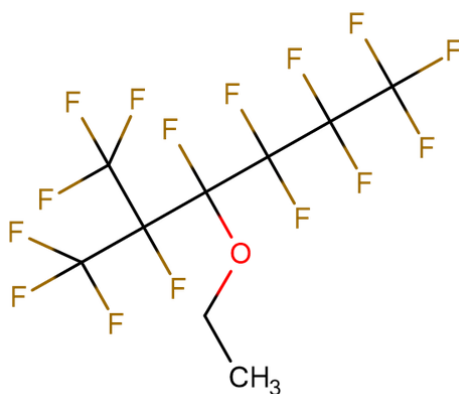
Figure 2.4: Molecular structure of HFE-7500 Engineering Fluid (3M$^{\text{TM}}$Novec$^{\text{TM}}$). $C_9H_5F_{15}O$.

For the dispersed phase generic green colorant (Globo) was used, absorbance peaks at 412 nm and 629 nm (Figure 2.5). This colorant was already used by the previous student that work with droplets, due to the good contrast to the oil, and also because the absorption peak is compatible with a portable laser (625 nm) that our laboratory already had for photosensor applications.)
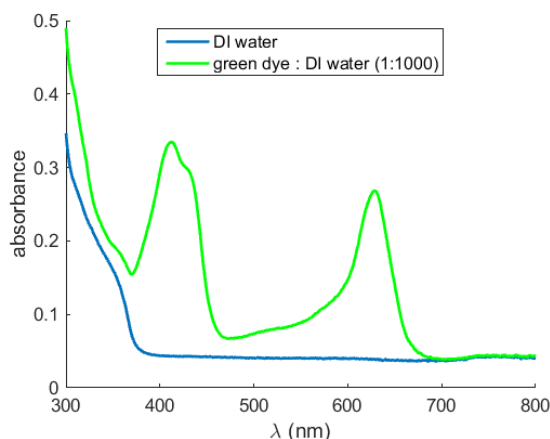
Figure 2.5: Absorbance variation with wavelength for the green dye used to form droplets, and MiliQ water used in dilution. Absorption peaks at 412 nm and 629 nm.

Injection System

In order to perform a droplet experiment inside microfluidic structures, injection system is required. Two NE-300 syringe pumps (New Era Pump Systems) in pushing mode were used. One 3D printed adapter enable to use the two oil syringes on the same pump. One pump controlled the dispersed phase and the other the continuous phase. To avoid wasting reagents inside the tube, each fluid to inject was prepareted in the following way: 1 ml syringe (CODAN) was filled with Milli-Q, air bubbles removed by agitation, then 20 ga luer stub (INSTECH) was fit and connected through BTPE-90 tube (INSTECH) to SC20/15 metal adapters (INSTECH). For the outlet, if nothing said, metal adapter and BTPE-90 tube were used. Figure 2.6 represents the system described. Showing: 1 Microscope Leica; 2 Syringe pumps; 3 Microfluidic structure; 4 Light. The system stabilizes faster if the same flow was applied for both phases (usually starts with 1 $\mu l/min$), and then the desired flow rates were setted. Experiments should start from lower to higher flow rates to avoid capacitive effects due to PDMS swelling caused by high pressure.
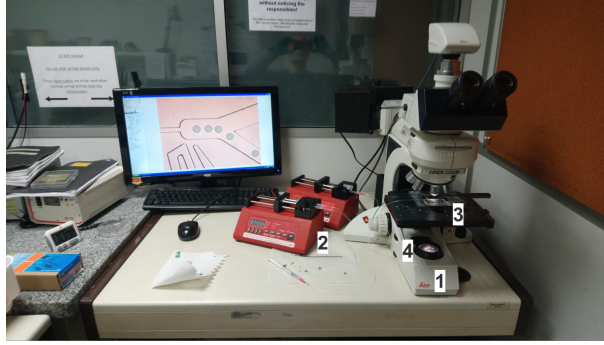
Figure 2.6: Typical Setup used in droplet generation experiments. Two syringe pumps. Leica Microscope.

Observation

Droplet generation and manipulation was observed by microscope. For the cases where planar electrodes weren't used, the PDMS structure was placed on top of a 2.5 *cm* × 5 *cm* glass slide for the non-inverted microscope LEICA DM LM. Some of the experiments were performed with Olympus microscope due to logistics (pneumatic experiments with $67.7\mu m$ height). LEICA microscope camera DFC300FX allows a recording mode of 60 fps that olympus XC30 cannot compete (only 25 fps), a so it was always used after that moment. The exposure time was set in order to see droplets without drag, but maintaining good luminosity -typically from 400 μs till 5 ms[4]. Light intensity was setted accordingly.

2.2.2 Pneumatic Actuation

Pneumatic actuation consisted in actuating one or two microfluidic channels with compressed Milli-Q. Preparation is similar to the one made for the Injection System (Section2.2.1). Here tubes are filled with mili-Q and connected to microfluidic channels and then the other side of the tube connected to the air compressed systems. Figure 2.7 shows the main components used in pneumatic setup. The valve system is composed by solenoid valves (SMC SY114-5MZ-Q) and Solenoid valve manifold (SMC SS3Y1-S41-04-M5-Q) that were actuated by On-Off rocker switches connected by a custom made PCB. From the compressed air till solenoid valves 4.4 mm I.D.[5] Polyurethane tubes (SMC TU0604) 55 cm length were used, and to connect with the syringe adapters 2.5 mm I.D. polyurethane tubes. Valves are powered by 24 V DC supply. The setup is exemplified in Figure 2.7
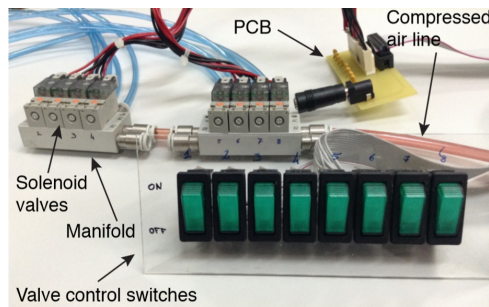
Figure 2.7: Main components used for pneumatic actuation. Developed by previous PhD student João Tiago[66].

As PDMS is permeable to air[67], one plug was inserted at the microfluidic valve outlet, and the inlet was pressurize, till all air go out. After that moment the valve is closed and the experiments may begin.

2.2.3 Electric Actuation

For experiments with planar electrodes, a external PCB was used to allow connection with High Voltage AC circuit (Figure 2.8-a)). The experiments that evolved liquid metal, a special cable with metal connec-

---

[4]Which is way lower than the 16.67 ms of capture frame rate.
[5]Inner Diammeter

tors (SC20/15) welded and silicon covered were built to connect with the supply circuit, after injection of the metal with syringe (Figure 2.8-b)).

a)   b)
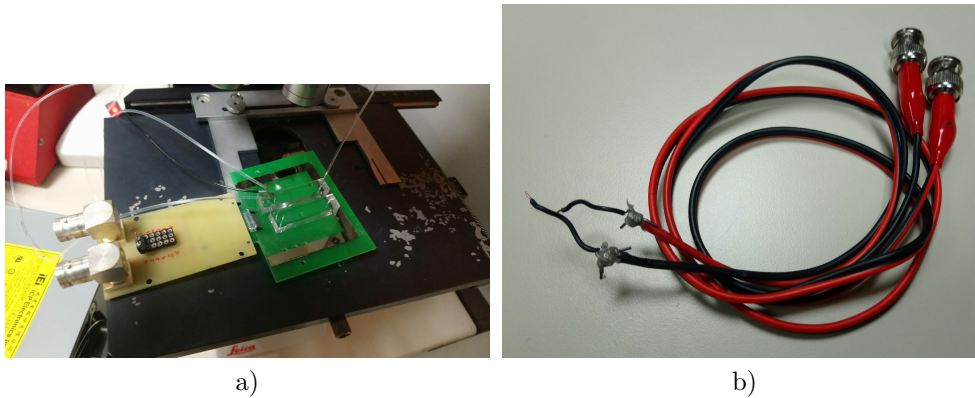
Figure 2.8: a) PCB used for connection with planar electrodes. b) Cables welded with SC20/15 connectors for liquid electrodes.

Oscilloscope (Angilent Technologies MSO7054A) was used to analyse and acquire generated wave shape. The High AC Voltage power supply developed for electric sorting is described in Section C.1.

2.2.4 Detection by Photosensors

For the experiments involving photosensors, were used 50 μm × 50 μm a-Si:H Photoconductors made by group colleague Denis Santos[68]. Sensor characterization and the final setup[6] used Al server box with 2 mm thickness, for electrical shielding. Dark current, I-V curve, I-λ curve were made with Keithley 237 picoammeter and a script developed by Denis Santos to acquire data directly to computer[68]. Fast time response measurements were performed with Pre-Amplifier (ITHACO 1211) and Oscilloscope (Angilent Technologies MSO7054A).
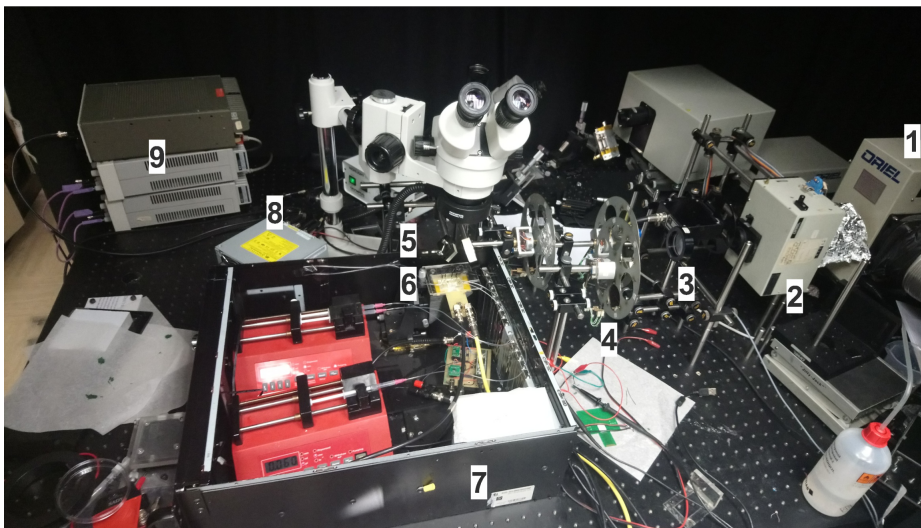
Figure 2.9: Optimized optical setup with Liquid electrodes.

Optical setup (Figure 2.9) consist on: 1 tungsten-halogen source (HLX 64655 250W Xenophot, OS-RAM, DE and lamp housing model 66184, Oriel Instruments, USA); 2 grating monochromator (Oriel Instruments 77250); 3 Collimator; 4 neutral density flters[7]; 5 Mirror and lens; 6 Photoconductor; 7 Electric shielding box; 8 High Voltage AC Circuit and respective power supplies 9. Schematic can be found in Figure 2.10.

---

[6]By final setup meant the otimized setup that covered more noise, and took advantage of a light with specific wavelength.
[7]reduce the intensity of all wavelegnts equally.
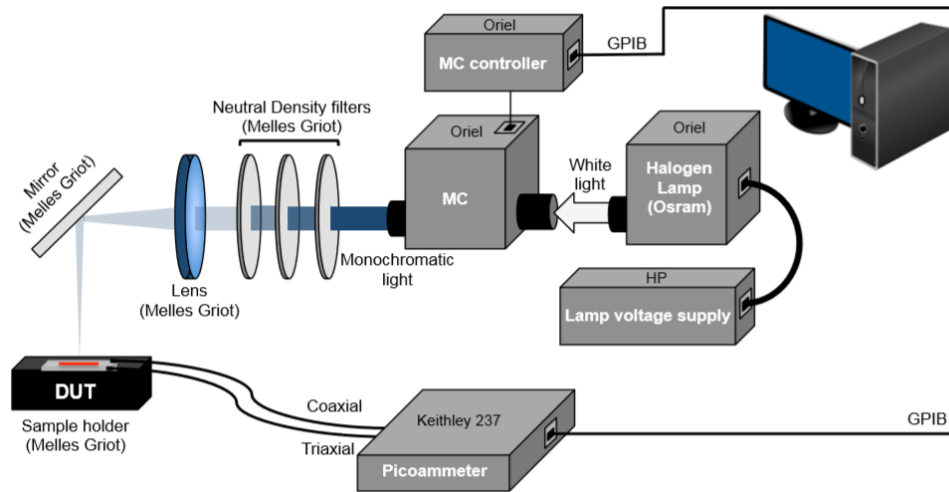
Figure 2.10: Setup schematic to characterize the photosensors[68]

2.2.5 Photosensors Characterization

Figure 2.11 shows the layout of used photoconductors. Firstly was characterized the current response with wavelength of excitation (Figure 2.12-a)). Comparison between dark current and light exposure for two different bias voltage (3 V and 30 V) is shown on Figure 2.12-b). To assure compatibility with droplet system (fast signals) response for a light signal with 500 Hz[8] is showed on Figure 2.13. The rounding of the signal is due to the rise time of preamplifier. Already some delay was observed, 240 μs.
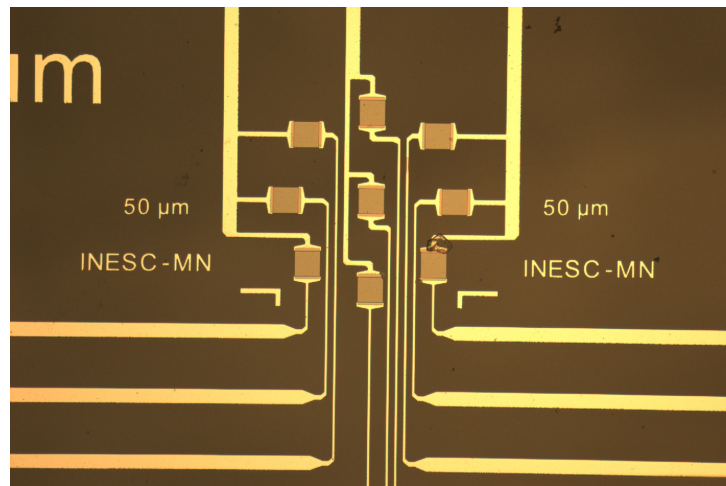
Figure 2.11: Microscope image of the Photoconductors used developed by Denis Santos[68].

---

[8]500 Hz was the maximum frequency for the wheel that cuts light.
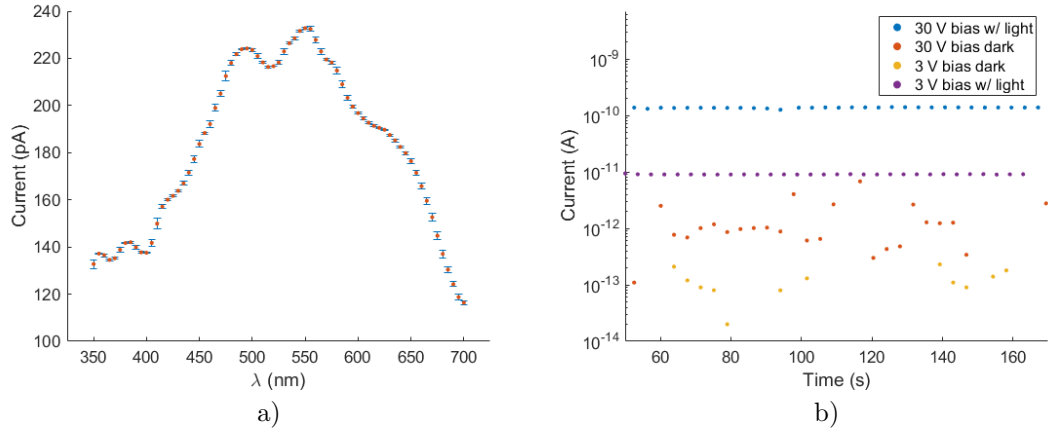
Figure 2.12: Characterization of 50 μm Photoconductors (Figure 2.11). a) Current response with excitation wavelength. b)Comparison between dark current and light current for 3 V and 30 V bias.
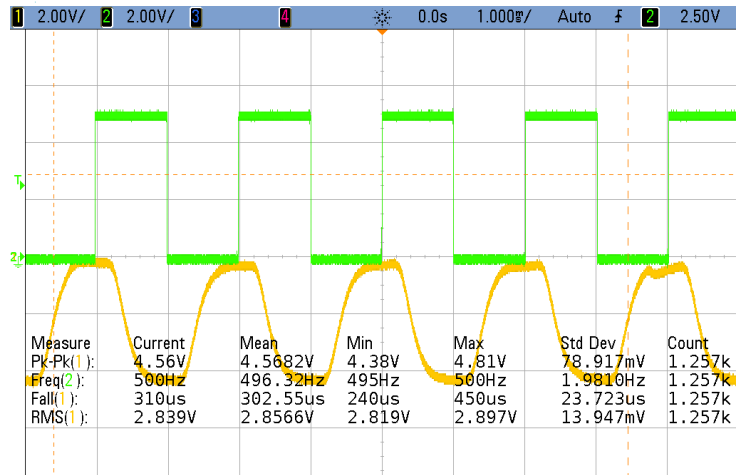
Figure 2.13: Oscilloscope image of Photoconductor response for a light Pulse of 500 Hz, with 5 V bias and 10^{10} V/I Gain 0.01 m rise time. Delay between chopper (green) and sensor response (yellow) 240 μs.

Chapter 3

Results and Discussion

A microfluidic system for directed evolution need a symbiosis of several modules, from cell mutation and encapsulation till sorting and recovery as shown in Figure 1. Guilherme Andrade[1] had already made progresses with droplet generator, comparing two different geometries, choosing flow-focusing over T-junction for its symmetry (oil phase always wets the walls) and faster droplet formation (droplets form closer to the generator).[1] Therefore in this works droplet generation was assumed as guarantee -just some experiments were made to transfer and get experience. The main focus during the work was at the integration, therefore experiments were conducted to find one or two conditions that work and not to fully characterize each module. Figure 3.1 shows the different modules used and developed on this work. (module 1) Droplet generator followed the flow focusing geometry, few modifications were made just to allow similar widths at the constriction for higher channels in z; (module 3)Sorting system by dielectrophoresis was developed. First were developed planar electrodes, for its advantage of allowing multiple alignments with microfluidic bifurcations (also developed, module 2) followed by a final design with two geometries of 3D electrodes made out of liquid metal. Pneumatic sorting was also explored. After, (module 4) detection by absorbance with photoconductors was implemented and studied. The two main modules were integrated (module 5), presenting some challenges yet to be solved.
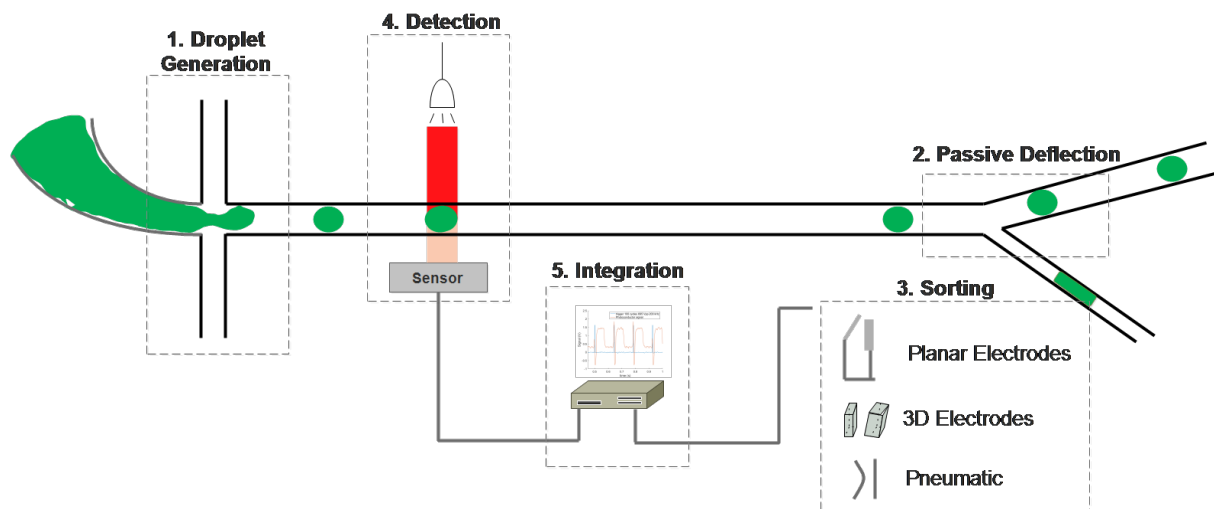
Figure 3.1: Overall view of project.

3.1 First experiments with droplet generator

By the work of the previous student Guilherme Andrade, droplet generator had already been characterized[1], but we had not much information about droplet manipulation. To get some experience on droplet generation, manipulation and process fabrication, a microfluidic mask with ten structures was designed (see Appendix A.1). Each structure had a flow-focusing generator, a deceleration zone, a reservoir, a sorting

---

[1]For the geometries designed size variation with flow rate and its dispersion was similar for both structures.

region, some had splitting geometries and others had large reservoirs with filters (Figures 3.2-a) and b)). The difference between the two designs is that for the structures with splitting geometries no big reservoir at the end was incorporated (Figure 3.2-a)). This reservoir was designed to concentrate droplets filtering the oil, but due to limitations on the fabrication it was not implemented, and no posterior design optimizations were made to integrate it.
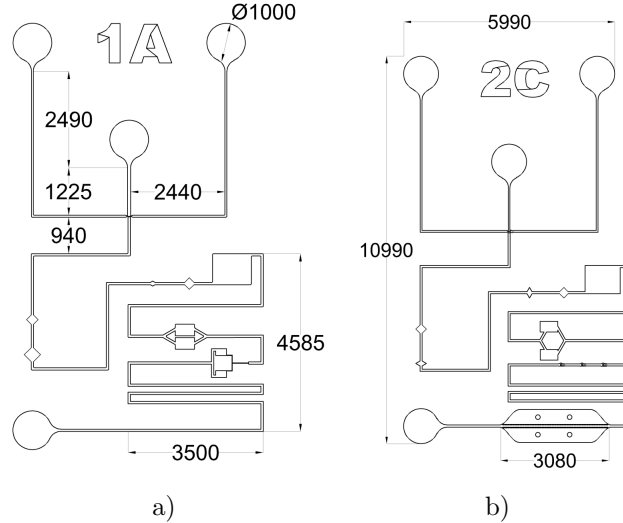
Figure 3.2: First AutoCAD mask designed. Two different types of standard structures designed: a) and b). Units in microns.

Sorting geometry is represented in Figure 3.3-a) at the top part. Besides that dimension, other with 180 μm till the bifurcation and 105 μm channels width was designed[2]. For $\phi_d = 3.4$ $\mu l/min$; $\phi_c = 9.00$ $\mu l/min$ in 40 μm height, droplets split on the narrower geometry a not in the other, as shows in Figures 3.4-a) and b). Also a splinting geometry was implemented with success designed by literature rules[69], where droplets are first accelerated by channel narrowing, and then by collision with a perpendicular wall symmetrical division occurs, as shown in Figure 3.4-c). This geometry has two small chambers to facilitate droplet visualization, by expansion and deceleration. A big reservoir with small poles 50 μm × 20 μm, was designed (Figure 3.3-b)) but wasn't enough resolution to fabricate them.

The deceleration zones (Figure 3.3-c)) consisted in losangue openings. Was intended to have a qualitative idea if works, in case that sensors could not acquire droplet signal inside 60 μm channels. If the opening was too large, droplets may collide and misalign, for smaller openings droplets decelerate without touching. Of course always depend on the tested flow rates. Also a big reservoir for droplet counting, was designed before sorting and splitting regions, to assure that droplets were observed as they were generated. Rectangular geometry wasn't well though as accumulate some droplets at the corners (flow is almost zero at those points).

---

[2]180 μm will be the length till bifurcation used on the next generation of bifurcations designed.
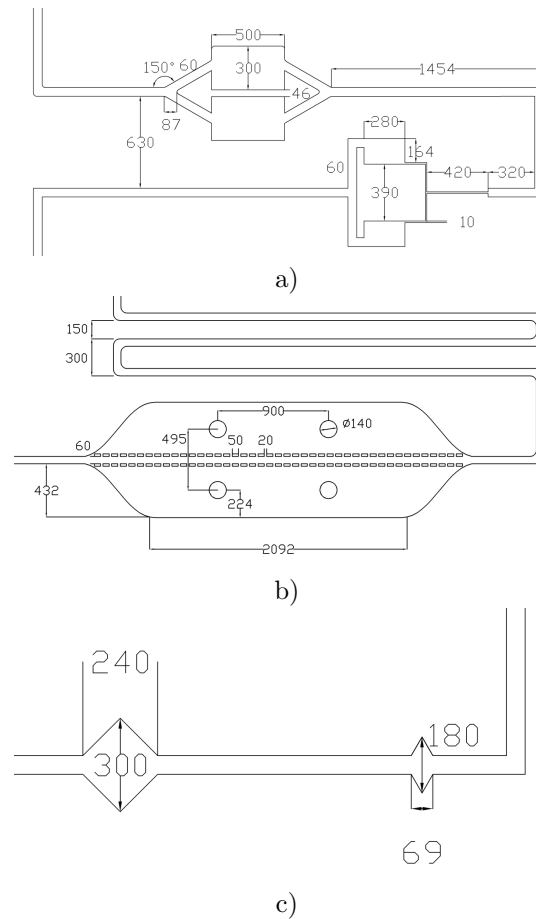
Figure 3.3: Different parts contained in the first microfluidic structure. Droplets are green, but due to different delays on processing blue and yellow channels, three colours appeared. If droplets moved slower just green appeared.
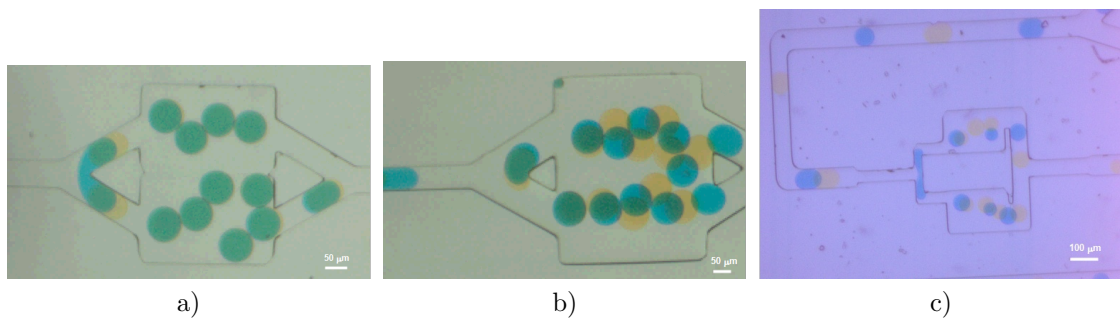
Figure 3.4: a) Sorting geometry. b) Sorting geometry with longer and wither bifurcation. c) Droplet divider.

Flow focusing geometry had to be redesigned so that same dimensions could be kept for higher channels (100 μm). Figure 3.5-a) shows the difference between the 100 μm height SU-8 mold and the AutoCAD design. Exposure time and angles were diminished to implement the design on higher channels (Figure 3.5-b)). Second generation structures had a more elongated form, already thinking on sensor and electrode integration, they have four different blocks: generator, serpentine for mixing and stabilization, bifurcation and reservoir, as shown in Figure 3.6. Global mask's view can be seen on Appendix A.2.
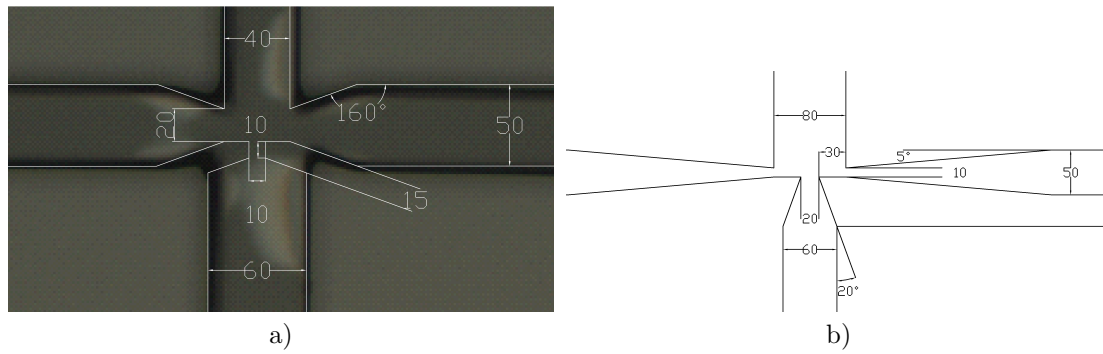
Figure 3.5: Evolutions of generator dimensions. a) first design b) was the second generation.
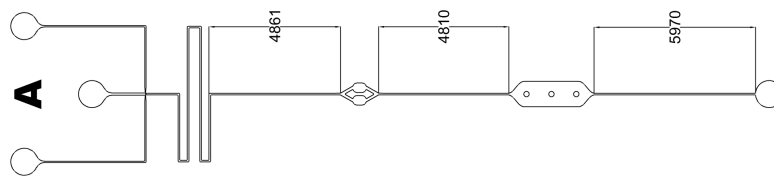
Figure 3.6: Total view of one typical structure of second design.

Figure 3.7 shows the variation of radius with the used flow rates. Axis scales are logarithmic, droplets radius are in linear scale (represented by dot size), colour gradient, representing the ratio between disperse to continuous flow rate, was used to facilitate visualization (also in linear scale). For a fixed disperse phase flow rate increasing continuous phase flow rate lowers droplet size. But for a fixed continuous phase flow rate increasing disperse phase flow rate not always increases droplet size, sometimes generation frequency increases. as happened for $\phi_c = 2 \ \mu l/min$.
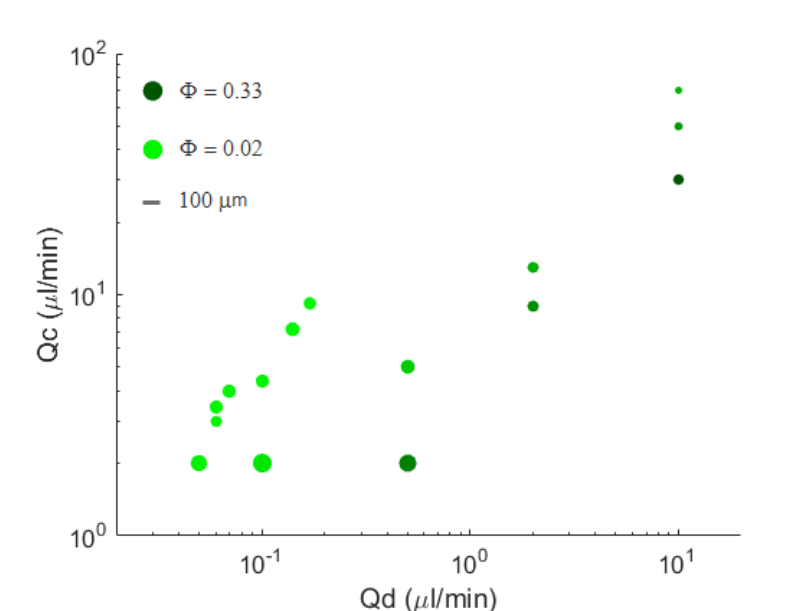
Figure 3.7: Variation of droplet size with disperse and continuous flow rates. Droplet's sizes and disperse to continuous flow rate ratio colour are in linear scale.

At this point no integration with sensors had be done yet. A proper characterization would include microscope imaging to infer droplet radius, and photoconductors (or other photosensor) to infer frequency

of generation and then correlate both. We should have in mind that droplets are very similar and it's almost impossible to track an unlabelled droplet between frames if travels fast. That was the reason why on the following experiments were chosen conditions with really low flow rates. Because generator characterization was already studied by Guilherme Andrade[1], the decision was to move forward[3]

3.2 Droplet Sorting

Two different sorting approaches were integrated with success: pneumatic and electric.

Electric is based on dielectrophoresis phenomena. Firstly was evaluated if the droplet system was able to be actuated by this phenomena (Clausius Mossoti function, Equation 1.17); after an High Voltage AC Circuit was developed to generate the required gradient field; Electrodes and microfluidic bifurcations were designed and tested, leading to a final design able to sort.

Pneumatic sorting appeared from an inspiration moment while HVAC was being built, using 3D electrodes as valves. A software to recognize and count droplets was develop to facilitate the analysis. Also delays of actuation were characterized.

3.2.1 by Dielectrophoresis

The intensity of the force depends on the particle size, medium and particle electrical conductivities and permittivities, and electrode geometry (see Equation 1.16). The first component studies was the dependence with medium and particle, translated by the Clausius-Mossoti function (Equation 1.17).

Clausius Mossoti Function Analysis

It was study the Clausius Mossoti function for different combinations of particle/medium (characteristics in Table 3.1). The study was performed running the Equation 1.17 on a script in Wolfram Mathematica Software[70]. First it was assured that the script was correct by plotting the evaluation model[71]. Then two options were taken in consideration: droplets and solid particles (beads). The bead in theory would allow less restriction in flow rates, which corresponds to less travelled distance between frames, thus more information about deflection trajectories. Looking at Figure 3.8, it's clear that silica beads could be used, but the ones that we had in our Lab. were either transparent or incompatible with the generator size[4]. Latex beads with higher conductivities seem to be good candidates because CM changes signal with frequency ($\sim 10\ kHz$).
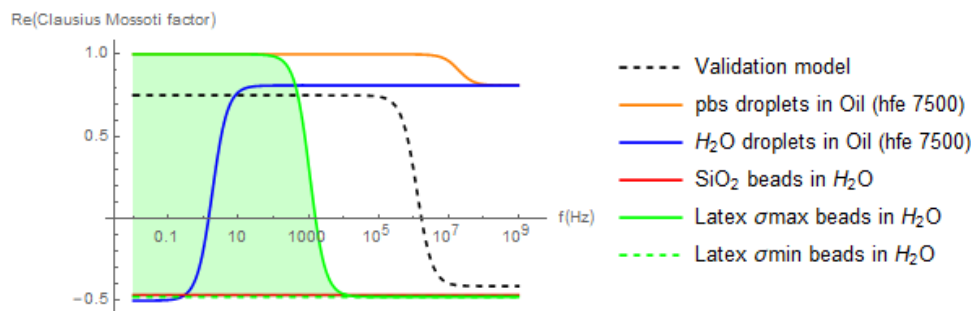
Figure 3.8: Variation of Real Part of Clausius-Mossoti function with frequency for different disperse and continuous phases combinations. Estimated by Equation 1.17 based on values in Table 3.1.
.

The green dye's electrical permittivity and conductivity were unknown. Because it was a water solution the relative permittivity should be similar to water, therefore was studied the effect for low and hight conductivities (H_2O and pbs solution). PBS also mimics a possible future scenario of droplets with encapsulated cells. It was clear that CM is positive and stable for the frequencies of work ($>$kHz). Sorting by dielectrophoresis shows to be possible for the system green dye/hfe 7500, and the force will have direction of the $\nabla |E^2|$.

---

[3]It's intended to find some conditions that make integration possible, because some changes could be done in between, it was decided to characterize systems once was established that the modules were compatible

[4]It wasn't pretended to design a new structure just for the beads.

Table 3.1: Relative electric permittivity, ϵ_r, and conductivity, σ, for the disperse - beads or droplets - and continuous phases. *Validation model - particle in aqueous electrolyte[71].

material	$\sigma(S/m)$	ϵ_r
SiO_2	10^{-17}	3.8
Latex	$10^{-17} - 10^{-5}$	2.5
pbs	0.1	80
H_2O	10^{-17}	80
hfe 7500[72]	$4.54 \cdot 10^{-9}$	5.8
particle vm*	$10 \cdot 10^{-3}$	10
medium vm*	$1 \cdot 10^{-3}$	80

Design and Fabrication of High Voltage AC Circuit (HVAC)

Voltages needed for dielectrophoresis in microfluidic are around hundred of Volts till kV range, with frequencies of few hundred kHz[73][5]. At INESC-MN there wasn't any power supply able to combine both voltage and frequency, so I built one. As we have a DC supply (hp 6209B 0-320 V; 0-0.1 A) the strategy was to design a circuit that alternate the voltage creating a square wave with 640 Vpp. Only the relative voltage between electrodes mattered, so H-bridge configuration suited well (final circuit on Figure 3.9) . The working principle is than whenever one of the transistors is On (short circuit) the other is Off (open circuit), if is open circuit no current will flow through it, the voltage at the electrode will be VDD; when the transistor is shorted, the voltage drop through the resistance R1 or R2 will determine the voltage at the electrode. R1 and R2 have the same value and will determine the rinsing time of the wave -the bipolar transistor introduces the capacitance- lower resistance, lower RC value, higher frequency of cut. The limitation is introduced by the maximum current that VDD can supply. For 0.1 A, 3.3 kΩ will enable 330 V drop with a frequency cut of 300 kHz (Figure 3.11). C_6 acts as a current compensation capacitor, for frequencies above 1 kHz the High Voltage Source couldn't supply current fast enough.
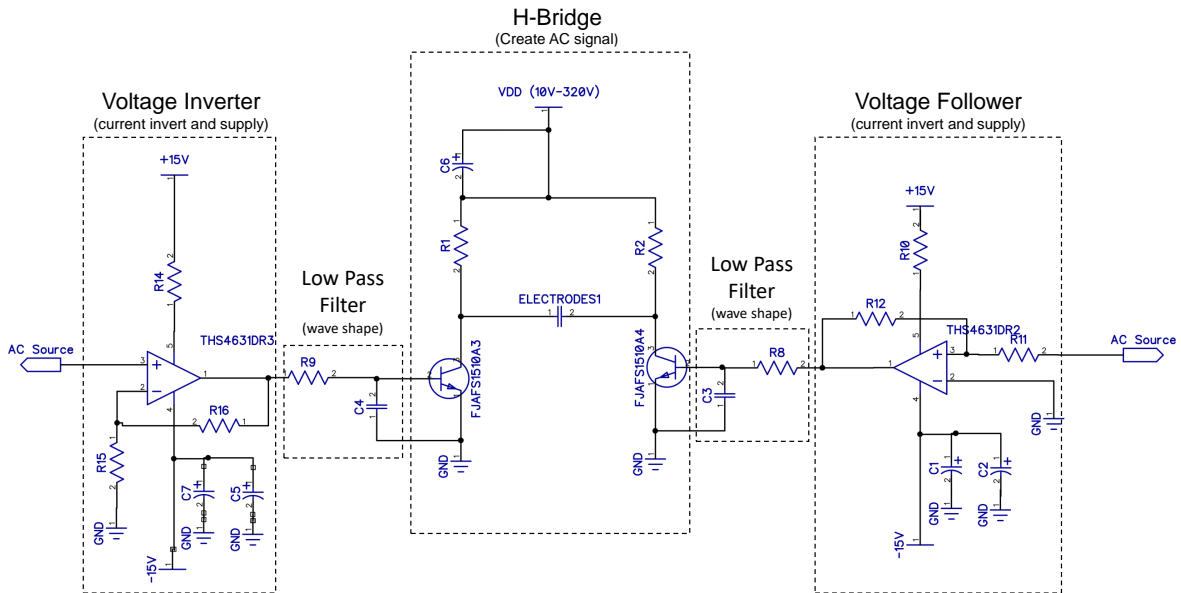
Figure 3.9: Circuit schematic to generate high voltage AC fields.

Because the current gain of these bjt is small, $h_{FE} \sim 15$, two high speed OpAmps were placed between[6] the Ac source and each transistor. Their function is to supply current for the transistors and amplifying the sinusoidal voltage signal (voltage gain given by $\pm \frac{R_{12/16}}{R_{11/15}}$), and one of them also inverts

---

[5]After 100kHz double layer effects at electrodes surface start to disapear[74]

[6]After to enable using the circuit in burst mode a 100 Ω resistor was conected from the AC Source to GND, to force 0 V when signal outuput was turned off.

the signal so that the electrodes signal oscillates between $\pm VDD$ as shown in Figure 3.10. This creates a delay effect between Ac Source and electrodes signal of $\sim 1\ \mu s$ (Figure 3.10 yellow to blue signals respectively).

The Op-Amps used are high speed, $1000\ V/\mu s$. To eliminate MHz oscillation, two $10\ \Omega$ resistors, R_{10} $R14$, are placed immediately next to the positive supply entrance of the Op-amp acting like a dissipater in a RLC circuit[7]. The capacitors connected to Op-amp's negative supply act as current compensator. The low pass filters between the Op-amp are to modulate the wave shape to make it more symmetrical. Op-Amps ideally should be symmetrical supplied till 30V total. I reality they were asymmetrically supplied with voltages ranging 7-12 V, the difference created gave fine tuning of DC voltage ($\sim \Delta 5\ V$). To create a DC offset the voltage of AC Source signal should be small so that the bjt not pull current to drop all the voltage across R_1 and R_2. This had to be adjusted for each frequency. For 0 DC at 200 kHz, 3 V_{pp} was setted. This is a disadvantage of this circuit, some non-linearities appear. Adjusting the amplitude of the ac signal and the positive and negative Op-amp's supplies always enables to set the desired DC offset between 0-100 V for each frequency, the output signal voltage is controlled by VDD. Figure 3.11 shows the response in frequency for the maximum output voltage, with DC component lower than 10 V in module.
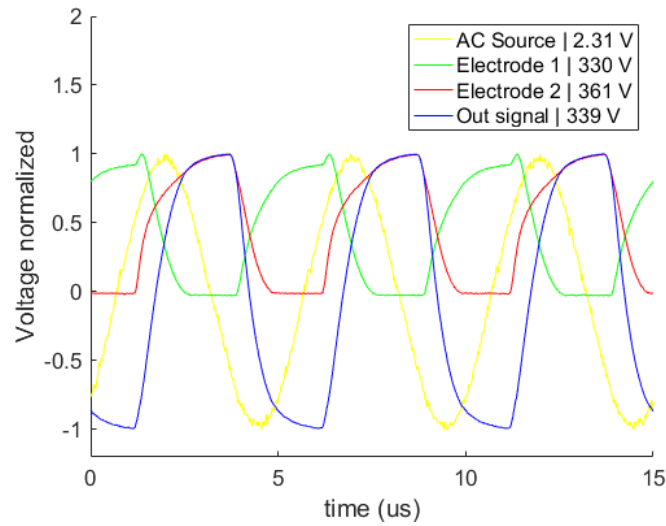
Figure 3.10: 200 kHz signal generated by the HVAC, regulated by AC Source, for each electrode and correspondent signal seen by the electrodes. Each channel is normalized to its maximum voltage.

---

[7]Inductor is created by the cables.
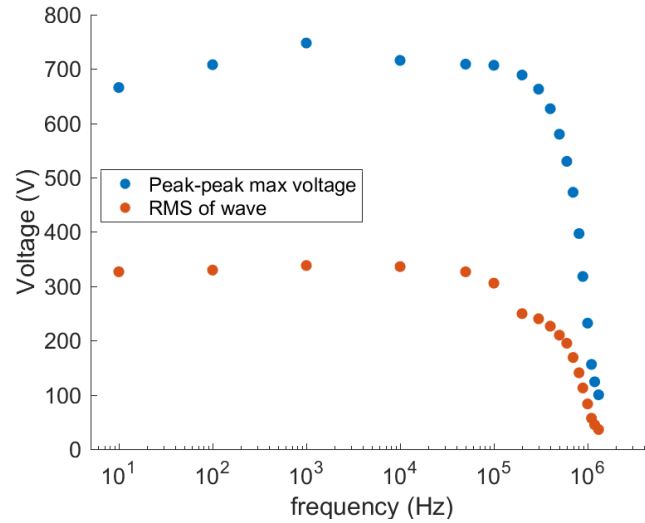
Figure 3.11: Frequency response of the circuit in Figure 3.9. Maximum peak-to-peak voltage for a DC component lower than $| \pm 10|V$; and respective *root mean square*, *rms*, values.

Figure 3.12 shows the variation of output signal's shape for different frequencies. Till 50 kHz no RC constant is irrelevant, wave is square, for higher frequencies signal starts getting sinusoidal shape (Figure 3.12-c)) and loosing amplitude (Figure 3.12-d))
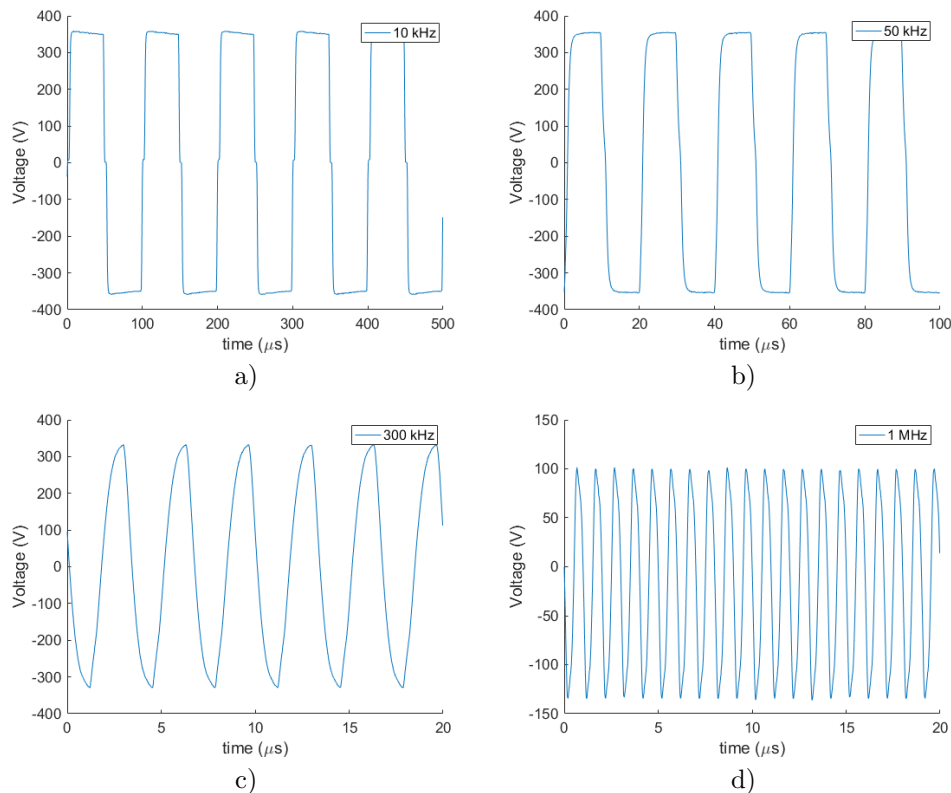
Figure 3.12: Maximum peak-to-peak output signal for different frequencies.

The circuit was implemented on a breadboard, allowing to change the components easily while fine tuning was being done. PCB or perforated boards would preferable, but to save time the circuit was kept on breadboard. Figure 3.13 shows the implementation of circuit on a breadboard in an adapted computer power supply cage. Resistors R_1 and R_2 dissipate around 30 W each so they had to be connected to a dissipater with vent. The bjt also heat up needing dissipaters. All of the dissipaters had thermal paste

32

in the junctions. External connections are with coaxial cables.

a)   b)
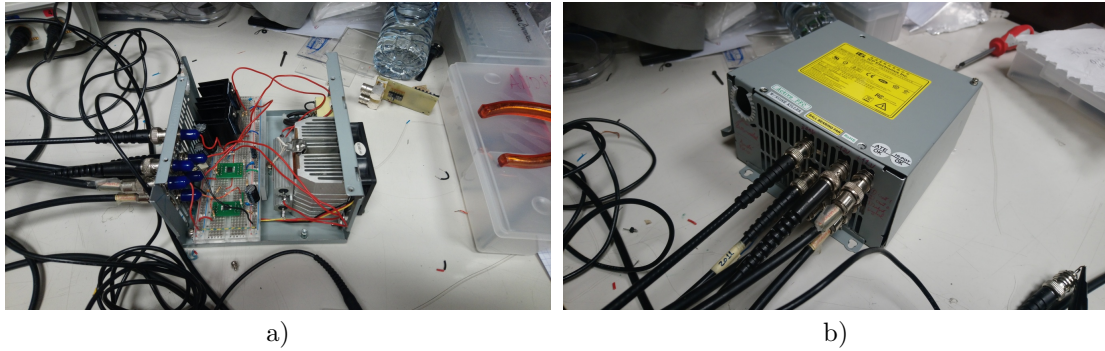
Figure 3.13: Circuit implementation. a) Open view - components arrangement; b) Circuit with box closed - working mode.

The first design used PNP transistors in opposite phase of NPN, instead of R_1 and R_2 resistors, not demanding so much current, but wave symmetry was being difficult to achieve and the decision was to simplify the circuit and move on.

Information about components and equipment used are in Appendix C.1.

Design and Simulation of TiW Planar Electrodes

Planar electrodes were chosen first due to enabling different alignments to the microfluidic channels. The design process started with COMSOL simulations, plotting $\nabla|E^2|$ in a vectorial form -green normalized arrows in Figures 3.14-3.16 and simultaneously the x and y partial derivatives -$|\frac{\partial}{\partial x}|E^2||$ and $|\frac{\partial}{\partial y}|E^2||$- in color a) and b) respectively for Figures 3.14-3.16. Gradient magnitudes should not be consider as absolute values[8], they were used for comparison between geometries, COMSOL parameters are described in Appendix C.2.

Three different geometries were studied. One with a simple geometry, a triangle facing a plate (Figure 3.14). Other two were taken from the literature, to confirm the effect and give idea of the field magnitude needed. One has one of the electrodes at the bifurcation[73] (Figure 3.15); and in the other both electrodes are located on the same side of the channel[75] (Figure 3.16). In a general way, all the three electrodes achieved the same field magnitude ($\sim 10^{14}$ $kg^2ms^{-6}A^{-2}$), what changes is the spacial distribution, having predominant gradient facing up at the bifurcation. For the first geometry (Figure 3.14) although the rectangle tips have strong field in y, the direction changes a lot in a small region, and it's not clear if the resultant force will be pointing down strongly. The intention with this design was to create the gradient at the triangle tip, which happen (Figure 3.14-a)). Looking at the gradient in x (Figure 3.14-b)) a gradient valley was created, this could mean that droplets will slow down or even stop. By the plots was thought that this geometry may work if placed near to the bifurcation

---

[8]PDMS walls were not taking in account, leading to over estimation of gradient's magnitude (see Appendix C.2).
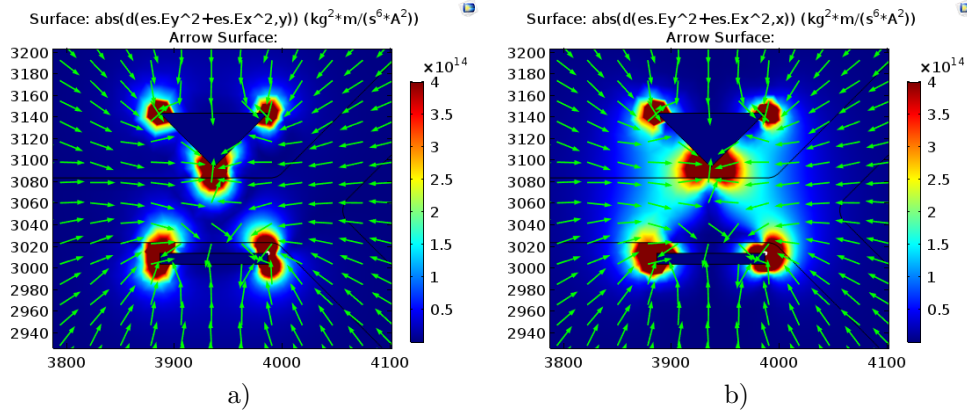
Figure 3.14: COMSOL simulation. Designed electrodes with simple geometry. Spacial derivative in a) y and b) x of the squared electric field. Arrows represent the gradient of the squared electric field of Dimensions in microns.

For the second geometry (Figure 3.15) in the vertical direction, gradient is facing up before the central electrode[9] (situated at the middle of bifurcation), and then for the upper channel the gradient is opposite to the fluid flow. This effect may not cause much problems in burst mode, because the actuation is just to deflect the droplets before bifurcation, but in continuum may slow down droplets and coalesce them. Was thought than if the top electrode was near the bifurcation, gradient would be more useful and the field at the central electrode will be far from the bifurcation.
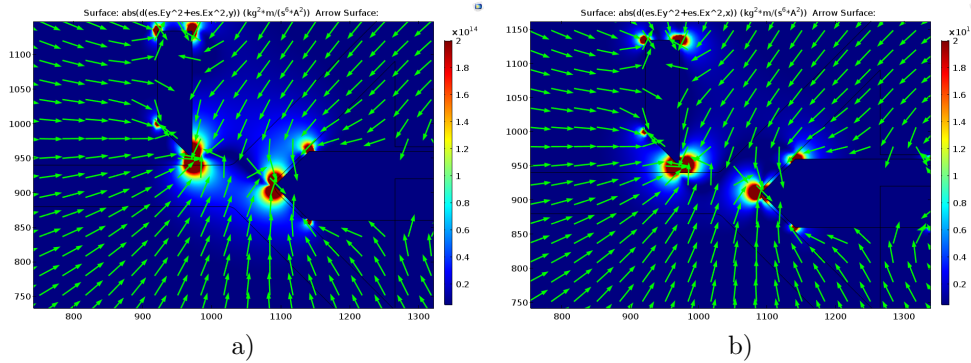
Figure 3.15: COMSOL simulation for planar electrodes used in droplet sorting[45]. Spacial derivative in a) y and b) x of the squared electric field. Arrows represent the gradient of the squared electric field of Dimensions in microns.

The third geometry considered (Figure 3.16) presented the higher vertical gradient for longer horizontal distance. And because is situated in just one side of the channel gives more freedom to design the microfluidic channel if 3D electrodes are desired. The horizontal gradient is one order lower in magnitude than the other geometries.

---

[9]The reference to central electrode is due to the fact that in the original configuration other electrode mirrored to the top one was at the bottom, and both were actuated with respect to the central one.
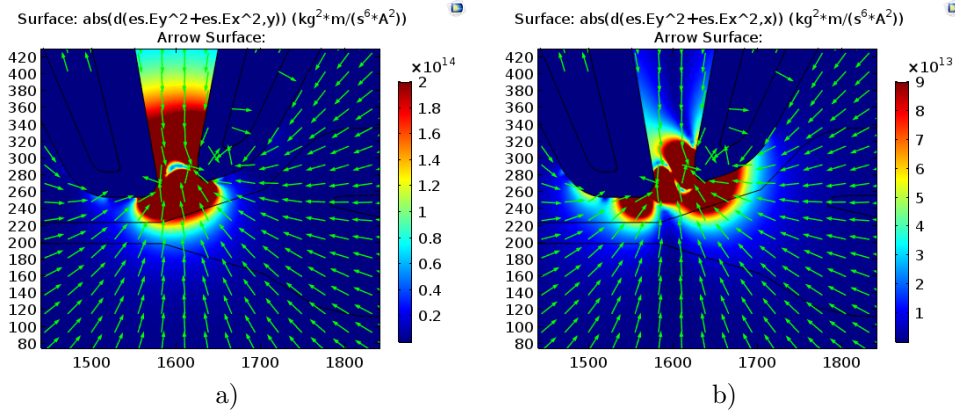
Figure 3.16: COMSOL simulation for 3D electrodes used in droplet sorting[75]. Spacial derivative in a) y and b) x of the squared electric field. Arrows represent the gradient of the squared electric field of Dimensions in microns.

Planar electrodes have around 200 nm in height, much lower than droplet radius and channel height ($\sim 50 - 100 \ \mu m$), meaning that a lot of field will be lost, fringe field actuates the droplet.

Overall view of electrodes mask and dimensions can be seen in Appendix C.5

Design of Microfluidic Sorting Structures

To enable sorting, microfluidic bifurcation is needed. Were tested 5 different bifurcations. To avoid differences in pressure caused by the outlet tubes[10], all the bifurcations join after at the same outlet. All the structures have a small reservoir to allow droplet deceleration, which facilitates image analysis and statistical count. The round corners are critical to avoid droplet accumulation.

It was intended to study two different phenomena, sorting by hydraulic resistance (droplet as fluid) and by momentum (droplet as particle). Here sorting is refereed as a passive phenomena, for given flow rate without external actuation droplets will choose one branch, or a characteristic distribution. Figure 3.17-a) corresponds to the symmetrical structure (like a control), same volume for each branch and with the same angle (150°). Other geometrical symmetrically bifurcation is represented on Figure 3.17-b), this differ from the first by having one branch with twice the hydraulic resistance.
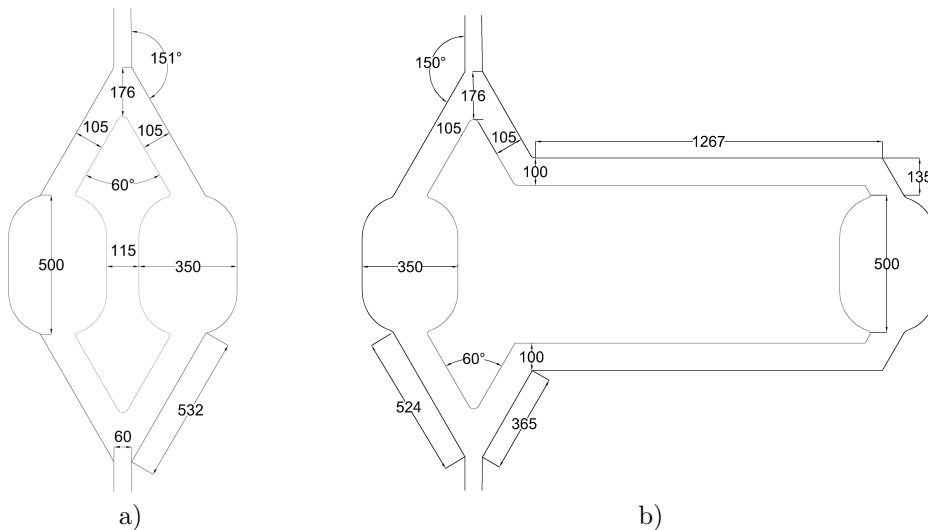
Figure 3.17: Autocad mask for the sortings structures. a) Symmetric bifurcation and equivalent hydraulic resistance. b)Symmetric bifurcation and 1:2 hydraulic resistance ratio. Dimensions in microns.

Figure 3.18-a) have both branches with same hydraulic resistance, but differs from Figure 3.17-a) for having one of the branches aligned with the input channel. The other structure combines both effects

---

[10]The tubes have around 500 μm in diameter, differences in length introduce an extra hydraulic resistance.

(Figure 3.18-b)), and was designed with more hydraulic resistance difference (1:2.5 instead of 1:2) fo the avoid the possibility of the difference not causing deflection.
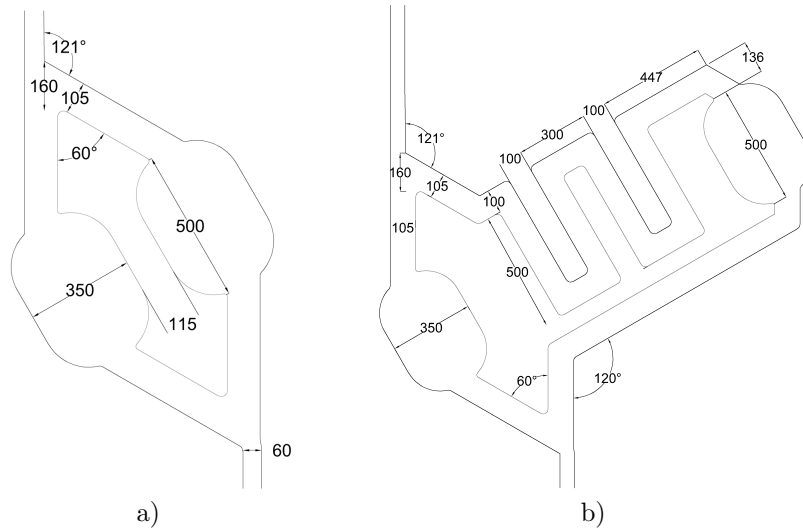
Figure 3.18: Autocad mask for the sortings structures. a) Asymmetric bifurcation and equivalent hydraulic resistance. b)Asymmetric bifurcation and 2:5 hydraulic resistance ratio. Dimensions in microns.

The last structure tested (Figure 3.19), adapted from the literature[75], have asymmetrical bifurcation and different hydraulic resistance ratio (5:8). This case also differs from the last for by having different brunch width immediately at the bifurcation .
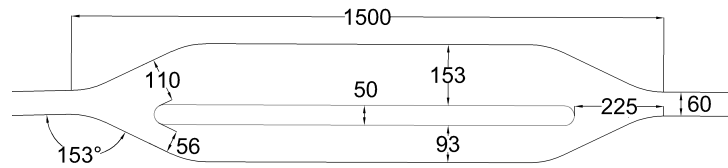
Figure 3.19: Autocad mask for the sortings structures. a) Asymmetric bifurcation and 5:8 hydraulic resistance ratio - adapted[75]. Dimensions in microns.

Full view of microfluidic structure can be seen in Appendix A.2.

Experiments with TiW Planar Electrodes

Combining the information of Clausius Mossoti function from Figure 3.8 with the HVAC response in frequency (Figure 3.11), it was chose the higher frequency that maintains the voltage at its maximum, 300 kHz. Higher frequencies avoid double layer capacitance, as ions don't have enough time to move, not charging the capacitor.[11].

At beginning mechanical sealing was performed - allowing electrodes reuse- (see Appendix C.3, due to some sliding between PDMS and glass surface, electrodes were scratch, when happened at the electrodes track, $40\mu m$ width, couldn't be used any more. For that reason, permanent sealing with oxygen plasma treatment was chosen. After was discovery that the scratch easiness came from poor deposition adherence -which was improver by oxygen plasma treatment before TiW deposition. Due to permanent sealing[12] and by the fact that neither all electrode and microfluidic bifurcations are compatible, not all combinations were tested.

Two different droplet regimes were used: low flow rate $\phi_d = 0.06 \ \mu l/min$; $\phi_c = 3.00 \ \mu l/min$, and high flow rate $\phi_d = 2.06 \ \mu l/min$; $\phi_c = 9.00 \ \mu l/min$. Droplet have similar radius for both flows ($29.7 \pm 0.2 \ \mu m$

---

[11]Looking now to the circuit characterization (Figure 3.11), frequency of 90-100 kHz would make more sense because rms value is the one that is taken in account, and not Vpp.

[12]And some fabrication processes went wrong.

and $29.9 \pm 0.2 \ \mu m$ for low and high flow rate respectively), but at the lower one besides moving slower, are more spaced. All experiments with planar electrodes were performed for $40 \ \mu m$ channel height.

The first combination being tested was the tip electrodes with symmetrical microfluidic, Figure 3.20, for a low flow rate. Without applied field droplets distribute evenly in pairs by the two brunches[13](Figure 3.20-a)). Presence of gradient was clearly observed, for both bottom and top electrode actuation (Figure 3.20-b) and c), but seemed to be too strong, forcing droplets to stop at the tip, and just being released when other came and coalesced. The bottom electrode when aligned had its tip a bit more inside the channel than the top one, this region when in contact with droplet produces air droplets by electrolysis seen in Figure 3.20-b). Lowering the voltage didn't avoid coalescence, it always appended till a threshold that droplets flow as the electrode was tuned off. This was due to the strong gradient field that was seen on simulations at the electrode tip (Figure 3.15).

| a) OFF | b) bottom ON | c) Top ON |
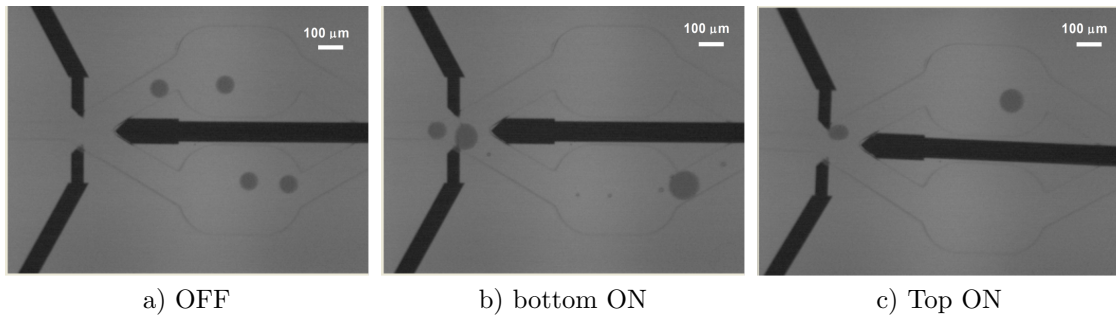
Figure 3.20: Sorting experiment with low droplet frequency generation. Actuation of b) bottom and c) top electrodes (with respect to the central one). $\phi_d = 0.06 \ \mu l/min$; $\phi_c = 3.00 \ \mu l/min$, $670.10 \ V_{pp} \ (AC) \ 3.00 \ V (DC) \ f = 300 \ kHz$.

For the high flow rate, droplets didn't stop any longer for low voltages (Figure 3.21-b), but the deceleration in a zone where strong field causes coalescence (Figure 3.21-b and c)). Was observed that lowering the voltage always creates coalescence, just changing the relative amount of dye solution that goes for the actuated side, the more the voltage higher ratio observed.

| a) OFF | b) $410.10 \ V_{pp} \ (AC) \ 1.20 \ V (DC)$ | c) $670.00 \ V_{pp} \ (AC) \ 3.00 \ V (DC)$ |
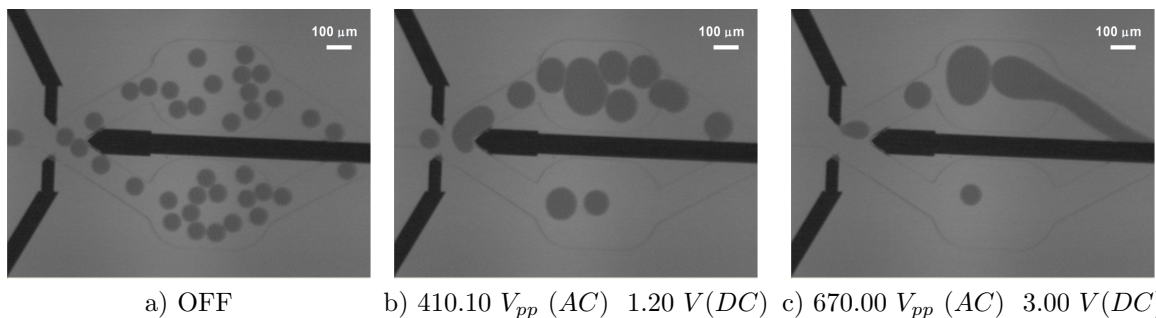
Figure 3.21: Sorting experiment with high droplet frequency generation. Top and central electrodes actuated. $\phi_d = 2.06 \ \mu l/min$; $\phi_c = 9.00 \ \mu l/min$, $f = 300 \ kHz$.

Figure 3.22 shows the experiment with tip electrodes with geometrically symmetrical bifurcation and 1:2 hydraulic resistance ratio. Due to wire bonding problem just one of the electrodes could be used forcing to invert them. Actuating the bottom electrode cause droplets to stop at the top electrode[14]. Droplets tend to adhere to electrodes surface even for low voltages as 5V. Also was confirmed that 1:2 hydraulic resistance ratio forces droplets to go to the less resistance branch even for low and high flow rates (Figures 3.22-a) and d)). If droplets are very close to each other, they tended to accumulate and periodically one droplet went by the other branch (Figure 3.22-c)).

---

[13]Because droplets move slower than the fluid[76, 77] , phenomena also observed by the previous student in this systems[1] when they get into the reservoir and slow down increasing the pressure at that branch, in this case two droplets were needed.

[14]Top electrode is floating

a) OFF

b) 300.00 V_{pp} (AC) 1.55 $V(DC)$

c) $\phi_c = 9\ \mu l/min$

d) $\phi_c = 13\ \mu l/min$
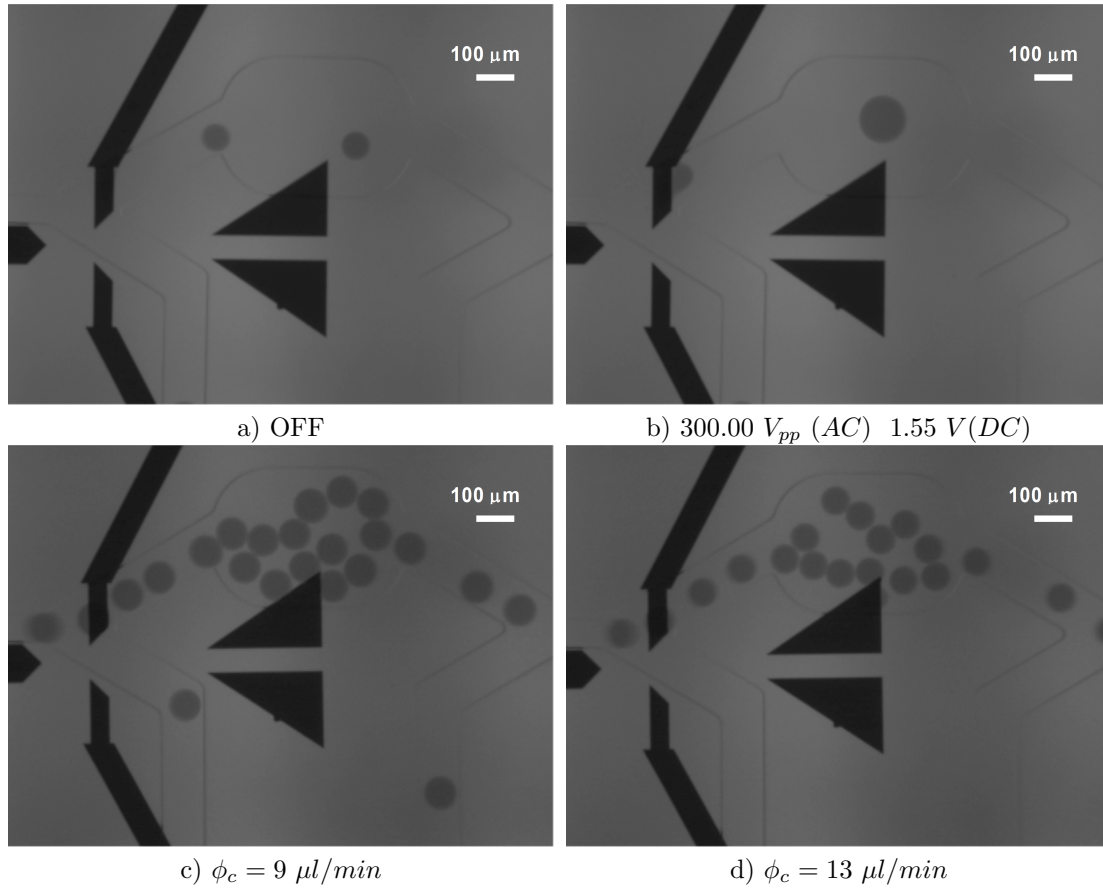
Figure 3.22: Study of sorting with hydraulic resistance, electrodes were used inverted due to wire bonding error. b) bottom electrode activation but visible effect on the top one, being inside the channel requires less potential to have the same force. a), b) $\phi_d = 0.06\ \mu l/min$; $\phi_c = 3.00\ \mu l/min$; c), d) $\phi_d = 2.06\ \mu l/min$.

Triangular electrode was tested with the asymmetrical diamond structure. For the low flow rate when electrodes are turned off, droplets always go to the upper branch (Figure 3.23)-a). Figures 3.23-b) and c) are sequential photos showing droplet trapping and coalescence, two droplets are enough two release from the electrode tip. For this combination voltage threshold[15] was 80-110 V_{pp}, the variation is due to droplet speed oscillations.[16] Around 180 V_{pp} air bubbles start to appear and electrodes start to dissolve (see Appendix C.4).

a) OFF

b)

c)
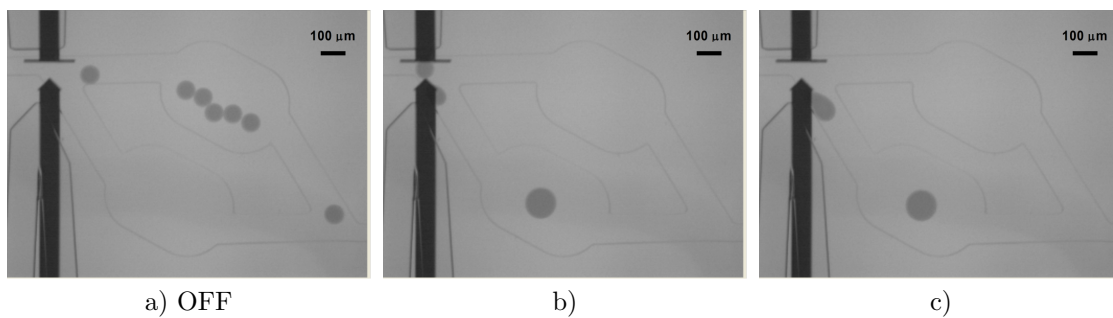
Figure 3.23: Sorting experiment with low droplet frequency generation. Planar electrodes actuated at b) $t = 0\ s$ and c) $t = 16.7\ ms$, showing droplet coalescence. $\phi_d = 0.06\ \mu l/min$; $\phi_c = 3.00\ \mu l/min$, 127.00 V_{pp} (AC) 0.70 $V(DC)$ $f = 300\ kHz$.

The same electrode geometry was tested for the splayed bifurcation. For low flow rate, without applied

---

[15]Threshold voltage stands for the minimum voltage applied to see droplets deflecting or stopping,

[16]For this experiment when removing the connectors to fill up the tubes with oil, the sealing was undone, impeding testing other flow rates.

voltage droplets go by the upper branch (Figure 3.24-a)). With 127 V_{pp} -voltage just few volts above threshold- a sequence of one droplet stop, getting hitted by other, coalescence and releasing is showed on Figures 3.24-b)-e).

a) OFF b) ON $t = 0$ s

c) ON $t = 233$ ms d) ON $t = 267$ ms e) ON $t = 300$ ms
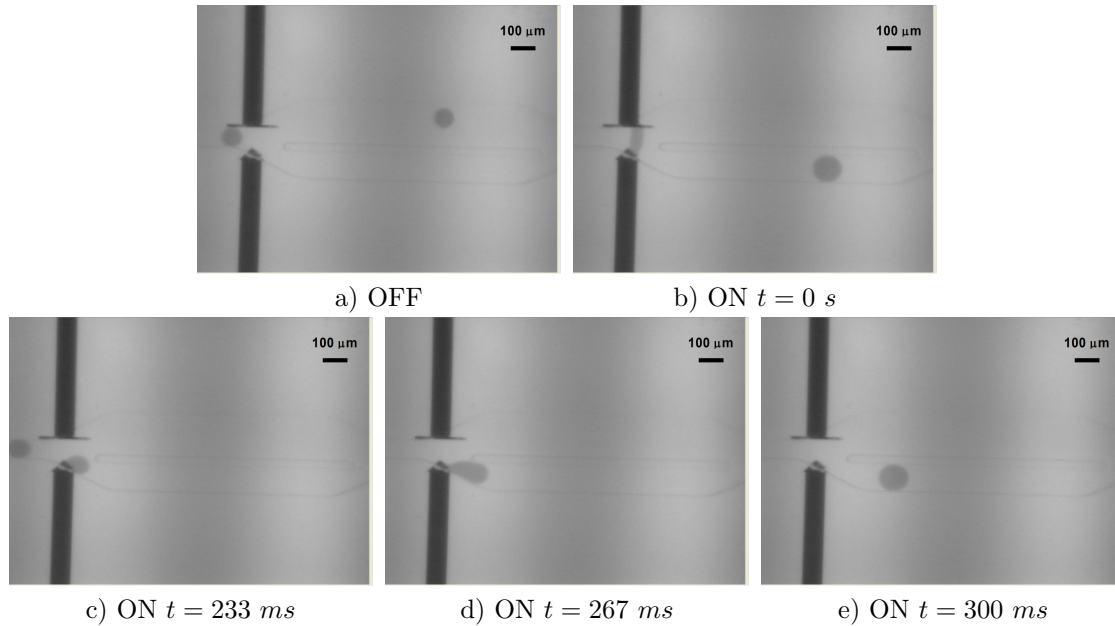
Figure 3.24: Sorting experiment with low droplet frequency generation. Planar electrodes actuated, showing droplet coalescence (c), d) and e) are consecutive frames) . $\phi_d = 0.06 \ \mu l/min$; $\phi_c = 3.00 \ \mu l/min$, $127.00 \ V_{pp} \ (AC) \ \ 0.70 \ V (DC) \ f = 300 \ kHz$.

Increasing the flow rate didn't avoid coalescence. Droplets went by both branches even for much higher voltages as shown in Figures 3.25-b) and c). Also with electrodes turned off droplets went by both branches.

a) OFF b) ON 137.00 V_{pp} (AC) c) ON 340.00 V_{pp} (AC)
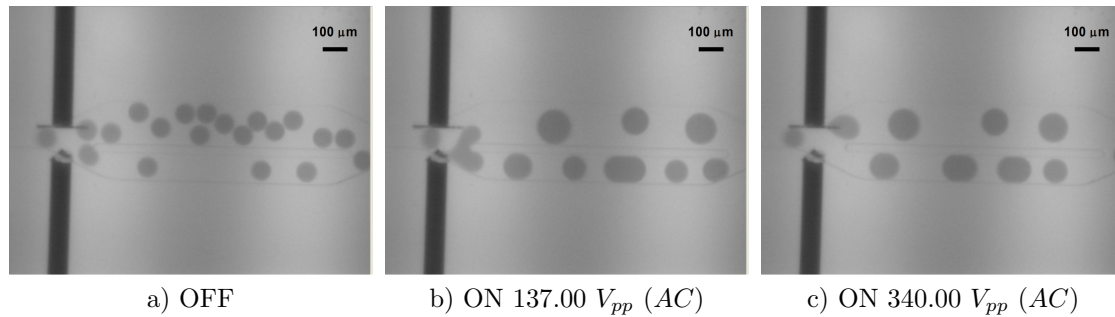
Figure 3.25: Sorting experiment with high droplet frequency generation. Planar electrodes actuated with different voltages. $\phi_d = 2.06 \ \mu l/min$; $\phi_c = 9.00 \ \mu l/min$, $f = 300 \ kHz$ a) 0.50V (DC), b) 0.75V (DC).

The combination of single-side electrodes and splayed bifurcation (Figure 3.26) was studied for high and low flow rates. Maximum voltage deflects the droplet but not enough so sort it (Figures 3.26-a) and b)). For the high flow rate, droplets coalesced but didn't sort. This experiment showed than bigger distance from the channel opening to the bifurcation may be needed in order to give time for the droplet to deflect. On this set, droplets are bigger than in the previous sets, meaning the flow hadn't been stabilized yet.

a) OFF

b) $656.00\ V_{pp}\ (AC)\ \ 0.20\ V(DC)$

c) OFF

d) $656.00\ V_{pp}\ (AC)\ \ 0.20\ V(DC)$
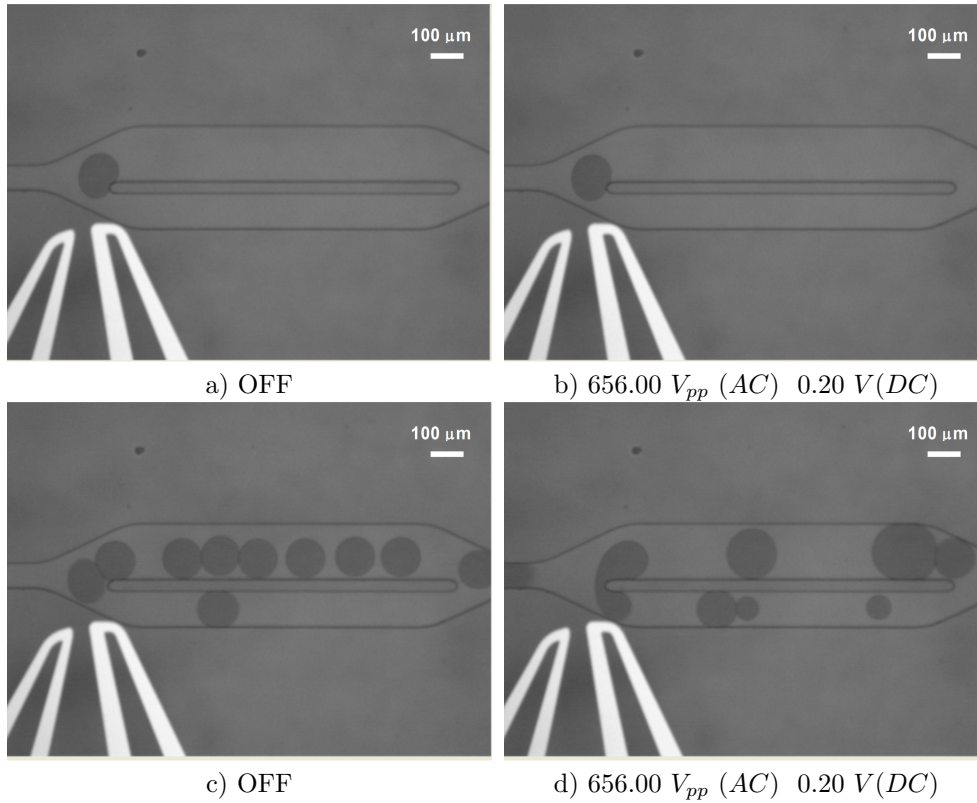
Figure 3.26: Sorting experiment for: a), b) low - $\phi_d = 0.06\ \mu l/min$; $\phi_c = 3.00\ \mu l/min$ - and c), d) high - $\phi_d = 2.06\ \mu l/min$; $\phi_c = 9.00\ \mu l/min$ - droplet frequency generation. $f = 300\ kHz$.

Single-side electrodes was tested for the diamond bifurcation (Figures 3.27 and 3.28). For high flow rate droplets coalesced always, just changing the amount of droplets not sorted. Figures 3.27 b), c) and d) show this variation, more voltage less droplets for the not actuated bifurcation.

a) OFF	b) 200.60 V_{pp} (AC) 10.78 $V(DC)$
c) 400.00 V_{pp} (AC) 5.88 $V(DC)$	d) 663.09 V_{pp} (AC) 3.72 $V(DC)$
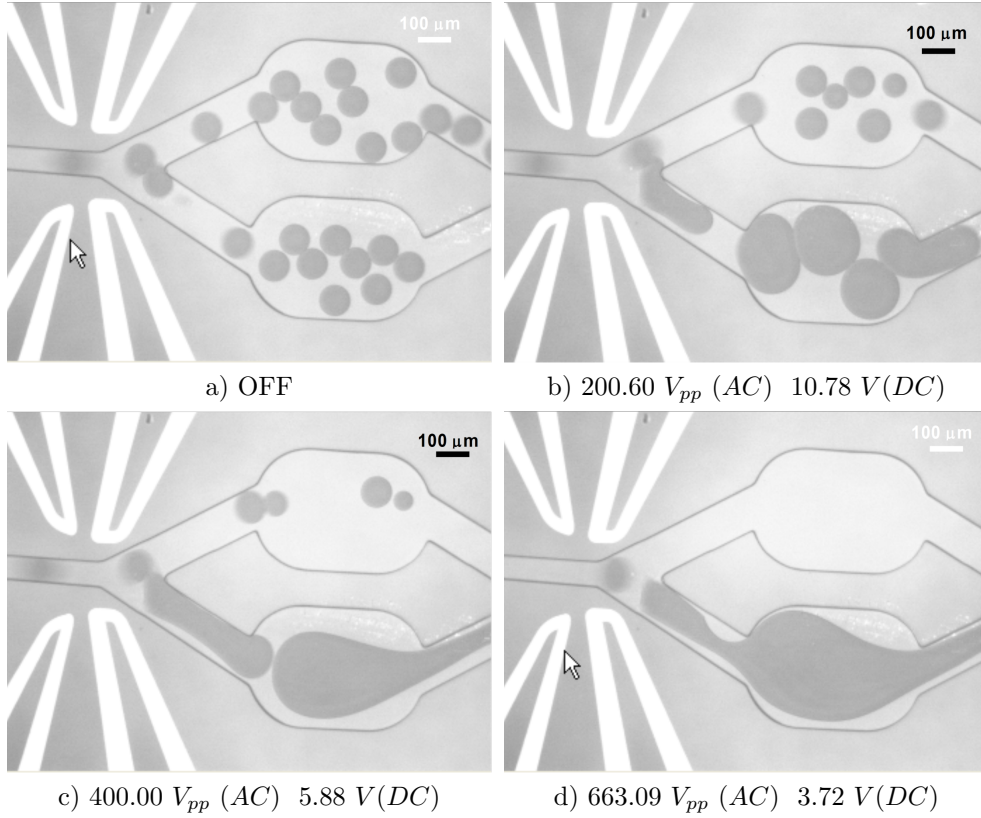
Figure 3.27: Sorting experiment for high droplet frequency generation, with different voltages at 300 kHz. $\phi_d = 2.06\ \mu l/min$; $\phi_c = 9.00\ \mu l/min$.

For the low flow rate it was found a voltage value, 336 V_{pp} at which droplets deflect and did not coalesce (Figure 3.28-b)), for 664 V_{pp} droplets deflect but the stooped ate the bifurcation creating coalescence whenever other droplet came (Figure 3.28-c). To extract information about the involved gradients, it was performed a simulation for this alignment. Figures 3.29-a) and b) show the simulation and gave information about the magnitude of gradient at the region where droplets stooped. $1.7 - 7.1 \cdot 10^{14}$ $Kg^2 \cdot m \cdot s^{-6} \cdot A^{-2}$ from 336 V_{pp} to 664 V_{pp}.

a) OFF   b) 336.00 V_{pp} (AC) 9.82 $V(DC)$ c) 664.00 V_{pp} (AC) 4.00 $V(DC)$
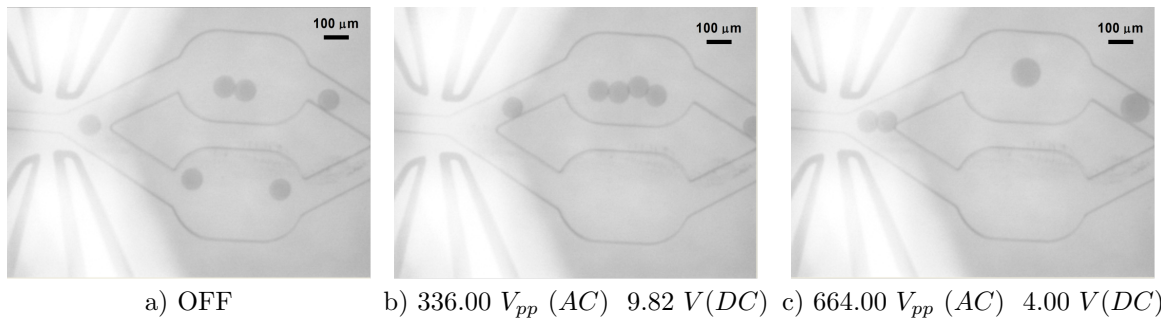
Figure 3.28: Sorting experiment for low droplet frequency generation.a) without applied field droplets sort evenly. b) lower voltages deflect droplet without coalescence. b) higher voltages stop the droplet at junction promoting coalescence before sorting. $\phi_d = 0.06\ \mu l/min$; $\phi_c = 3.00\ \mu l/min$; $f = 300\ kHz$
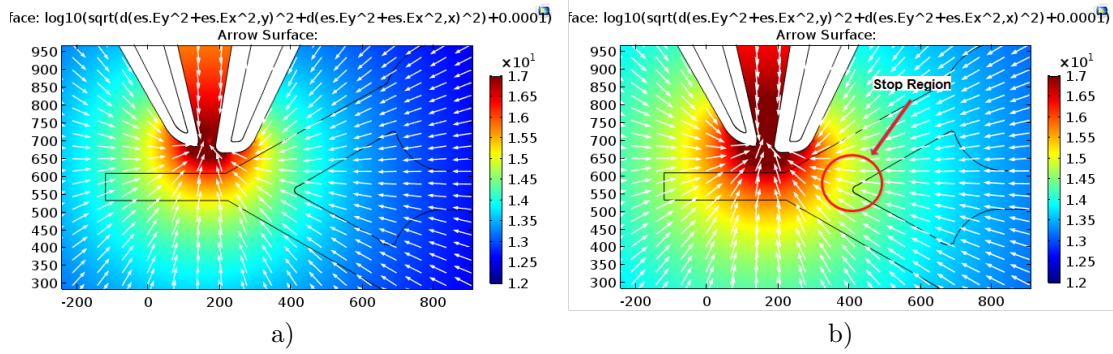
Figure 3.29: COMSOL simulation for the experimental alignment and field used in Figures 3.28-b,c. a)336.00 V_{pp} b) 664.00 V_{pp}.

The planar electrodes experiments demonstrated sorting, enabling to infer the gradient magnitude required fro droplet deflection at these flow rates. Also showed that microfluidic bifurcations should be longer, taking by principle mainly hydraulic resistance, as by momentum requires specific flow rates. In some cases where electrodes stayed in contact with solution, electrolysis was observed (even in oil) and if in contact with droplets electrodes dissolve in seconds, see Section C.4.

Design and Simulation of 3D Electrodes

3D electrodes were adapted from the triangular design (Figure 3.14) to be compatible with soft lithography methods, meaning bigger separations between electrodes. Gradient field was just simulated after the fabrication to understand better what was happening. Figure 3.14-b) shows a gradient valley in the longitudinal direction to the channel, justifying the observed trapping effect.
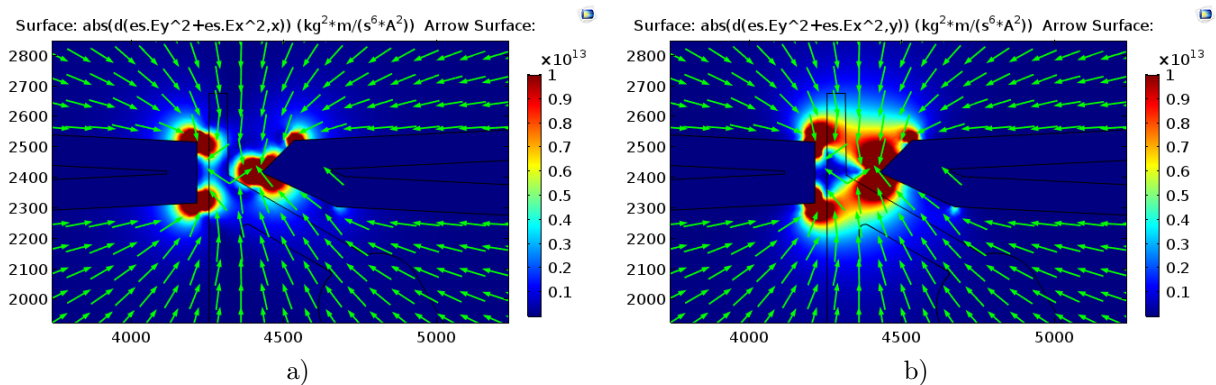
Figure 3.30: COMSOL simulation. 3D electrodes adapted from planar geometry (Figure 3.14) to be compatible with microfluidic fabrication. Spacial derivative in a) x and b) y of the squared electric field. Arrows represent the gradient of the squared electric field of Dimensions in microns.

Experiments with 3D Electrodes.

3D electrodes consist in microfluidic channel filled up with liquid metal. Continuity was always confirmed during experiments, by applying the field at inlet and acquiring it at the outlet with oscilloscope.

In 40 μm height structures, for low flow rate the shift caused is almost negligible[17] (Figures 3.31-a) and b)). The presence of gradient is more noticeable for the high flow rate where sorting effect is not much present -not so much droplet volume deflects down- but coalescence is (Figures 3.31-c) and d)).

---

[17]Notice that the image acquisition rate is at 60 fps, 16.67 ms between consecutive frames, meaning that is hard to be sure that both frames (with and without field) correspond to the same exact moment.

a) OFF   b) ON 608.00 V_{pp} (AC) 1.00 $V(DC)$

c) OFF   d) ON 609.00 V_{pp} (AC) 1.01 $V(DC)$
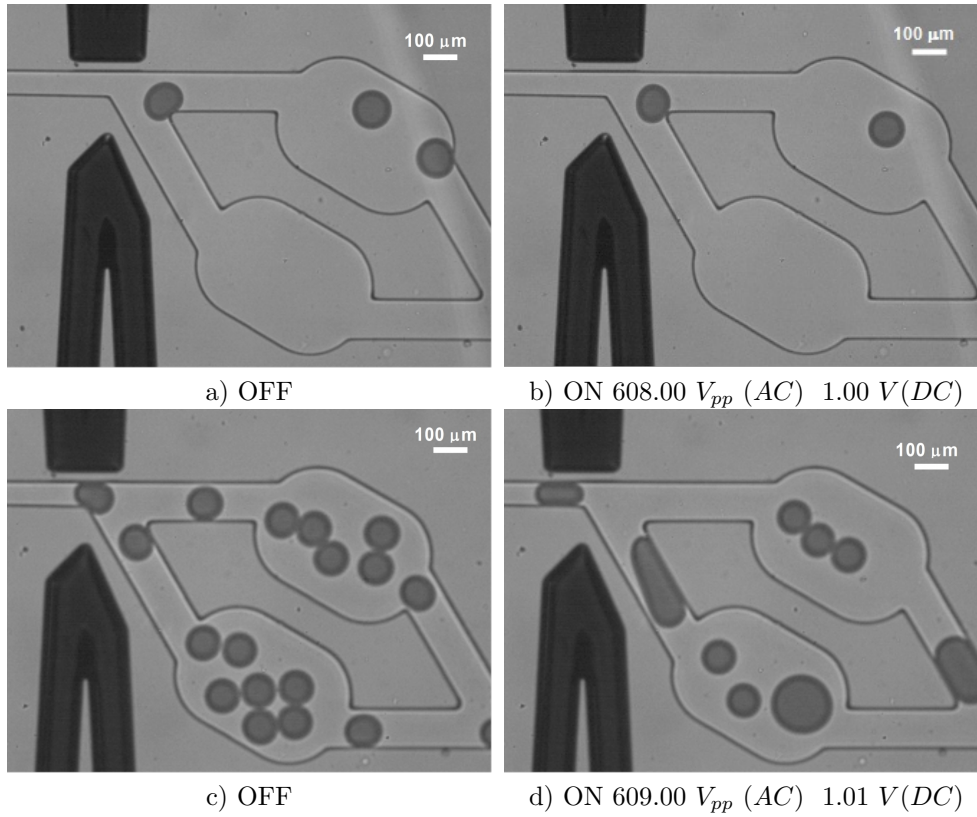
Figure 3.31: Sorting experiments for 3D electrodes, in 40 μm height channels. With low flow rates: a) and b), no visible effects. $\phi_d = 0.06$ $\mu l/min$; $\phi_c = 3.40$ $\mu l/min$; Higher flow rates c), d), reduces spacing between droplets allowing coalescence due to electric field. $\phi_d = 2.00$ $\mu l/min$; $\phi_c = 12.00$ $\mu l/min$.

To allow droplets be spherical at the bifurcation and take advantage of the 3D effect for the electrodes, 100 μm height structures were fabricated. To make a bridge with the 40 μm structures, were tested flow rates with the same capillary number as the previous high and low flow rates (Figures 3.32-c), d) and e), f)). Also it was tested the same low flow rate ($\phi_d = 0.06$ $\mu l/min$; $\phi_c = 3.00$ $\mu l/min$) allowing to analyse droplets with much less speed (Figures 3.32-a), b)).
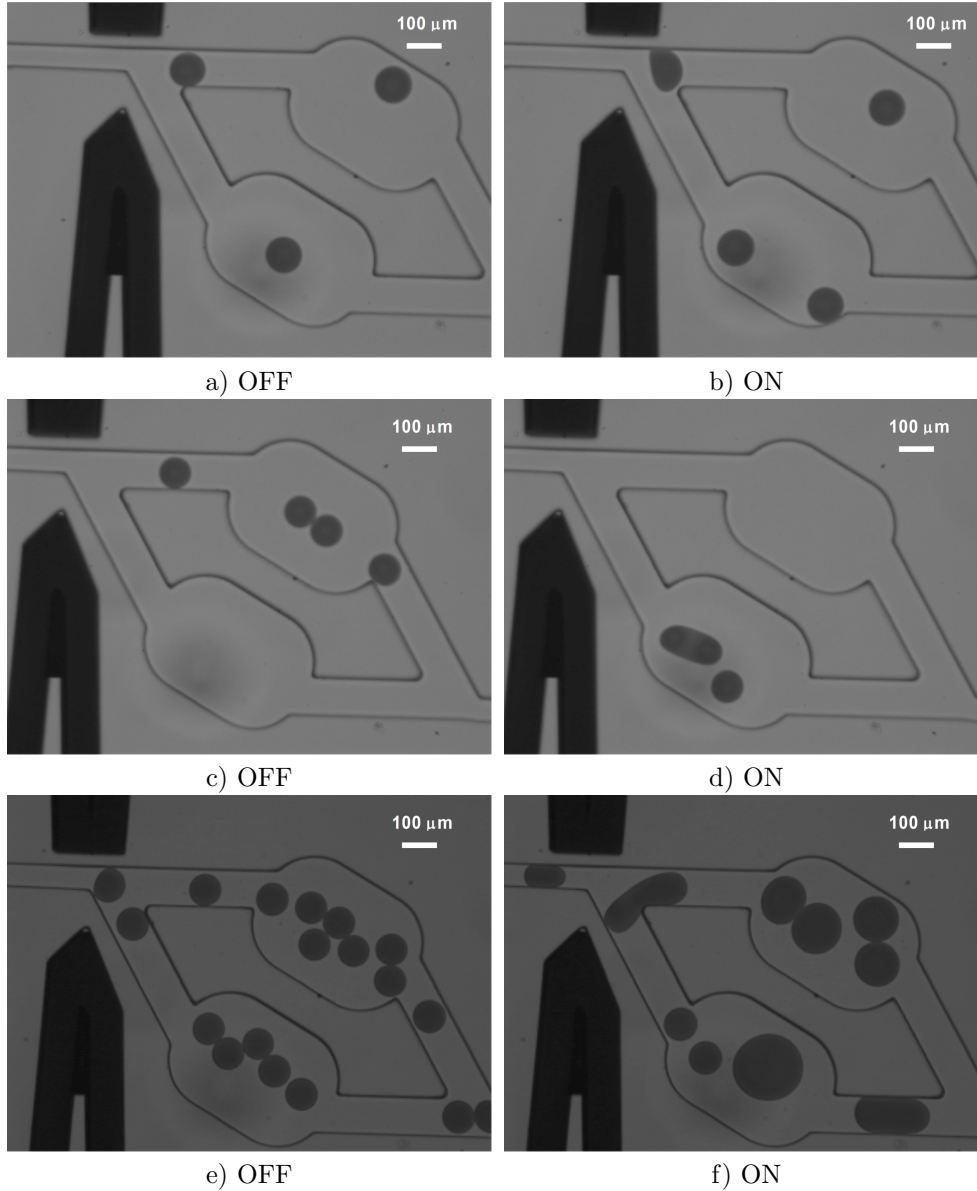
Figure 3.32: Sorting experiments for 3D electrodes, in 100 μm height channels. b) For low flow rate ($\phi_d = 0.06$ $\mu l/min$; $\phi_c = 3$ $\mu l/min$) droplets slow down ; higher ones - d), f) show coalescence. c), d) and e), f) have flow rates to match the same capillary numbers than the previous flow rates tested. c) and d): $\phi_d = 0.15$ $\mu l/min$; $\phi_c = 7.50$ $\mu l/min$; e), f): $\phi_d = 5.00$ $\mu l/min$; $\phi_c = 22.15$ $\mu l/min$. 675.00 V_{pp} (AC) 0.50 $V(DC)$ $f = 200$ kHz.

For the lowest flow rate, it was possible to confirm the deceleration effect (Figure 3.32-b))[18] For the other flow rates coalescence was always observed without proper deflection. Figure 3.32-d) shows just one moment, in really droplets deflected more to bottom than without actuation (Figure 3.32-c)), but wasn't constant in time, a train of droplets deflect down followed by other set that went up. 100 μm height channels seem more promising at this point to allow sorting.

By the previous experiments a lot of insight were collected enabling a new microfluidic and electrode design, such as: bifurcation should be more elongated, so that droplets have more time to deflect (previous structures had 176 μm); sorting by hydraulic resistance is more efficient, and the ratio 1:2 is enough; gradient field of $1.7 \cdot 10^{14}$ $Kg^2 \cdot m \cdot s^{-6} \cdot A^{-2}$ is enough to deflect droplets; channel with height bigger than droplet's diameter seem to work better.

---

[18]The equivalent flow rate for the same speed in 40 μm height channels could not been tested because for flows lower than $\phi_d = 0.06$ $\mu l/min$ syringe pumps became unstable.

Design and Simulations of New electrodes and Microfluidic Structures

The new electrode and microfluidic design was an iterative process with 14 different designs, caming up to the designs in Figures 3.33a)-f). The rational was to first put both 3D electrodes designed before on same side, straighten the triangular tip, than misalignment them -one advanced in relation to the other- and finally rotate in relation to the channel (Appendix C.6). This was done in order to take advantage of the perpendicular gradient and minimize the component that is against droplet flow -which causes stop and coalescence.

Bifurcation has now 771 μm long instead of 176 μm, and 300 μm width instead of a cone shape, this was designed with the intention to give time for droplets to deflect to the streamlines that will flow for the sorter branch (right one on Figures 3.33-a) and b)). These streamlines have a width of 90 μm, and were design for droplets with 80 μm in diameter. Bifurcation angles were kept similar to the previous one (150 °), but the default branch is 10 ° closer to horizontal and the sort one more 10 °, giving some extra momentum sorting effect. At bifurcation, branches have already different widths and the hydraulic resistance difference is also created by their length ratios, 1:2 (full mask in Appendix C.6).

To avoid the cases were droplets stop near to the electrode because flow is low and the field gradient is high, it was place the electrode right next to the opening chamber (Figures 3.33)-c) and d)); droplets should go to the right side of the chamber and they follow the streamlines than go into the right branch. If that didn't work, the second design (Figures 3.33-e) and f)) have the electrode just next to the bifurcation having maximum gradient just before bifurcation. Gradient field magnitude around $1.7 \cdot 10^{14} \ Kg^2 \cdot m \cdot s^{-6} \cdot A^{-2}$ were confirmed for voltages bellow 320 V to assure droplet deflection -this was the gradient magnitude that deflected droplets in previous experiments.
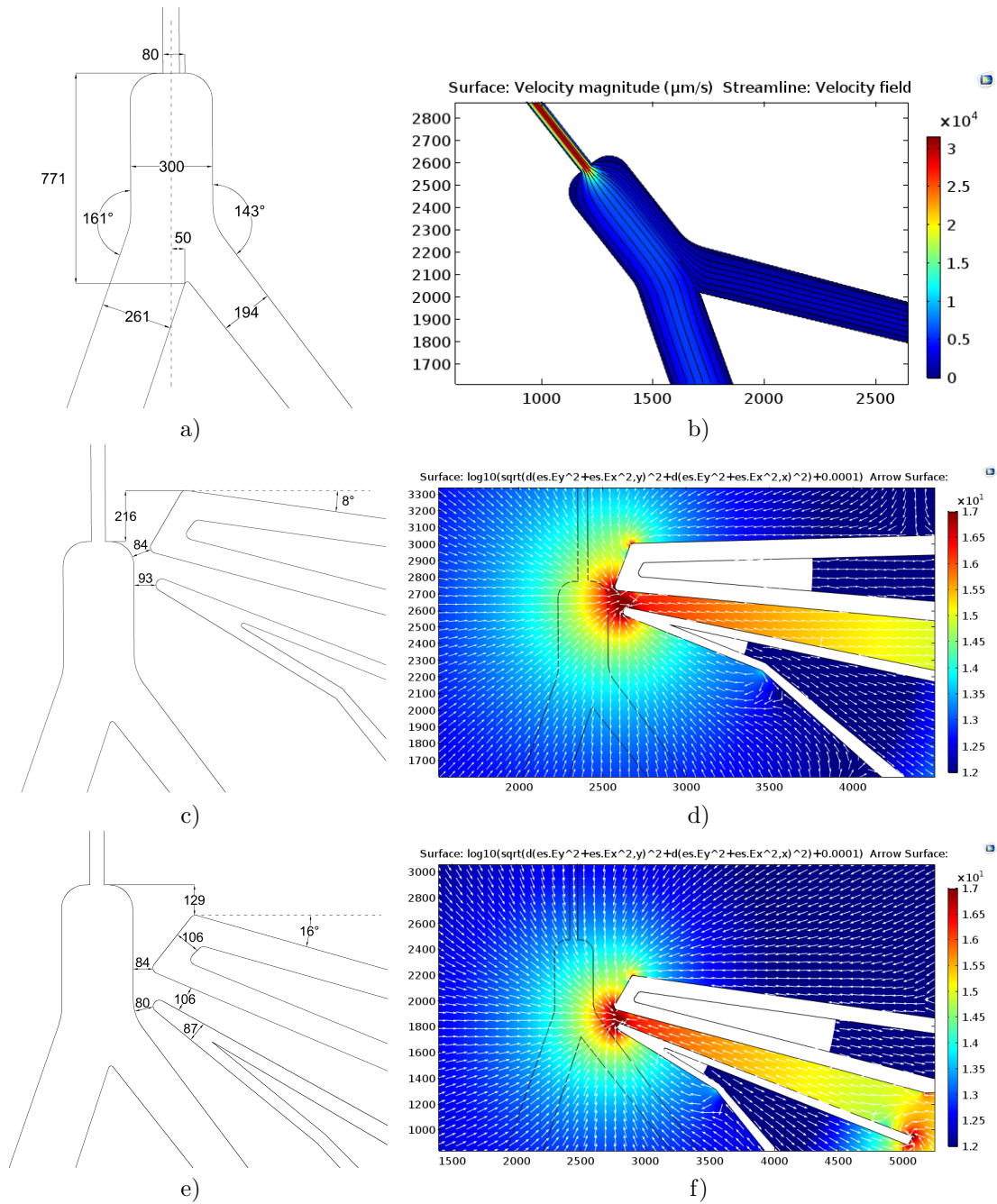
Figure 3.33: a), b) Optimized geometry for microfluidic sorting, and respective COMSOL simulation. New 3D electrode design for two different relative displacements, and respective COMSOL simulations for the same applied field as on Figure 3.29-b.

Experiments with New Electrodes and Microfluidic Structures

The goal with this experiments was to find some conditions that work, and not to fully characterize the system -remember that we were aiming integration[19], and then re-optimize each part if needed. [20] Firstly was checked if the passive sorting with the new bifurcation design (explained in Section 3.2.1) worked.

---

[19]A key aspect is that if the system is not integrated just continuous deflection could be studied. Two study single droplet deflection, high voltage burst duration and timing should be evaluated, microscope cameras have 16.6 ms resolution, which are some hundreds of microns for higher flow rates, thus high temporal resolution is needed to properly characterize this system.

[20]Some photos have droplets in both upper and bottom channel, this is not because sometimes droplets go up and down randomly, happened because recording was being made with 5 s field off and then 5 s on, depending on the flow rate the droplets that suffered other condition than the one being evaluated could still appear. 5 s was chosen because is enough to see the effect stable, although first times were taken recording of 30 s with same condition.

Figure 3.34-a) exemplifies a case where all the droplets flow to the default branch. This design started not to work when droplets are to close to each otherand collide at the chamber misaligning and deviate to the lower branch as shown in Figure 3.34-b). These were experiments in 40 μm height channels, same effect occurs for 100 μm in height.

a)   b)
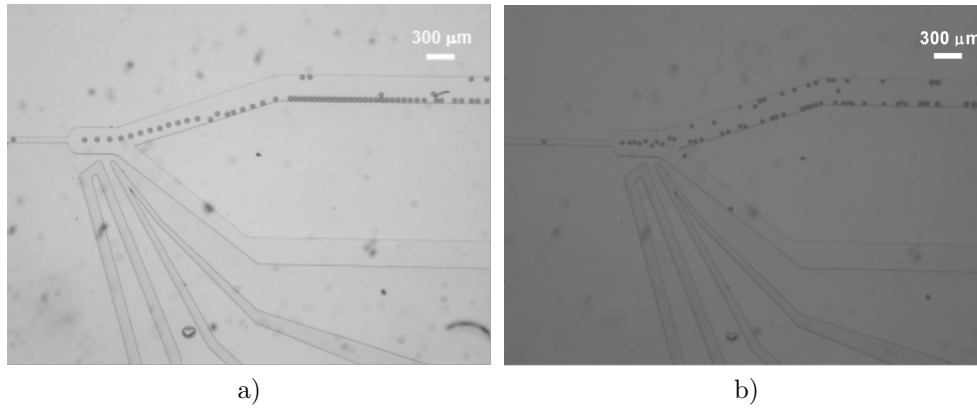
Figure 3.34: Experiments with two different condition, exemplifying: a) passive sorting not working because droplets are to close to each other and start to deviate before bifurcation; b) perfect passive sorting. $height$: 40 μm a) $\phi_d = 0.06$ $\mu l/min$; $\phi_c = 3.00$ $\mu l/min$; b) $\phi_d = 0.06$ $\mu l/min$; $\phi_c = 8.00$ $\mu l/min$.

It was observed that if outlet tubes didn't stay at same height, the variation in pressure is enough to make droplets deflect to the opposite channel. A proper setup with holder for the tubes should be designed for future experiments and also to enable characterization of this effect. To To evaluate if the cause was just the outlet tube heigh difference and not by deformations at the outlet connection with the metal connectors a more flexible tube tube was used (BTCOEX-22), and just by elevating the tip three centimetres sorting was inverted.

Having the passive sorting assured, liquid electrodes where implemented. For the lowest flow achievable ($\phi_d = 0.06$ $\mu l/min$; $\phi_c = 2.40$ $\mu l/min$) droplet deflection is minimum, $\Delta_y \sim 2.4\mu m$ for 600 V_{pp} as shown in Figures 3.35-a) and b). The same insignificant deflection also occurs for the other electrode position.

a) OFF   b) 600.00 V_{pp} (AC) 3.00 $V(DC)$
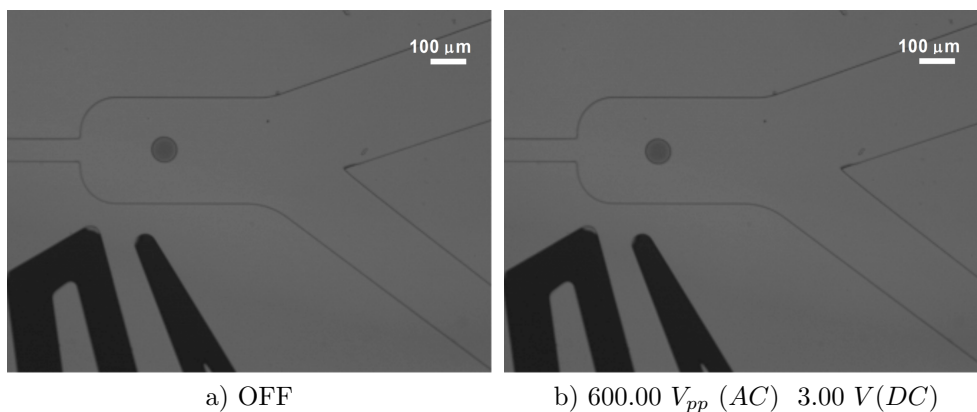
Figure 3.35: Experiment for new design with electrode on the beginning of bifurcation with 40 μm height, no significant shift was observed ($\Delta_y \sim 2.4\mu m$). $\phi_d = 0.06$ $\mu l/min$; $\phi_c = 2.40$ $\mu l/min$.

Figures 3.36-a) and d) compare the trajectory of a single droplet in same flow rate conditions for both electrode alignments. It's clear that the one near to the bifurcation requires less field to successfully sort the droplet. But this doesn't mean that was more suitable for all the conditions. In fact when droplets are really close to each other (Figures 3.37-a) and b)), the configuration with electrode near to bifurcation caused droplet coalescence and the other one didn't, for the same voltage applied 670 V_{pp}[21].

---

[21] When is said that droplets have the same distance, is referent to the distance in between droplets at the down channel, where they are in contact. One can argue that having higher flow rate for the disperse phase cause droplets to be evenly

a) OFF   b) 500.00 V_{pp} (AC) 2.00 $V(DC)$

c) OFF   d) 670.00 V_{pp} (AC) 2.00 $V(DC)$
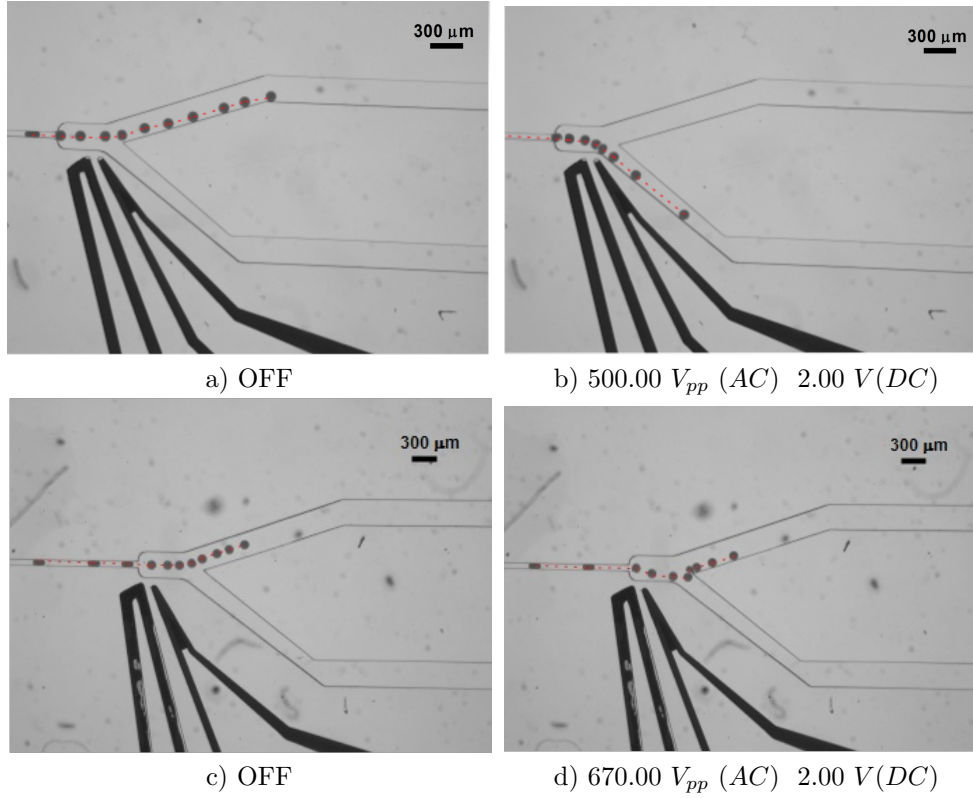
Figure 3.36: Comparison between the trajectories for two relative positions of the electrodes with - b) and d) - and without - a) and c) - applied field. $height = 100\ \mu m$; $\phi_d = 0.06\ \mu l/min$; $\phi_c = 4.00\ \mu l/min$.

By comparing Figures 3.36-a) and c), we can see that droplet's diameter is different indicating that flow conditions were not stable[22]. Also the trajectory is not similar in Figure 3.36-a) droplets go by bottom wall, and in Figure 3.36-c) by the middle of channel. These variation point to the need of a more stable setup that fixes outlet tubes at same level all experiments.

a)   b)
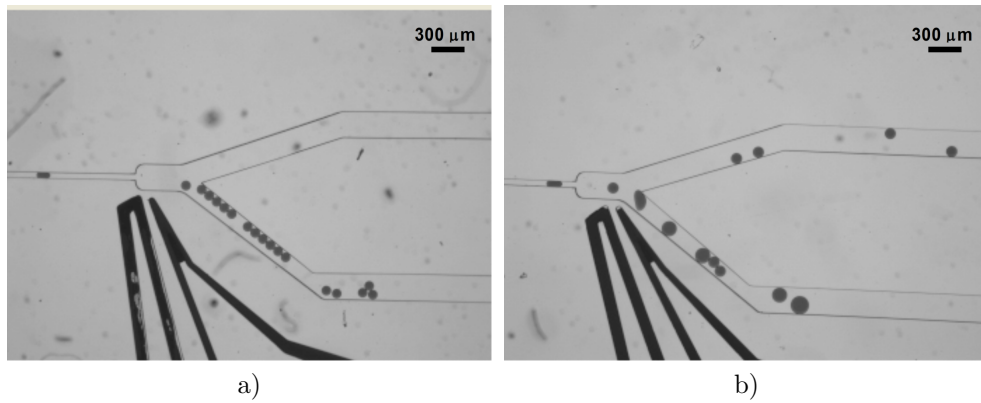
Figure 3.37: Experiment to infer coalescence tendency between the relative position of the electrodes to the channel. Similar droplet distances, and same voltage was applied. a) $\phi_d = 0.1\ \mu l/min$; $\phi_c = 4.00\ \mu l/min$; b) $\phi_d = 0.4\ \mu l/min$; $\phi_c = 6.00\ \mu l/min$. 670.00 V_{pp} (AC) 2.00 $V(DC)$. $height = 100\ \mu m$.

To understand the effect coalescence with voltage for the electrode at bifurcation, were taken photos with steps of 50 V_{pp} starting at voltage bellow the threshold (Figures 3.38-a)-f)). It could be seen that

---

more closer which is true, but notice that the flow for continuous phase increased from 4 to 6 $\mu l/min$ as an attend to avoid coalesce -faster droplets stay less time near where gradient is stronger and less tendency to coalescence occurs- and still it appended.

[22] In each round of experiments flow were tested from low to high to avoid capacitive effects, and waited 1 minute before acquiring video with a new flow rate.

increasing the voltage approximates droplets more to the bottom wall -at 500 V_{pp} was already touching-
and for voltages above 550 V_{pp} coalescence effects started to occur at this flow rate.
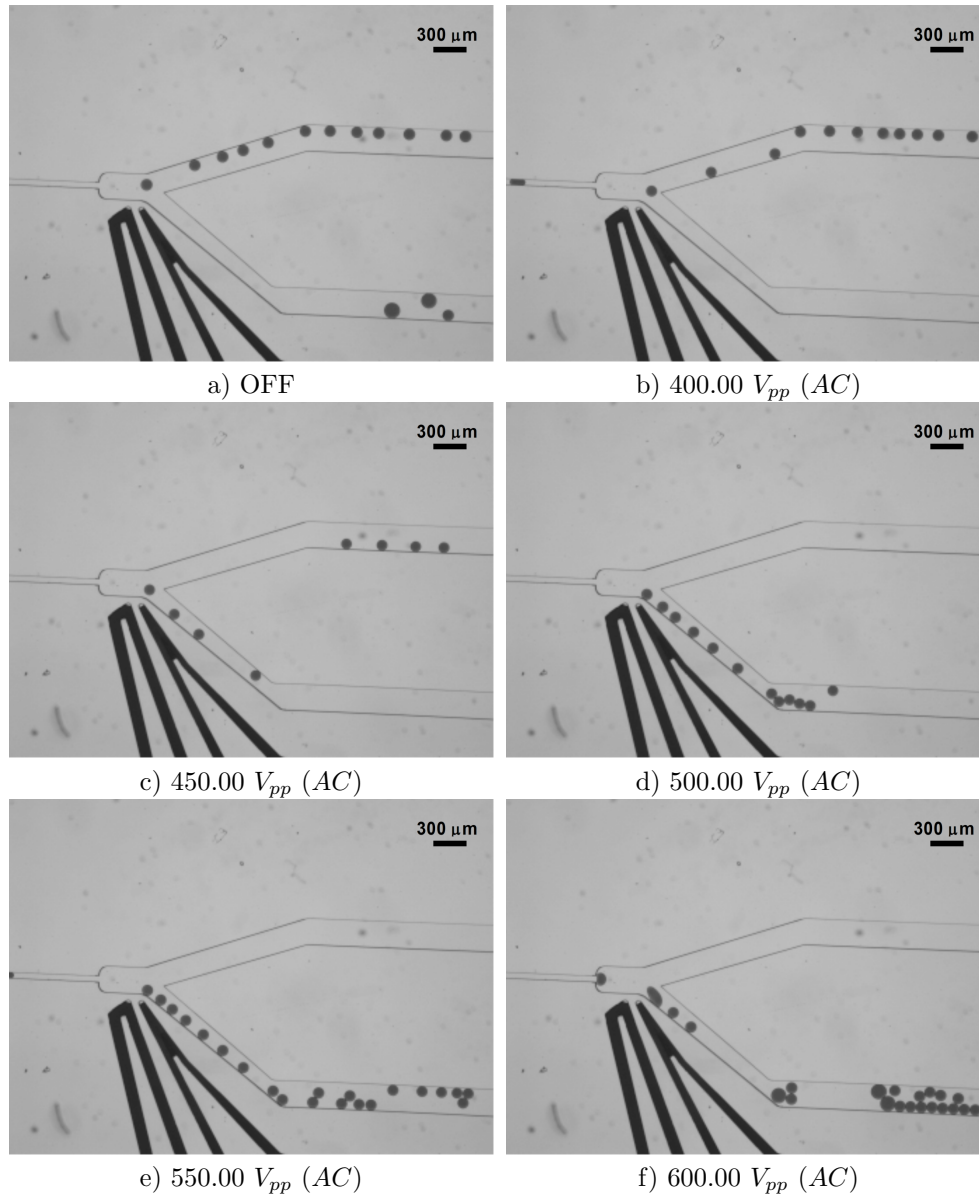
Figure 3.38: Variation of droplet deflection with voltage. $\phi_d = 0.2$ $\mu l/min$; $\phi_c = 4.00$ $\mu l/min$; All DC
components lower than 5 V.

In this Section was confirmed that passive sorting works well, if droplets do not touch each other at
the chamber. Were found conditions for both electrodes to sort droplets with 100 μm structures. For
40 μm not. Electrode alignment at beginning of chamber works better for droplets close to each other
not causing coalescence. Electrode alignment at the bifurcation requires lower voltages and can work for
higher flow rates but can cause coalescence if droplets aren't spaced enough. Example of a microfluidic
structure filled with liquid metal can be seen in Appendix C.6.

3.2.2 by Pneumatic Actuation

Pneumatic sorting experiments came by inspiration. They were performed when the HVAC was being
built. It took a bit of time, and one day I remembered to try to actuate the channels that were designed
for the liquid metal electrodes, with compressed water. The valves were actuated manually to find
condition that work in continuum. For integration, delay time had to be characterized. To characterize
each condition, Matlab script was developed to recognize droplets inside each chamber and do automatic

counting (information about script in Appendix B.2).

Finding Best Working Conditions

Figure 3.39 shows the variation of droplets inside each chamber with time for a specific flow rate, $\phi_d = 0.1\ \mu l/min$; $\phi_c = 10.00\ \mu l/min$, and pressure 0.36 MPa. Three combinations were possible for channel dilatation: top channel, bottom channel and both. Between each combination both channels were deactuated, restoring the deformation to zero.

The blue an green rectangles represent the areas that droplets inside were counted, all the yellow circles were false positives that weren't counted. In the graph, blue line corresponds to the counting inside blue rectangle, the same for green line and rectangle. It was assured that both rectangles had same area, and that each analysed frame had a totally different group of droplets. Figure 3.39 tells information about the stability of measurements. The percentage indicated, is a time average for all the frames that had the same valve condition, related with the number of droplets at the blue rectangle. By repetition of the last condition three times, is possible to see that the sorting percentages are coherent. Some oscillation occurs for the case of both electrodes off, just meaning that the flow rate was not optimum for the bifurcation geometry.
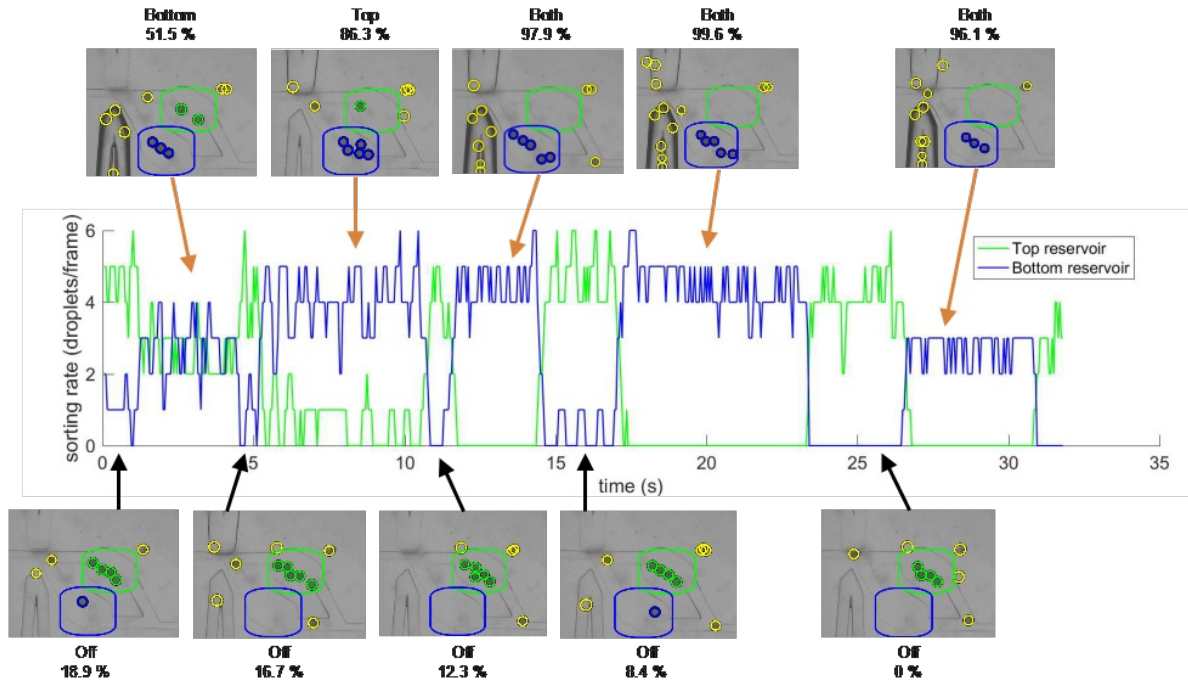
Figure 3.39: Variation of sorting rate with time, for different valve combinations. Percentages are related to the bottom channel. $Height = 67.7 \pm 1.3\ \mu m$, $\phi_d = 0.1\ \mu l/min$; $\phi_c = 10.00\ \mu l/min$; Valve actuation Pressure 0.36 MPa.

.

More conditions were tested for pneumatic sorting and best conditions are summarized on Table 3.2. Percentage of sorting refers to the relative amount off droplets that went for the bottom electrode, with the best of three possible combinations of channel deformation. Percentage of droplet with sorter off refers to the percentage of droplets that went by the down channel with valves turned off.

It was clear that 40 μm height channels performed better, having total efficiency for status on and off. Three different flow rates were tested intending to check for high low and medium droplet frequency, droplets with radius ranging 29.7 μm to 34.8 μm were successfully sorted. Images representing these conditions can be found on Appendix B.1. For the bigger height, $67.7 \pm 0.3 \mu m$ several effects were analysed. The effect of pressure (and consequently deformation) was compared using a flow rate of $\phi_d = 0.1\ \mu l/min$; $\phi_c = 10.00\ \mu l/min$; increasing from the minimum effective pressure , 0.2 MPa, to almost the maximum available, 0.36 MPa, sorting performance increases from 78.8 % to 99.6 %. Default sorting was really improved by raising the continuous phase flow rate, from 29.5 % and 49.1 % for 0 %.

For similar total flow rates, conditions 1st (7.1 $\mu l/min$) and 4th (6 $\mu l/min$), smaller droplets sort better (just 58.9 % of the 63.4 μm droplets were sorted in comparison with the 82 % of 54.5 μm droplets with more 0.6 MPa of valve pressure).

Table 3.2: Comparison for the best conditions found for pneumatic droplet sorting.

height (μm)	ϕ_d ($\mu l/min$)	ϕ_c ($\mu l/min$)	Press. (MPa)	Rad. (μm)	Sort. On (%)	Cond.	Sort. Off (%)
67.7 ± 0.3	0.1	7	0.3	41.92 ± 0.50	82.0	both	29.5
		10	0.2	38.47 ± 0.41	78.8		0.4
			0.36		99.6		0
	2	4		53.92 ± 0.75	58.9	bottom	49.1
40.4 ± 0.1	0.06	3	0.36	29.70 ± 0.15	100	bottom	0
	0.07	4		34.80 ± 1.48			
	0.17	9.2		32.37 ± 0.67			

The deflection mechanism may seem a bit counter intuitive. By actuating the bottom valve we are constricting the bottom channel, increasing its hydraulic resistance, thus expecting droplets to flow by the upper channel. A possible explanation for the downwards deflection, is that the valve expansion is not sufficient to increase hydraulic resistance on the bottom branch but the strangulation created increases fluid velocity at the beginning of the branch, lowering the pressure and sucking the droplet. Also should be noted that disperse phase have lower density than continuous phase (1000 kgm^{-3} vs 1614 kgm^{-3}), and shear gradient lift force may dominating wall lift force[78, 79].

Valve Actuation's Delay

Understanding how fast did the valves inflate and deflate will give information on how fast droplets can sorted, and if integration was desired, how far away upstream should the sensor be placed for compensate the delay. To evaluate these delays a led was activated when the solenoid valve was powered (scheme in Figure 3.40). The difference between the last frame with valve unpowered (black) and the first with the valve fully expanded gave the delay time. The uncertanty was related to the frame rate. The Microscope camera records at 60fps, because the computer did not record at constant rate the PC monitor 200 fps rate was chose. Each experiment was repeated 5 times and the error is the standard deviation of these measurements.
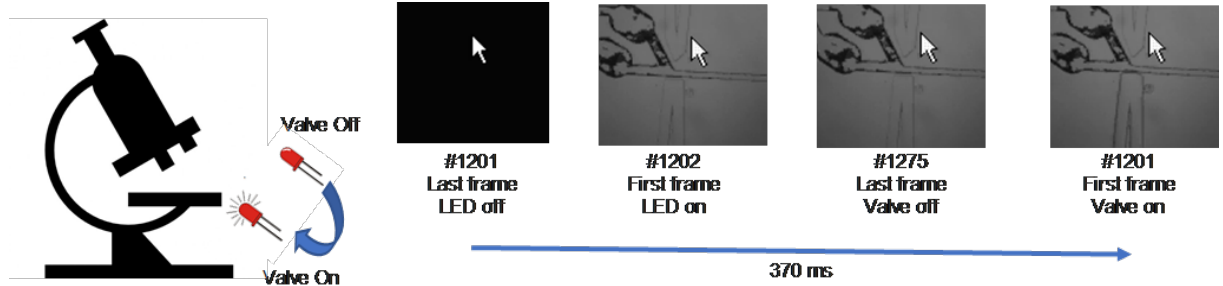
Figure 3.40: Schematic of valve's delay study. Camera recording at 60 fps (2x2 Binning mode) and screen capturing at 200 fps.

.

Table 3.41 summarizes the delay characterization. Higher pressure decreases delay time. Valve deflation delay wasn't characterized, but should be if pneumatic integration is pretended.

Figure 3.41: Delays time between actuation and full valve expansion. For 1:10 pdms:curing agent.

State	Pressure (MPa)	delay (ms)
Off $\rightarrow$ On	0.3	393.3 ± 20.1
	0.4	249.0 ± 23.2

Pneumatic actuation have significant delays, droplets achieve easily several hundreds of microns per second on these channels. De-pressurization delay should also be characterized, as it will also contribute

for the actuation rate, but is enough to see that some improvements should be made if pneumatic actuation is desired, mainly at the solenoid valves that actuate the system, because microfluidic valve inflation is from one frame to another ($t < 16.6\ ms$), but from pressing the button till that moment hundreds of milliseconds are required.

3.3 Droplet Detection with a-Si:H Photoconductors

Aiming at integration, squared 50 μm side photoconductors from Denis Santos[68] were used. Sensor characterization can be found in Section 2.2.4. First was used the sensors with microscope confirmation, after was studied how to lower the noise and finally was studied the variation of signal with dilution of the colourant.

3.3.1 Experiments with Droplets

To be able to confirm that the signal measured was from the droplets a shielding box for the sensor be under the microscope was built (Figure 3.42-b)). It was used the microscope lamp as light (white) source and the Pre-Amplifier to amplify the signal. To bias the sensors it was applied 5 V by hp E3612 Power Supply..

a)   b)
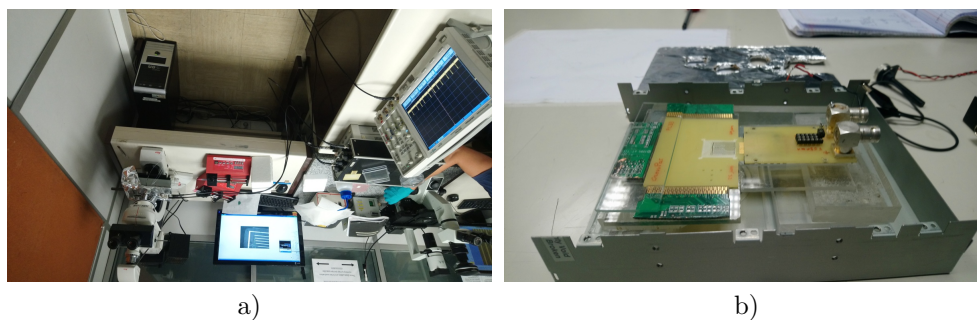
Figure 3.42: a) Complete view of the first setup used for detection of droplet with Photoconductors. b) Faraday Cage build to isolate photosensors from electrical noise.

Figures 3.43-a) and b) were a fingerprint, on the left is a video frame with the microfluidic channel aligned with the sensor, with one droplet already passed, one plug covering the sensor and more three coming; on the right is the respective photosensor signal. It clear identifies the first droplet followed by all the plugs and other droplet after some time. The signal didn't drop till zero because droplets are green and light is white[23].

a)   b)   c)
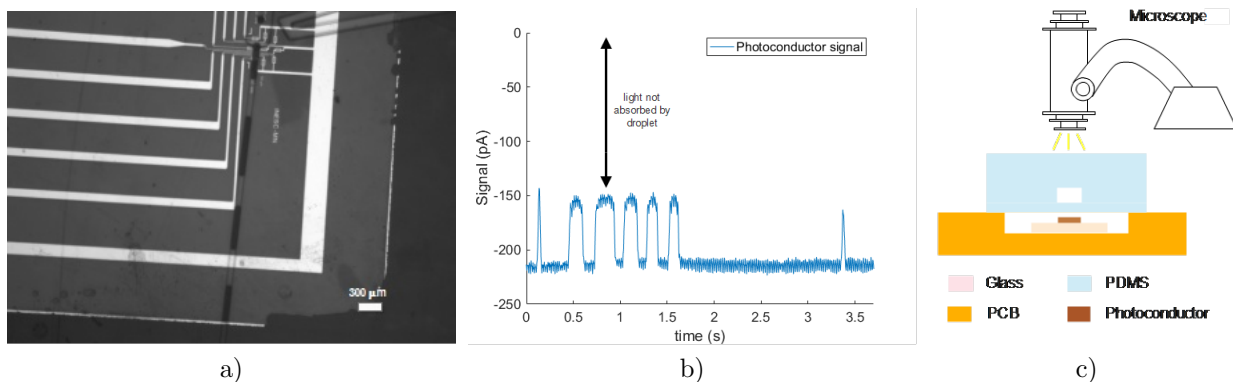
Figure 3.43: b) Photoconductor signal for a droplet followed by 5 plugs and then other droplet, as seen on the microscope image, a) 5V bias; 10^{10} V/I gain. c) Schematic view of experimental setup used.

---

[23]With filter to pass just red light the signal went to zero, but the filter also cuts the emission light which in this case is the same cause no fluorescence was used, thus was not possible with filters have sensor signal and microscope imaging for this setup

For $\phi_d = 0.5$ $\mu l/min$; $\phi_c = 3.00$ $\mu l/min$ (Figure 3.44), droplets have a frequency of 15 Hz which start to approximate with the 50 Hz noise of electric network. The Fast Fourier Transform in Figure 3.44-c) show the peak for the 15 Hz followed by its first three harmonics (it's a square signal) and then the 50 Hz and its harmonics appear. To amplify fast, rise time should be reduced, which caused more noise to appear and be amplified. This setup started to show its limitations, although having the big advantage of allowing to video record in parallel with sensor acquisition.

a)   b)   c)
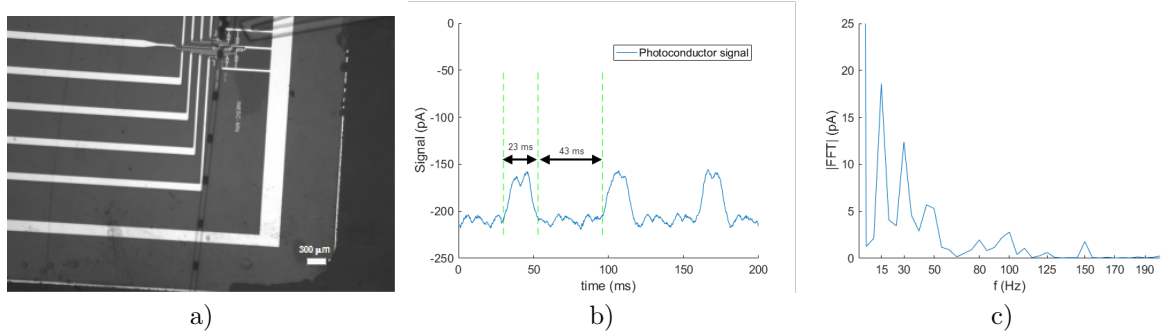
Figure 3.44: a) Microscope image for $\phi_d = 0.5$ $\mu l/min$; $\phi_c = 3.00$ $\mu l/min$, and respective Photoconductor signal, b). c) Fast Fourier Transform from the signal in b), indicating droplet frequency at 15 Hz.

3.3.2   Setup Optimization and Noise Reduction

The setup was changed to reduce noise and excitation light is at the maximum of abortion of green dye, 629 nm (see Figure 2.5). The Faraday cage is now a steel server box with 3 mm thickness (more information explained in Section 2.2.4). Figure 3.45 show the advantage of increasing the voltage and reducing the gain, reducing the gain by 10 and increasing the voltage by 10 gives a signal with the same amplitude but SNR changes from 2 to 36[24]. Also, analysing in frequency (Figure 3.45-b)), for the higher gain is possible to see the peaks for 50 Hz noise and other frequencies that are not multiples of the droplet frequency (noise therefore).

a)   b)
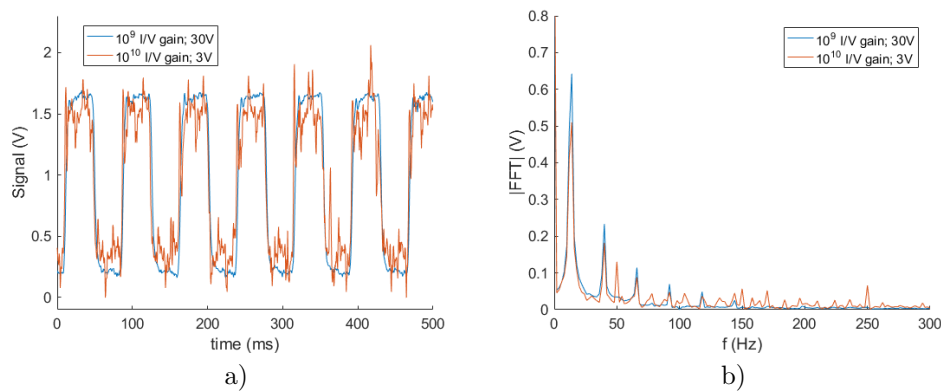
Figure 3.45: Signal comparison for different gains and voltages applied on Photoconductor with droplets flowing on top. $\phi_d = 0.5$ $\mu l/min$; $\phi_c = 3.00$ $\mu l/min$.

3.3.3   Study of Signal Intensity with Droplet's Dye Concentration

In a real directed evolution experiment, for example some of the droplets will have more concentration of a certain analyte which will cause bigger signal. In order to have an estimative of the sensibility of the setup, different dye dilutions were tested and absorbance was calculated [25]. Absorbance was calculated from Equation 3.1.

---

[24]Notice that these experiments work with high luminosity conditions. For experiments where low luminosity occurs, the increase of voltage will increase photoconductors dark current, and that may be prejudicial.

[25]Effects of reflection on the droplets and oil, and oil absorbance in 629 nm aren't taken in consideration.

$$A = log_{10}\left(\frac{\phi_i}{\phi_t}\right) \tag{3.1}$$

Where the incident light signal, ϕ_i, was the amplitude of the peak created by the chopper (completely blocks light), and the transmitted light ϕ_t, was the $signal_{chopper} - signal_{droplet}$. Figures 3.47-a) and b) show simultaneously chopper and droplet signals for two different concentrations. The sensor was aligned in channels with 60 μm width and 100 μm height, droplets have a parallelepiped shape (like in Figure 3.43-a)). Figure 3.46 shows absorbance variation with dye's dilution, ranging from 1:0 till 1:1000, measured by the a-Si:H photoconductors and simultaneously the microscope image. Also the green line represents the signal from the droplet's water in oil interface. Droplets do not present all the same size although the system was stable when photos were acquired, indicating that the dye's concentration is influencing the fluid properties.This should not be a problem when using cells, because droplets form before the reaction occur. The four lower concentrations have a linear behaviour that was characterized by a linear fit, parameters are in Table 3.3. The uncertainty is big due to electrical noise.
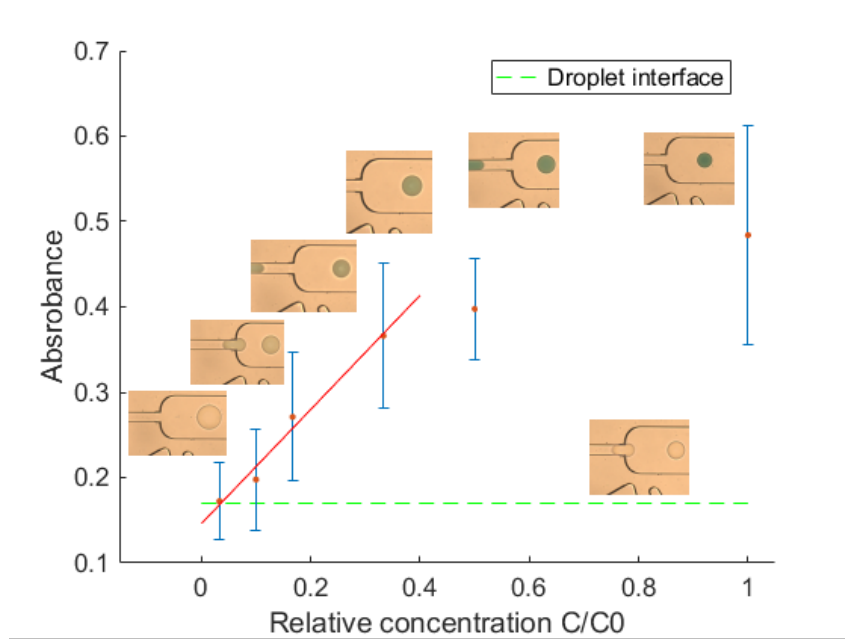
Figure 3.46: Variation of the relative signal caused by droplet with the one from chopper (zero light) with concentration of dye. $\phi_d = 0.5\ \mu l/min$; $\phi_c = 3.00\ \mu l/min$; 30 V bias; 10^{10} V/I gain.

Table 3.3: Parameter for linear fit $y = m \cdot x + b$ at 4 first point in graph of Figure 3.46. Values presented for 95 % confidence interval.

m	b	χ^2
0.67 ± 0.39	0.15 ± 0.05	0.98

It's interesting to see that for low concentrations, the effect of droplet/oil interface is visible, Figure 3.47-b) shows the signal of a droplet with 30 times less concentration. In the middle of the signal is a valley that corresponds to the actual droplet signal, the two extremes are the signal caused by the droplet interface. Once again, if the amplification is fast enough, the sharp transition are possible to be analysed and lower concentration will be detectable.
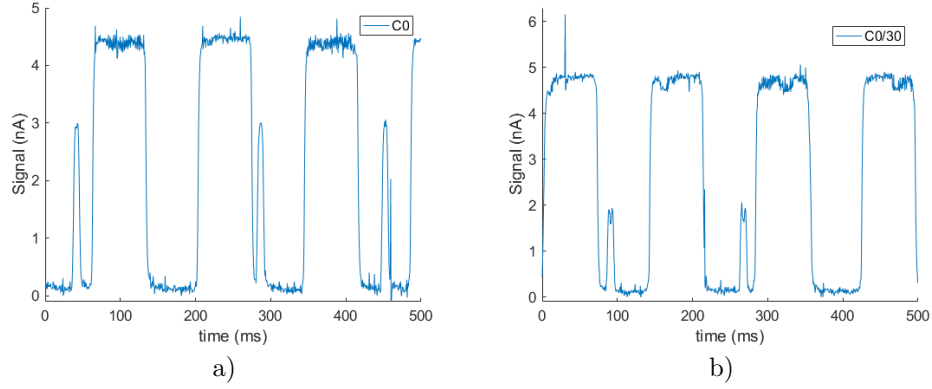
Figure 3.47: Examples of the signals caused by chopper - higher amplitude - and droplet passage,for: a) no diluted dye; b) diluted 30 times. Chopper 7 Hz; $\phi_d = 0.5~\mu l/min$; $\phi_c = 3.00~\mu l/min$; 30 V bias; 10^{10} I/V gain.

3.4 Integration of a-Si:H Photoconductor with Dielectrophoresis Actuation

An integrated system with detection and sorting requires data acquisition, precessing and actuation. To conjugate these information microcontroller was used. In this section are discussed the key steps to integrate the two modules. First was designed a transimpedance circuit, to allow portability; after the delay between the modules was characterize; finally both were tested together.

3.4.1 Design and Fabrication of a Transimpedance Amplifier Circuit

Previous Section 3.3 gave information about the magnitude of current signals -for 3 V bias $1V*10^{-10}I/V = 10nA$- and by considering that the microcontroller used was teensy 3.6, the final output signal had to be between 0 and 3.3 V. High gain (200 dB) and low frequency response is needed to start to use the system.

The final circuit implemented is on Figure 3.48. Photoconductor is bias by the 3.3 V microcontroller's supply, the signal is converter from current to voltage by the first stage amplifier -where most of the gain is-, some high frequency noise is cuted by a Low pass filter before amplifying the signal again to meet the 0-3.3 V window of teensy 3.6; other filter is applied to clean the signal facilitating the posterior use of a threshold voltage to trigger electrodes[26].

---

[26]some fast spikes of voltage went above threshold voltage triggering the the signal not always at the same time.
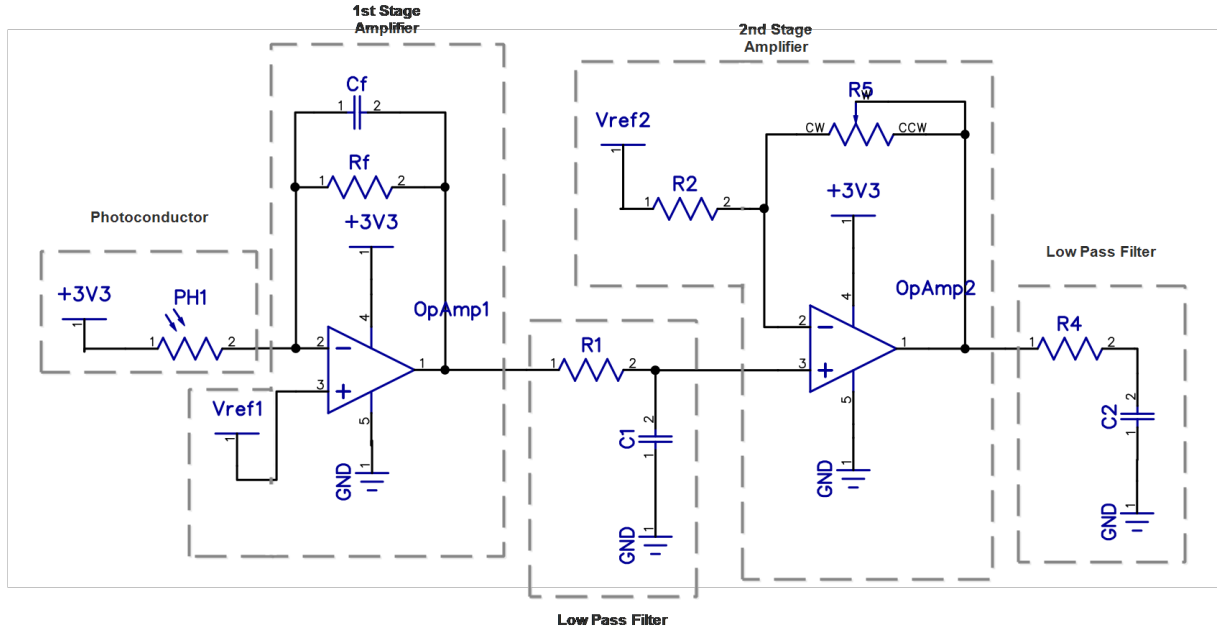
Figure 3.48: Schematic of the transimpedance circuit used to amplify the signal from the Photoconductor.

The current generated by the Photoconductor is given by Equation 3.2

$$i_{signal} = \frac{3.3 - V_{ref1}}{R_{PC}(luminosity)} \tag{3.2}$$

where the photoconductor resistance, $R_{PC}(luminosity)$, depends on luminosity conditions. The signal is then converted from current, i_{signal}, to voltage, v_{out}, in the first stage amplifier as described by Equation 3.3.The circuit behaviour is frequency, f, dependent.

$$v_{out} = V_{ref1} - i_{signal} \cdot \frac{R_f}{1 + 2j\pi f R_f C_f} \tag{3.3}$$

The low pass filter behaviour is characterized by Equation 3.4.

$$v_{out} = \frac{V_{in}}{1 + 2j\pi f R_{1,4} C_{1,2}} \tag{3.4}$$

The second stage amplifier by Equation 3.5.

$$v_{out} = V_{in} \cdot \left(1 + \frac{R_3}{R_2}\right) - V_{ref}\frac{R_3}{R_2} \tag{3.5}$$

For a frequency smaller than the cutoff frequencies, $f_{cuttoff/3dB} = 1/(2\pi RC)$, filter effects could be despised. The gain and offset of the circuit is obtained by conjugating the Equations 3.4 and 3.5.

$$v_{out} = \frac{R_3}{R_2}(V_{ref1} - V_{ref2}) + V_{ref1} - i_{in}R_c\frac{R_3}{R_2} \tag{3.6}$$

V_{ref1} and V_{ref2} are controlled by the DAC of teensy 3.6, and both setted to 1.61 V (2000 in 2^{12} bits), although this decreases the amount of bias voltage to the photoconductor ($3.3 - 1.61 = 1.69 \ V$ allows higher range for the signal, because the gain is manually compensated by the potentiometer $R_3 = 1 \ M\Omega$ ans $R_2 = 100 \ \Omega$. C_f is 1 pF and R_f 100 $M\Omega$, having a cuttoff frequency of 1.59 kHz. The RC filters are composed by $C_{1,2} = 10 \ nF$ and $R1, 4 = 20 \ k\Omega$ cutting at 795 Hz. High speed Op-amp with single supply, OPA-350 were used.

It required some careful mounting to avoid noise. Implementation on a perfurated board is shown on Figure 3.49-a). Overlapping between ground and 3.3 V was avoided at maximum, when necessary was crossed to avoid capacitance effects. For the first stage amplifier, feedback resistance and capacitor were welded near to the Op-amp output connection, to reduce noise[80]. Also some oscillation appear if the capacitor is not well chosen, due to parasitic capacitance of the photoconductor[81]. The frequency

response of the circuit is shown on Figure 3.49-b), measured with chopper generated signal. The behaviour is not ideal as the amplification starts to decrease for frequencies around 40 Hz, but still works for the previous conditions (till 15 Hz) as show in the Figure 3.51.

a)   b)
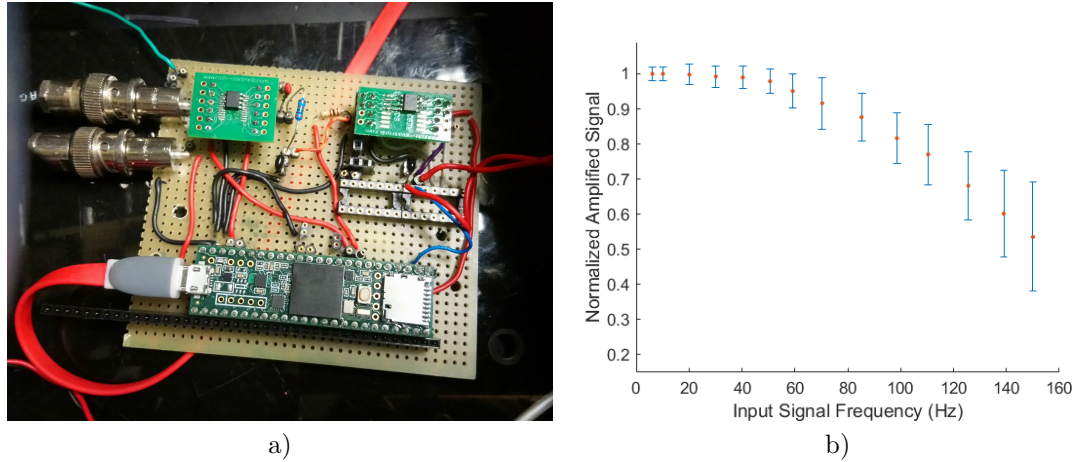
Figure 3.49: a) Mounting of circuit represented in Figure 3.48 . b) Frequency response of the circuit.

3.4.2   Characterization of Integrated System's Delays

Similar to the pneumatic study, here is also important to have an idea about the delays between each module, to predict the sensor to electrode distance and to improve one of the modules if needed. Figure 3.50-a) schematizes the system between droplet detection, all the modules that signal has to got through till the sorting region where electrodes are actuated. Figure 3.50-b) shows the different modules: signal actuates de photoconductor[27] and is amplified (first delay), when it reach the threshold voltage micro-controller sets the trigger pin -switches from 0 to 3.3 V- (second delay), Ac source will receive the trigger and start a burst of n cycles (third delay), this will generate the high voltage signal that actuates the electrodes (fourth delay).

a)   b)
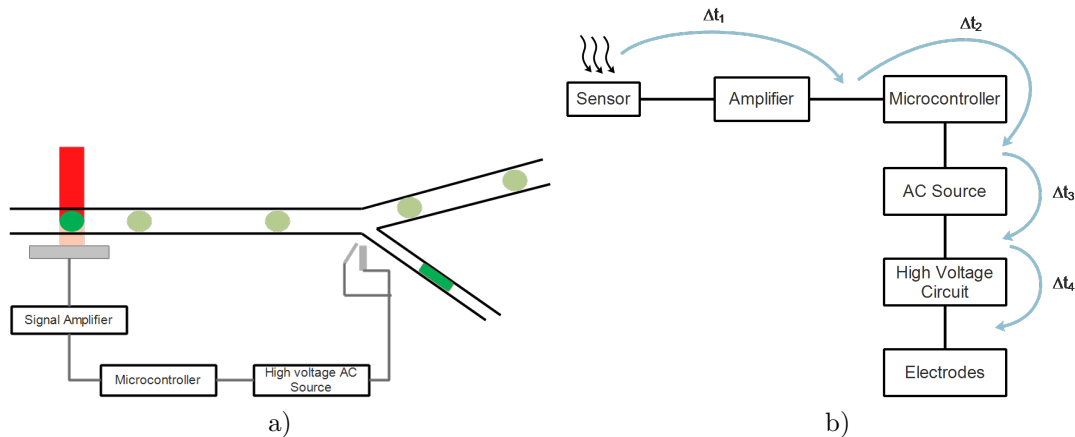
Figure 3.50: a) Representative scheme on integration between detection and sorting. b) Various modules evolved between the light blocking by the droplet and the actuation on the electrodes.

Delay Between Light and Amplified Signal

TIA circuit may be modified to read simultaneously two sensors, Pre-Amplifier cannot, allowing to estimate droplet velocity and correct the actuation delay in case of flow rate instability. that was the reason why delay between light signal and amplified signal was characterized for the TIA circuit. The light signal was created by chopper, and was measured the time between no light (chopper 0 V) and full

---

[27]Here could been a delay that was not characterized.

rising of amplified signal (Amplified signal 3 V[28]). Delay was greatly dependent on the cutoff frequencies (inversely proportional to rising time) of the circuit, 7.00 ± 1.71 ms. Delay with the Pre-amplifier is around 240 μs range (see Section 2.2.5). Figure 3.51 shows the delay between input signal and amplified signal.
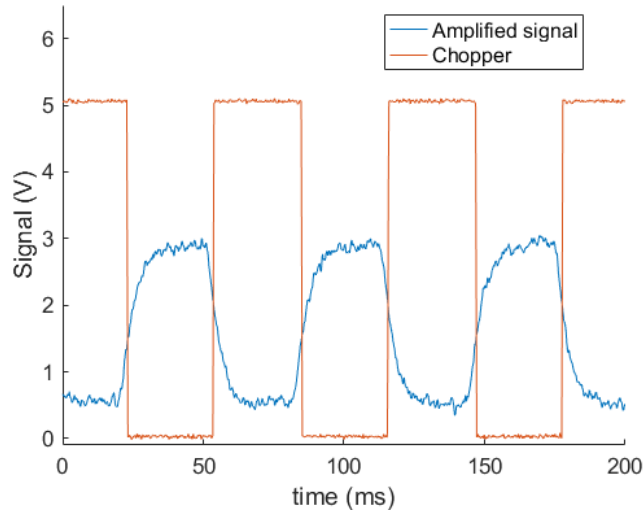
Figure 3.51: Variation in time of the amplified signal caused by chopper blockage. Chopper blocking light corresponds to 0 V. No light amplied signal corresponds to $\sim$ 3 V.

Delay Between Amplified Signal and Microcontroller's Response

After the signal was amplified a analog port of teensy 3.6 received the signal and when above the setted threshold voltage, 1.5 V in Figure 3.52, turned on, 3.3 V a digital port. It was seen that the amplified signal drops several mV after the trigger meaning that some current-compensator capacitor was needed. Measured delay was 51.23 ± 6.13 μs.
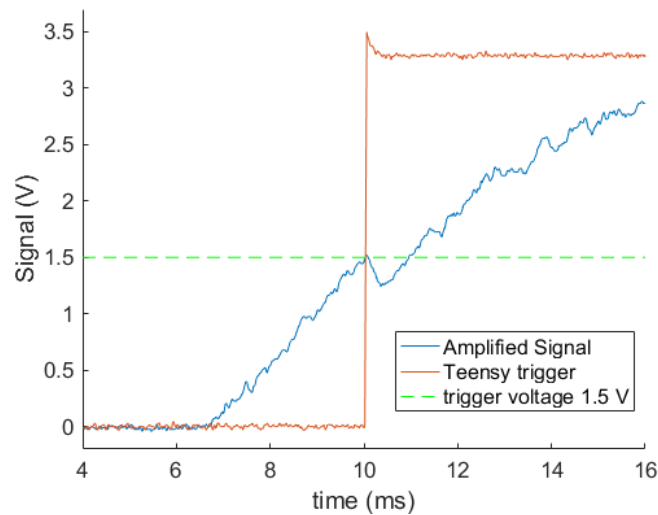
Figure 3.52: Delay between the amplified signal - when reach the trigger voltage - and the output trigger.

Delay Between Microcontroller's Response and AC Source's Burst

Microcontroller triggers the Ac source, which triggers HVAC signal. The AC signal is setted according to each output signal frequency. Signal amplitude and frequency are the variables. To facilitate the

---

[28]Here the signal changes between 0 and 3 V and not 0 to 1.5 V because the current variation is bigger, chopper completely block light, droplet not

visualization a squared signal for AC Source is used, but in the HVAC signal is sinusoidal, the delays didn't change with the shape. Figure 3.53 shows this delay.
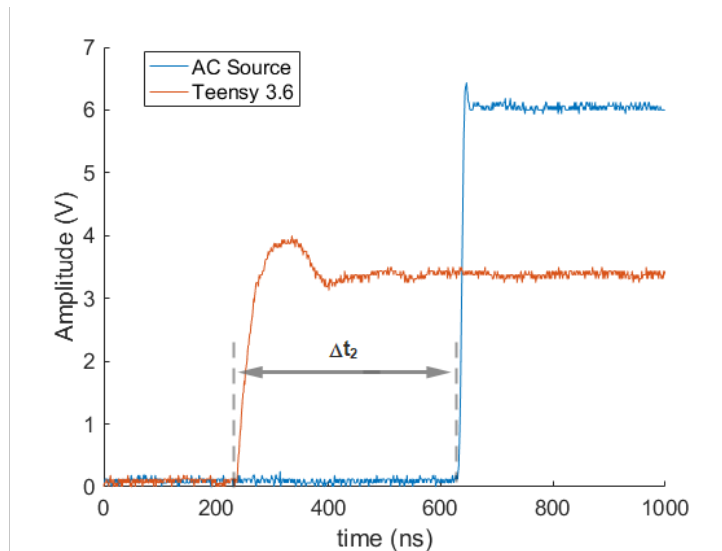
Figure 3.53: Transient view of the delay between teensy trigger and AC source signal - square wave.

The delays decreased almost 1 μs from 1 kHz to 100 kHz signal. At the hundred of kHz delay stabilized around 400 ns as shown in Figure 3.54-a). Increasing the signal amplitude from 10 mV_{pp} to 10 V_{pp} just changed the delay 25 ns, decreasing with voltage increase (Figure 3.54-b)).
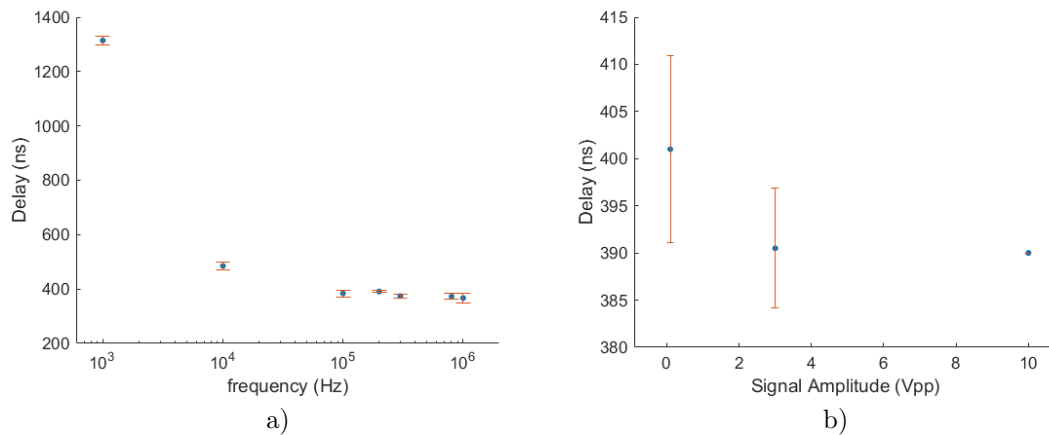
Figure 3.54: a) Variation of delay between teensy trigger and AC source signal with: a) output frequency (amplitude 3 V_{pp}) and b) voltage (300 KhZ).

Delay Between Microcontroller's Response and High Voltage Burst

To facilitate the delay analysis, it was measured the delay between trigger (sharp signal by the microcontroller) and high voltage signal, meaning that two delays were summed as shown in Figure 3.55. Because signals had dispar amplitudes, each one was normalized to its maximum amplitude, always present in each plot's legend. To deflect a droplet, the signal should stay on for a specific amount of time, this time was controlled by the number of cycles per burst, and was setted at the AC Source. Also after the burst there is a delay to turn off related with the HVAC and electrodes discharging time; Figure 3.56-a) shows both on and off delays.
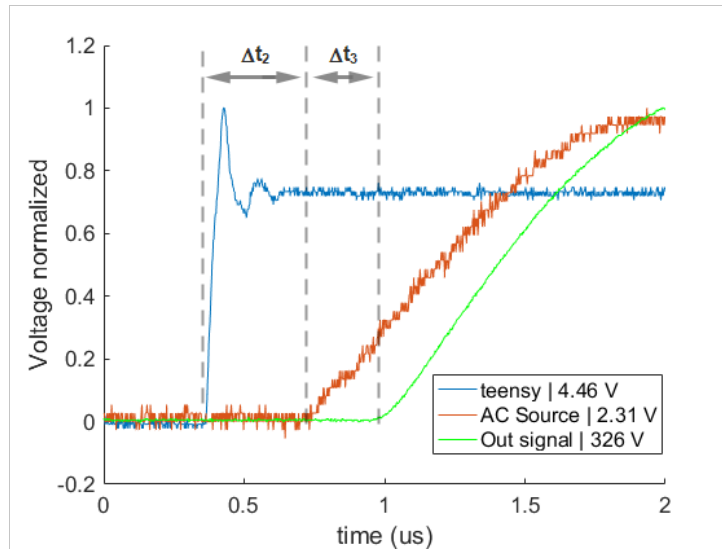
Figure 3.55: Transient view of the delays between teensy trigger to AC source signal, Δt_2, and between AC source and high voltage output signal, Δt_3 . Normalized voltages.

Delay time (on and off) do not change[29] with the number of cycles -ere tested bursts of 1, 10 and 100 cycles at 200 kHz, Figures 3.56-A), b) and c). Also was evaluated signal amplitude stability to assure that voltage is the same as in continuum mode, frequency is always similar[30] to continuum mode (Figure 3.56-d)

---

[29]Saying that don't change means that are contained by the distribution errors.

[30]For one cycle burst 6 V difference was observed, but this condition will never be used.
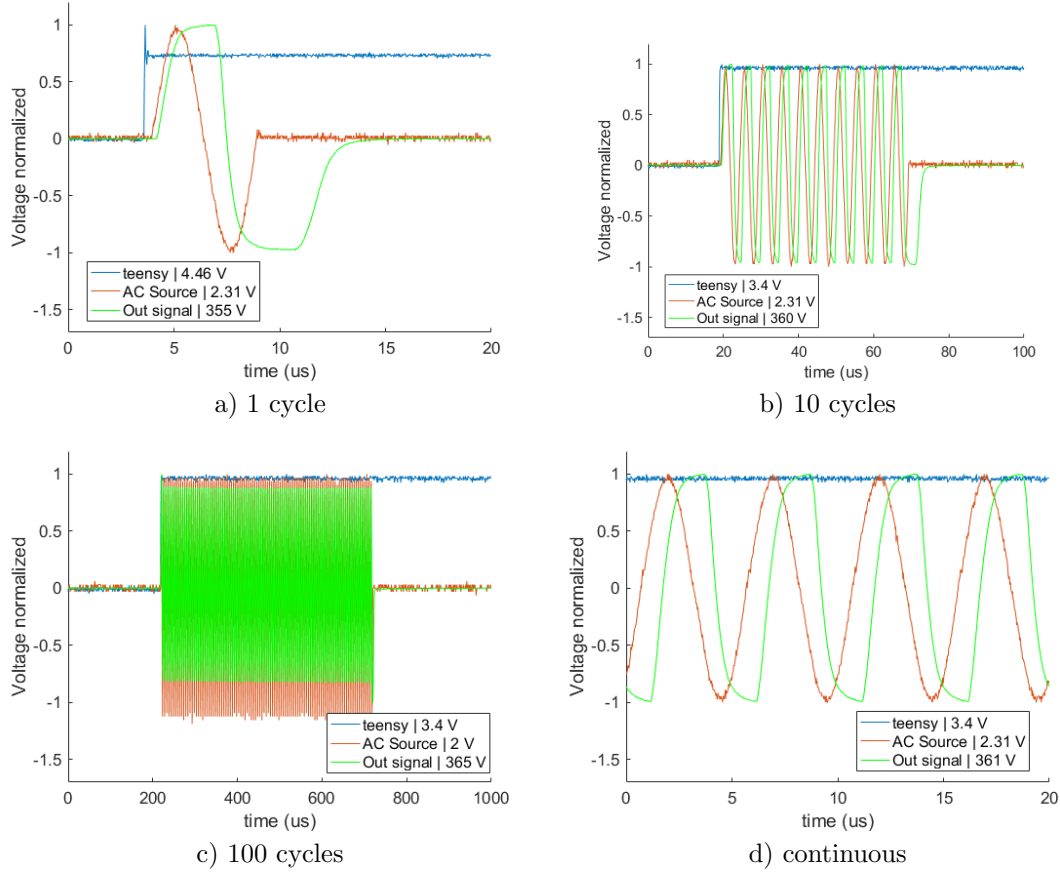
Figure 3.56: Delay study for different number of cycles in burst mode, for maximum voltage applied - a) to c). d) Continuous output signal. Normalized voltages.

The delay to turn on is one magnitude order below than the turning off delay. Table 3.4 summarizes the average for these delays.

Table 3.4: Average delays between teensy and High Voltage field on, and between AC source turned off and High Voltage field turn off.

Trigger to High Voltage signal	
On	Off
$620.70 \pm 4.60\ ns$	$6.39 \pm 0.20\ \mu s$

Delays do not change with voltage of output signal.

Table 3.5: Resume of delays for the different modules.

light - TIA	TIA - μcontr.	μcontr. - AC source*	μcontr. - High Volt. Signal	
			ON	OFF
$7.00 \pm 1.71\ ms$	$51.23 \pm 6.13\ \mu s$	$391.75 \pm 2.88\ ns$	$620.70 \pm 4.60\ ns$	$6.39 \pm 0.20\ \mu s$

Table 3.5 compares each module delay for often used conditions, 200 kHz and 3 V_{pp}. The amplification delay is very significant (ms range) and should be the first to be taken in consideration, followed by signal reading and setting the trigger ($\sim 50\ \mu s$). The order delays are at hundreds of ns range. The delay between microcontroller and Ac source is twice the Ac source to high voltage signal delay, but still in hundreds of ns range. the Turning of delay $\sim 6\ \mu s$ should be paid attention if droplets are really close to each other, potently causing the following droplets to also deflect.

3.4.3 Experiments with Integrated System

Sorting and detection were integrated. Was chosen to start from the better setup to understand the limitations. A microfluidic structure was aligned with the photosensor, the light beam with photosensor, electrodes filled with liquid metal. Chopper as light signal at low frequency (7 Hz), picometer as bias supply with 30 V. When the signal crosses above 0.7 V an 100 cycles with 695 V_{pp} 200 kHz burst is produced causing a voltage drop as shown in Figure 3.57-a). To understand what this drop was, manual trigger was setted and hight voltage was applied for 2 s and then turned off. Signal offsets almost -6 V (Figure 3.57-b)). Although triaxial cables were used to shield the signal from photoconductor till Pre-Amplifier (10^9 V/I gain), photoconductors it self, their tracks, wire bonding, pcb conectors were all exposed to the electrodes signal, which were right on top of the photosensor.
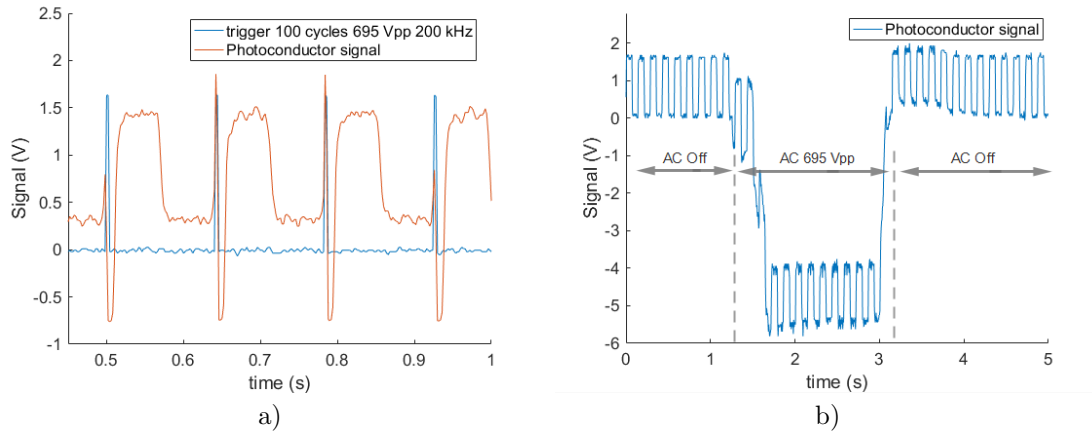
Figure 3.57: a) Photoconductor signal with time, microontroller aquires the signal and trigger when $V > V_{th}$ producing a 10 cycle burst with 695 Vpp 200 kHz. b) Distortion of Photoconductor signal when electrodes are actuated and return to normality when turned off.

To try to understand what was going on, both photoconductor's terminals were measured with and without applied field (Figures 3.58-a) and b)). At ground, noise jumped from few mV_{pp} to 220 mV_{pp}; and at the positive supply from 50 mV_{pp} to 250 mV_{pp}. The noise was confirmed to be from the electrodes by doing a frequency analysis, comparing electrodes switch on and off (Figures 3.58-b) and d). With them on appeared the frequency of actuation and it's harmonics.
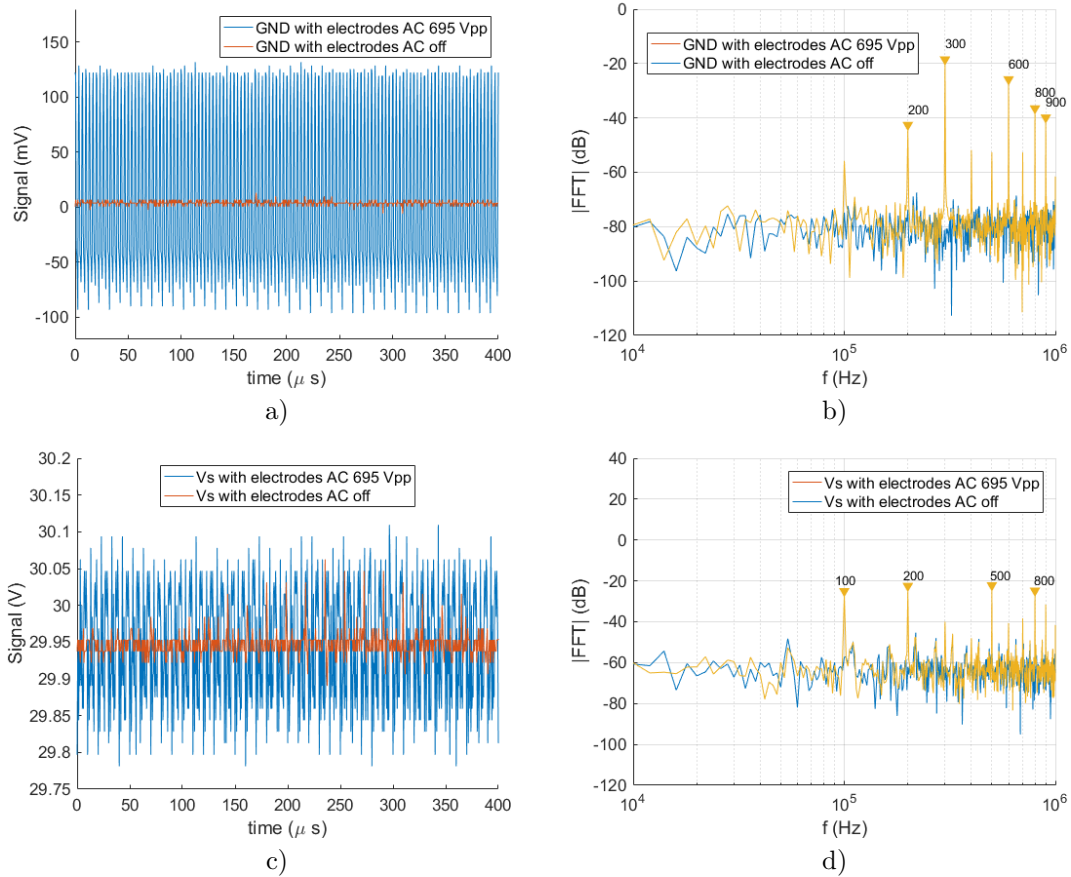
Figure 3.58: Distortion caused by electrodes actuation - 695 Vpp 200 kHz - on photoconductor terminals.

One should notice that 30 V bias created 1.5 V signal, and the summed noise amplitude is at most 0.5 V, which per si cannot cause a -6 V drop. This voltage drop corresponds to 6 nA of induced current, pointing that electromagnetic interference was occurring. In fact there is a closed common ground track all around photoconductor's substrate, which may work as a closed line for induction. Some more time was needed to understand and debug the system.

Chapter 4

Conclusion and Outlook

The aim for this dissertation was to conceive an integrated microfluidic system for droplet detection and deflection applied for Directed evolution, major steps were done in that direction. The work started by a state-of-art review for Droplet's microfluidic applied to Directed Evolution, identifying the system's core modules: droplet generation and encapsulation, detection and sorting. Soft lithography, metal deposition and etch among other techniques were learned enabling semi-autonomous device fabrication. Droplet generation was already studied, serving as a starting point for the core of this work: Sorting, Detection and Integration. The key achievements can be summarized:

- Flow-focusing droplet generator was used as a starting point for system development.

- A circuit to generate high voltage at different frequencies (50-700 V_{pp}, 1 Hz - 1MHz) was designed and built. It was indispensable to generate the necessaries AC voltages for actuation by DEP.

- Three different TiW planar electrodes, one 3D electrode and five microfluidic structures were simulated, fabricated and tested. Allowing multiple alignments between electrodes and bifurcations, giving valuable information about optimal gradient field magnitude, bifurcation geometry and channel height for droplet sorting. Default sorting by hydraulic resistance performed better than by momentum. Electrodes in contact with solution degrade faster and usable voltage range is more limited.

- Two completely novel 3D electrode/bifurcation geometries were designed, simulated and tested, achieving sorting without coalescence. One geometry performs better for higher flow rates, and requires less voltages; the other allows sorting without coalescence for droplets at low velocity and without space in between.

- Sorting by pneumatic actuation was implemented with success. Performance was evaluated in function of channel height, droplets radius and flow rate. Valve's actuation delay were also characterized, showing that response time of solenoid valves was the limitation factor.

- Image analysis script was developed to allow droplet counting and size measurement. Still requiring some characterization to proper validate and use the script "blindly".

- 50 μm side a-Si:H thin film photoconductors were used for droplet's optical detection by absorbance. They Offer the advantage of faster measurements (till at least 500 Hz, limited by the setup), customized to fit microfluidic channels and droplet dimensions.

- Preliminary study of light intensity variation with droplet dye's concentration was performed using 50 μm side a-Si:H thin film photoconductors.

- Transimpedance Amplifier circuit with 200 dB gain was designed and implemented to allow photoconductor's signal acquisition and processing on a portable platform.

- System integration with detection and electrical sorting was implemented. Delays between signal acquisition and electric actuation were characterized. Still needing some solution to avoid signal distortion caused by high voltage burst required for DEP actuation.

At this point each module is working. Still some work is left to be done, my future work suggestions are:

- Firstly remove the signal distortion caused by high voltage burst for DEP. This may influence the setup, or even the actuation method therefrom being the first problem to approach. Photoconductors tracks, wire bonding and PCB connector, weren't shielded. The use of optic fiber[82] to allow photosensor shielding from electrodes without having to put away the photoconductor from the light signal, may solve the problem. Acoustic sorting could be thought as an alternative to electrical sorting if incompatibility is confirmed -but i don't think that's the case.

- Droplet generator should be proper characterized with microscope and photosensor in parallel to evaluate droplet's size and frequency, also giving information about real droplet speed inside the channels, which will be helpful when designed photosensors's array.

- A customized setup should be developed to study sorting. Mainly to assure reproducibility, sometimes disturbed by outlets tubes's relative height variation. A box with several heights should be built to study the effect on passive deflection, and to guarantee always the same conditions.

- To perform detection and sorting integration, burst's duration and timming will play a key role. The study would benefit if some image acquisition is performed at same time, because gives information about droplet position when the actuation is occurring, and not just a binary response for sorting success, as the integration of another photosensor would give.

- High Voltage AC Circuit may be miniaturized using low power RF oscillators to generate the signal[83].

Bibliography

[1] Guilherme Araújo de Andrade. *Droplet Microfluidics Systems for Dyrected Evolution.* Instituto Superior Técnico, Master dissertation, 2017.

[2] Liu Packer, Michael S. and David R. Methods for the directed evolution of proteins. *Nature Reviews Genetics*, 16(379), 2015.

[3] Manish Kumar Tiwari, Ranjitha Singh, Raushan Kumar Singh, In-Won Kim, and Jung-Kul Lee. Computational approaches for rational design of proteins with novel functionalities. *Computational and Structural Biotechnology Journal*, 2(3):e201204002, 2012.

[4] Yu-Ping Lai, Jing Huang, Lin-Fa Wang, Jun Li, and Zi-Rong Wu. A new approach to random mutagenesis in vitro. *Biotechnology and Bioengineering*, 86(6):622–627, 2004.

[5] Keith M. Derbyshire, Joseph J. Salvo, and Nigel D.F. Grindley. A simple and efficient procedure for saturation mutagenesis using mixed oligodeoxynucleotides. *Gene*, 46(2):145 – 152, 1986.

[6] Ernst Freese. The specific mutagenic effect of base analogues on phage t4. *Journal of Molecular Biology*, 1(2):87 – 105, 1959.

[7] B.A. Bridges. Mutagenic dna repair in escherichia coli xvi. mutagenesis by ultraviolet light plus delayed photoreversal in reca strains. *Mutation Research/Fundamental and Molecular Mechanisms of Mutagenesis*, 198(2):343 – 350, 1988.

[8] Jeremy J. Agresti, Eugene Antipov, Adam R. Abate, Keunho Ahn, Amy C. Rowat, Jean-Christophe Baret, Manuel Marquez, Alexander M. Klibanov, Andrew D. Griffiths, and David A. Weitz. Ultrahigh-throughput screening in drop-based microfluidics for directed evolution. *Proceedings of the National Academy of Sciences*, 107(9):4004–4009, 2010.

[9] H. M. Shapiro. *Pratical Flow Cytometry.* Wiley-Liss, 2003.

[10] K. Dane Wittrup. Yeast surface display for screening combinatorial polypeptide libraries. *Nature Biotechnology*, 15, 1997.

[11] Amir Aharoni, Karena Thieme, Cecilia P. C. Chiu, Sabrina Buchini, Luke L. Lairson, Hongming Chen, Natalie C. J. Strynadka, Warren W. Wakarchuk, and Stephen G. Withers. High-throughput screening methodology for the directed evolution of glycosyltransferases. *Nature Methods*, 3:609 EP –, Jul 2006. Article.

[12] Pingan Zhu and Liqiu Wang. Passive and active droplet generation with microfluidics: a review. *Lab Chip*, 17:34–75, 2017.

[13] Shiguang Li, Zhiguang Xu, Aaron Mazzeo, Daniel Burns, Gang Fu, Matthew Dirckx, Vijay Shilpiekandula, Xing Chen, Nimai Nayak, Eehern Wong, Soon Fatt Yoon, and Zhong Fang. Review of production of microfluidic devices: Material, manufacturing and metrology. *Proceedings of SPIE - The International Society for Optical Engineering*, 6993, 04 2008.

[14] Front-matter. In Shaurya Prakash and Junghoon Yeom, editors, *Nanofluidics and Microfluidics.* William Andrew Publishing, 2014.

[15] John A. Rogers and Ralph G. Nuzzo. Recent progress in soft lithography. *Materials Today*, 8(2):50 – 56, 2005.

[16] Byeong-Ui Moon, Steven G. Jones, Dae Kun Hwang, and Scott S. H. Tsai. Microfluidic generation of aqueous two-phase system (atps) droplets by controlled pulsating inlet pressures. *Lab Chip*, 15:2437–2444, 2015.

[17] Yuehao Li, Mranal Jain, Yongting Ma, and Krishnaswamy Nandakumar. Control of the breakup process of viscous droplets by an external electric field inside a microfluidic device. *Soft Matter*, 11:3884–3899, 2015.

[18] David J. Collins, Adrian Neild, Andrew deMello, Ai-Qun Liu, and Ye Ai. The poisson distribution and beyond: methods for microfluidic droplet production and single cell encapsulation. *Lab Chip*, 15:3439–3459, 2015.

[19] Piotr Garstecki, Irina Gitlin, Willow DiLuzio, George M. Whitesides, Eugenia Kumacheva, and Howard A. Stone. Formation of monodisperse bubbles in a microfluidic flow-focusing device. *Applied Physics Letters*, 85(13):2649–2651, 2004.

[20] M. Belloul, J.-F. Bartolo, B. Ziraoui, F. Coldren, V. Taly, and A. I. El Abed. High-throughput formation and control of monodisperse liquid crystals droplets driven by an alternating current electric field in a microfluidic device. *Applied Physics Letters*, 103(3):033112, 2013.

[21] Cheng Li, Kappy Krueger, Weiwei Yang, Hongxu Duan, and Weiwei Deng. Gas-focused liquid microjets from a slit. *Physics of Fluids*, 27(3):032101, 2015.

[22] Chunmei Zhou, Pingan Zhu, Ye Tian, Xin Tang, Rui Shi, and Liqiu Wang. Microfluidic generation of aqueous two-phase-system (atps) droplets by oil-droplet choppers. *Lab Chip*, 17:3310–3317, 2017.

[23] Bo Zheng, Joshua D. Tice, and Rustem F. Ismagilov. Formation of droplets of alternating composition in microfluidic channels and applications to indexing of concentrations in droplet-based assays. *Anal Chem*, 76(17):4977–4982, Sep 2004.

[24] Lucas Frenz, Joshua Blouwolff, Andrew D. Griffiths, and Jean-Christophe Baret. Microfluidic production of droplet pairs. *Langmuir*, 24(20):12073–12076, 2008. PMID: 18823095.

[25] Rongcong Luo, Ngoc-Duy Dinh, and Chia-Hung Chen. Fast-responsive hydrogel as an injectable pump for rapid on-demand fluidic flow control. *Biomicrofluidics*, 11(3):034107, 2017.

[26] Minsoung Rhee, Peng Liu, Robert J. Meagher, Yooli K. Light, and Anup K. Singh. Versatile on-demand droplet generation for controlled encapsulation. *Biomicrofluidics*, 8(3):034112, May 2014.

[27] Yun Ding, Xavier Casadevall i Solvas, and Andrew deMello. "v-junction": a novel structure for high-speed generation of bespoke droplet flows. *Analyst*, 140:414–421, 2015.

[28] Uwe Tangen, Abhishek Sharma, Patrick Wagler, and John S. McCaskill. On demand nanoliter-scale microfluidic droplet generation, injection, and mixing using a passive microfluidic device. *Biomicrofluidics*, 9(1):014119, Jan 2015.

[29] A. S. Utada, L.-Y. Chu, A. Fernandez-Nieves, D. R. Link, C. Holtze, and D. A. Weitz. Dripping, jetting, drops, and wetting: The magic of microfluidics. *MRS Bulletin*, 32(9), 2007.

[30] P. B. Umbanhowar, V. Prasad, and D. A. Weitz. Monodisperse emulsion generation via drop break off in a coflowing stream. *Langmuir*, 16(2):347–351, 2000.

[31] Levent Yobas, Stefan Martens, Wee-Liat Ong, and Nagarajan Ranganathan. High-performance flow-focusing geometry for spontaneous generation of monodispersed droplets. *Lab Chip*, 6:1073–1079, 2006.

[32] A. S. Utada, E. Lorenceau, D. R. Link, P. D. Kaplan, H. A. Stone, and D. A. Weitz. Monodisperse double emulsions generated from a microcapillary device. 308(5721):537–541, 2005.

[33] Rémi Dangla, S. Cagri Kayi, and Charles N. Baroud. Droplet microfluidics driven by gradients of confinement. *Proc Natl Acad Sci U S A*, 110(3):853–858, Jan 2013.

[34] Karin Schroan, Montse Ferrando, Silvia de Lamo-Castellva?, Sami Sahin, and Carme Güell. Linking findings in microfluidics to membrane emulsification process design: The importance of wettability and component interactions with interfaces. *Membranes (Basel)*, 6(2):26, Jun 2016.

[35] Goran T. Vladisavljević, Nauman Khalid, Marcos A. Neves, Takashi Kuroiwa, Mitsutoshi Nakajima, Kunihiko Uemura, Sosaku Ichikawa, and Isao Kobayashi. Industrial lab-on-a-chip: Design, applications and scale-up for drug discovery and delivery. *Advanced Drug Delivery Reviews*, 65(11):1626 – 1663, 2013. Design production and characterization of drug delivery systems by Lab-on-a-Chip technology.

[36] Isao Kobayashi, Yoshihiro Wada, Kunihiko Uemura, and Mitsutoshi Nakajima. Microchannel emulsification for mass production of uniform fine droplets: integration of microchannel arrays on a chip. *Microfluidics and Nanofluidics*, 8(2):255–262, Feb 2010.

[37] Emma Piacentini, Lidietta Giorno, Marijana M. Dragosavac, Goran T. Vladisavljević, and Richard G. Holdich. Microencapsulation of oil droplets using cold water fish gelatine/gum arabic complex coacervation by membrane emulsification. *Food Research International*, 53(1):362 – 372, 2013.

[38] Thomas Ward, Magalie Faivre, Manouk Abkarian, and Howard A. Stone. Microfluidic flow focusing: Drop size and scaling in pressure versus flow-rate-driven pumping. *ELECTROPHORESIS*, 26(19):3716–3724, 2005.

[39] Andrew S. Utada, Alberto Fernandez-Nieves, Howard A. Stone, and David A. Weitz. Dripping to jetting transitions in coflowing liquid streams. *Phys. Rev. Lett.*, 99:094502, Aug 2007.

[40] A.G. Maran, F. Campo-Cortãos, and J.M. Gordillo. Generation of micron-sized drops and bubbles through viscous coflows. *Colloids and Surfaces A: Physicochemical and Engineering Aspects*, 344(1):2 – 7, 2009. Current research on foams.

[41] Florent Malloggi, Siva A Vanapalli, Hao Gu, Dirk van den Ende, and Frieder Mugele. Electrowetting-controlled droplet generation in a microfluidic flow-focusing device. *Journal of Physics: Condensed Matter*, 19(46):462101, 2007.

[42] Stefan Haeberle, Roland Zengerle, and Jens Ducrée. Centrifugal generation and manipulation of droplet emulsions. *Microfluidics and Nanofluidics*, 3(1):65–75, Feb 2007.

[43] Ting-Hsiang Wu, Yue Chen, Sung-Yong Park, Jason Hong, Tara Teslaa, Jiang F. Zhong, Dino Di Carlo, Michael A. Teitell, and Pei-Yu Chiou. Pulsed laser triggered high speed microfluidic fluorescence activated cell sorter(). *Lab Chip*, 12(7):1378–1383, Apr 2012. 22361780[pmid].

[44] Hui-Sung Moon, Kwanghwi Je, Jae-Woong Min, Donghyun Park, Kyung-Yeon Han, Seung-Ho Shin, Woong-Yang Park, Chang Eun Yoo, and Shin-Hyun Kim. Inertial-ordering-assisted droplet microfluidics for high-throughput single-cell rna-sequencing. *Lab Chip*, 18:775–784, 2018.

[45] Heng-Dong Xi, Hao Zheng, Wei Guo, Alfonso M. Ganan-Calvo, Ye Ai, Chia-Wen Tsao, Jun Zhou, Weihua Li, Yanyi Huang, Nam-Trung Nguyen, and Say Hwa Tan. Active droplet sorting in microfluidics: a review. *Lab Chip*, 17:751–771, 2017.

[46] Muhsincan Sesen, Tuncay Alan, and Adrian Neild. Microfluidic plug steering using surface acoustic waves. *Lab Chip*, 15:3030–3038, 2015.

[47] Darren R. Link, Erwan Grasland-Mongrain, Agnes Duri, Flavie Sarrazin, Zhengdong Cheng, Galder Cristobal, Manuel Marquez, and David A. Weitz. Electric control of droplets in microfluidic devices. *Angewandte Chemie International Edition*, 45(16):2556–2560, 2006.

[48] Byungwook Ahn, Kangsun Lee, Romain Louge, and Kwang W. Oh. Concurrent droplet charging and sorting by electrostatic actuation. *Biomicrofluidics*, 3(4):044102, Dec 2009. 002904BMF[PII].

[49] Hun Lee, Linfeng Xu, and Kwang W. Oh. Droplet-based microfluidic washing module for magnetic particle-based assays. *Biomicrofluidics*, 8(4):044113, Jul 2014. 1.4892495[PII].

[50] Sixing Li, Xiaoyun Ding, Feng Guo, Yuchao Chen, Michael Ian Lapsley, Sz-Chin Steven Lin, Lin Wang, J. Philip McCoy, Craig E. Cameron, and Tony Jun Huang. An on-chip, multichannel droplet sorter using standing surface acoustic waves (ssaw). *Anal Chem*, 85(11):5468–5474, Jun 2013. 23647057[pmid].

[51] Lang Rao, Bo Cai, Xiao-Lei Yu, Shi-Shang Guo, Wei Liu, and Xing-Zhong Zhao. One-step fabrication of 3d silver paste electrodes into microfluidic devices for enhanced droplet-based cell sorting. *AIP Advances*, 5(5):057134, 2015.

[52] Cheng Qian, Haibo Huang, Liguo Chen, Xiangpeng Li, Zunbiao Ge, Tao Chen, Zhan Yang, and Lining Sun. Dielectrophoresis for bioparticle manipulation. *International Journal of Molecular Sciences*, 15(10):18281–18309, Oct 2014.

[53] Jingmei Li, Zhou Liu, Haibo Huang, and Ho Cheung Shum. Shielding electric fields to prevent coalescence of emulsions in microfluidic channels using a 3d metallic coil. *Micromachines*, 6(10):1459–1468, 2015.

[54] Jeremy J. Agresti, Eugene Antipov, Adam R. Abate, Keunho Ahn, Amy C. Rowat, Jean-Christophe Baret, Manuel Marquez, Alexander M. Klibanov, Andrew D. Griffiths, and David A. Weitz. Ultrahigh-throughput screening in drop-based microfluidics for directed evolution. *Proceedings of the National Academy of Sciences*, 107(9):4004–4009, 2010.

[55] Adam Sciambi and Adam R. Abate. Generating electric fields in pdms microfluidic devices with salt water electrodes. *Lab Chip*, 14:2605–2609, 2014.

[56] Adam Sciambi and Adam R. Abate. Accurate microfluidic sorting of droplets at 30 khz. *Lab Chip*, 15:47–51, 2015.

[57] Iain C. Clark and Adam R. Abate. Finding a helix in a haystack: nucleic acid cytometry with droplet microfluidics. *Lab Chip*, 17:2032–2045, 2017.

[58] Liang Wu, Pu Chen, Yingsong Dong, Xiaojun Feng, and Bi-Feng Liu. Encapsulation of single cells on a microfluidic device integrating droplet generation with fluorescence-activated droplet sorting. *Biomedical Microdevices*, 15(3):553–560, Jun.

[59] Zhenning Cao, Fangyuan Chen, Ning Bao, Huacheng He, Peisheng Xu, Saikat Jana, Sunghwan Jung, Hongzhen Lian, and Chang Lu. Droplet sorting based on the number of encapsulated particles using a solenoid valve. *Lab Chip*, 13:171–178, 2013.

[60] A. R. Abate and D. A. Weitz. Single-layer membrane valves for elastomeric microfluidic devices. *Applied Physics Letters*, 92(24):243509, 2008.

[61] Dong Hyun Yoon, Junichi Ito, Tetsushi Sekiguchi, and Shuichi Shoji. Active and precise control of microdroplet division using horizontal pneumatic valves in bifurcating microchannel. 4:197–205, 06 2013.

[62] Adam R. Abate, Jeremy J. Agresti, and David A. Weitz. Microfluidic sorting with high-speed single-layer membrane valves. *Applied Physics Letters*, 96(20):203509, 2010.

[63] Ying Zhu and Qun Fang. Analytical detection techniques for droplet microfluidics "a review. *Analytica Chimica Acta*, 787:24 – 35, 2013.

[64] D. R. Santos, R. R. G. Soares, V. Chu, and J. P. Conde. Performance of hydrogenated amorphous silicon thin film photosensors at ultra-low light levels: Towards attomole sensitivities in lab-on-chip biosensing applications. *IEEE Sensors Journal*, 17(21):6895–6903, Nov 2017.

[65] Gallium–indium eutectic description. https://www.sigmaaldrich.com/catalog/product/aldrich/495425?lang=pt&region=PT. Accessed: 2018-10-22.

[66] João Tiago dos Santos Fernandes. *Microfluidic cell culture platforms for the study of the molecular mechanisms of Parkinson's disease*. Instituto Superior Técnico, 2015.

[67] Dmitry A. Markov, Elizabeth M. Lillie, Shawn P. Garbett, and Lisa J. McCawley. Variation in diffusion of gases through pdms due to plasma surface treatment and storage conditions. *Biomed Microdevices*, 16(1):91–96, Feb 2014. 24065585[pmid].

[68] Denis Roda dos Santos. *Integrated biosensors for Lab-on-a-Chip platforms*. PhD thesis, Instituto Superior Técnico, 2018.

[69] Yung-Chieh Tan, Jeffrey S. Fisher, Alan I. Lee, Vittorio Cristini, and Abraham Phillip Lee. Design of microfluidic channel geometries for the control of droplet volume, chemical concentration, and sorting. *Lab Chip*, 4:292–298, 2004.

[70] Wolfram Research, Inc. Mathematica, Version 11.3. Champaign, IL, 2018.

[71] Ronald R. Pethig. *Dielectrophoresis: Theory, Methodology and Biological Applications*. Wiley, 2017.

[72] 3M^{TM}Novec^{TM}. *3M^{TM}Novec^{TM}7500 Engineered Fluid: Procut Information*.

[73] Keunho Ahn, Charles Kerbage, Tom P. Hunt, R Westervelt, Darren Link, and DA Weitz. Dielectrophoretic manipulation of drops for high-speed microfluidic sorting devices. 88:024104–024104, 01 2006.

[74] Peter R. C. Gascoyne and Jody Vykoukal. Particle separation by dielectrophoresis. *Electrophoresis*, 23(13):1973–1983, Jul 2002. 12210248[pmid].

[75] Linas Mazutis, John Gilbert, W. Lloyd Ung, David A. Weitz, Andrew D. Griffiths, and John A. Heyman. Single-cell analysis and sorting using droplet-based microfluidics. *Nat Protoc*, 8(5):870–891, May 2013. 23558786[pmid].

[76] Charles N. Baroud, Francois Gallaire, and Raomi Dangla. Dynamics of microfluidic droplets. *Lab Chip*, 10:2032–2045, 2010.

[77] Michael J. Fuerstman, Ann Lai, Meghan E. Thurlow, Sergey S. Shevkoplyas, Howard A. Stone, and George M. Whitesides. The pressure drop along rectangular microchannels containing bubbles. *Lab Chip*, 7:1479–1489, 2007.

[78] Hamed Amini, Wonhee Lee, and Dino Di Carlo. Inertial microfluidic physics. *Lab Chip*, 14:2739–2761, 2014.

[79] Matas, Jp., Morris, Jf., and Guazzelli, E. Lateral forces on a sphere. *Oil & Gas Science and Technology - Rev. IFP*, 59(1):59–70, 2004.

[80] Bruce Carter. *Op Amps for Everyone, Fourth Edition*. Newnes, Newton, MA, USA, 4th edition, 2013.

[81] Akshay Bhat. Stabilize your transimpedance amplifier. 2012.

[82] N. . Nguyen, S. Lassemono, and F. A. Chollet. Optical detection for droplet size control in microfluidic droplet-based analysis systems. In *The 13th International Conference on Solid-State Sensors, Actuators and Microsystems, 2005. Digest of Technical Papers. TRANSDUCERS '05.*, volume 2, pages 1557–1560 Vol. 2, June 2005.

[83] Y.-Y. Jau, F. M. Benito, H. Partner, and P. D. D. Schwindt. Low power high-performance radio frequency oscillator for driving ion traps. *Review of Scientific Instruments*, 82(2):023118, 2011.

Appendix A

Microfluidic Structure's Masks

A.1 Overall View of First Microfluidic Mask
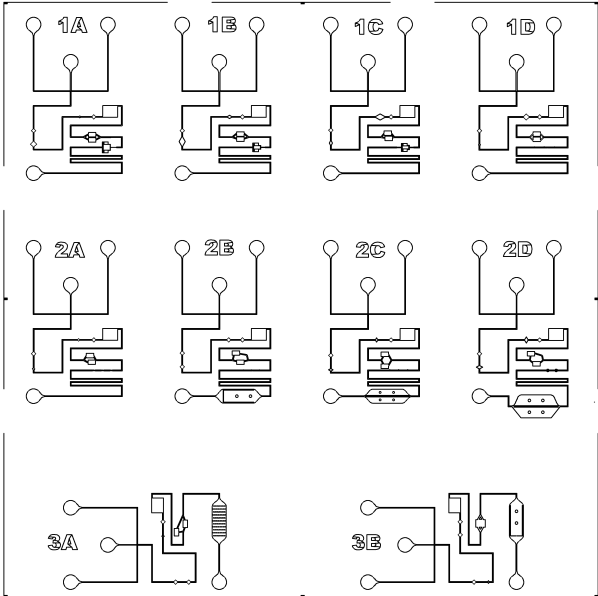
Figure A.1: First AutoCAD mask for droplet generation and manipulation. Inside a 4 cm side frame.

A.2 Overall View of Second Microfluidic Mask
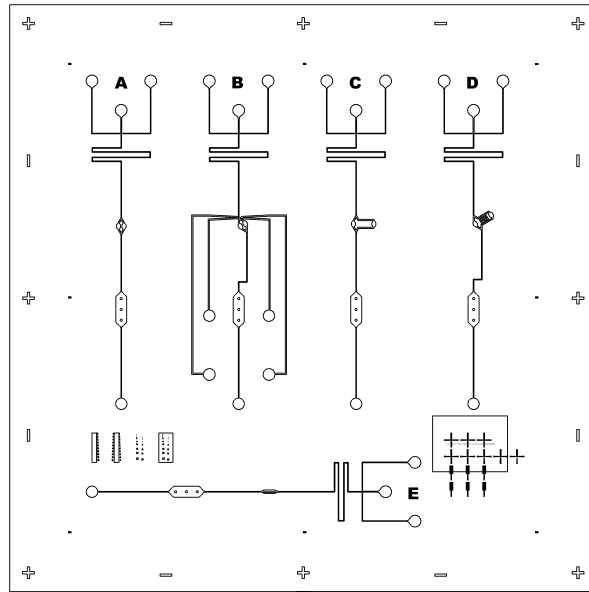
Figure A.2: Second AutoCAD mask for droplet generation and manipulation. Inside a 4 cm side frame.
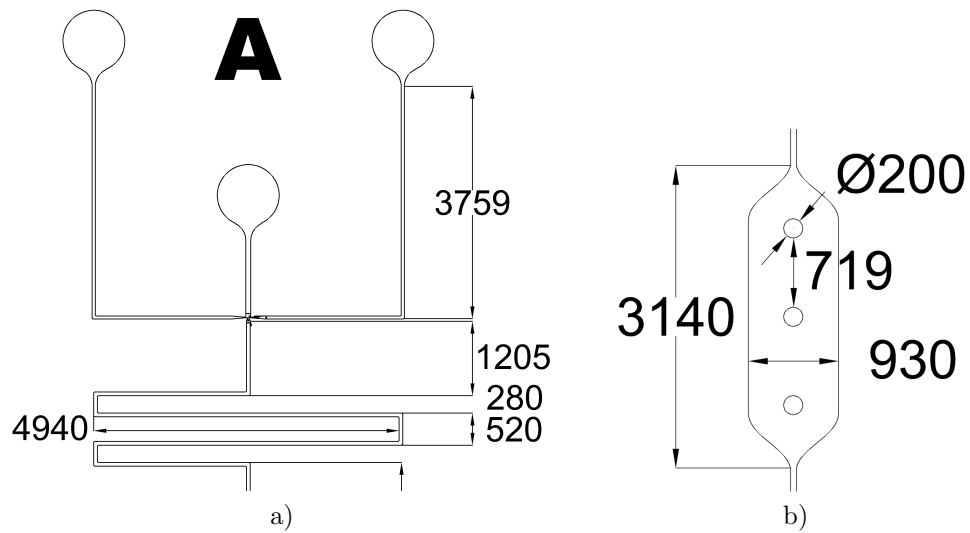
Figure A.3: a)Close-up at inlet region. b) reservoir dimensions. All dimensions in microns.
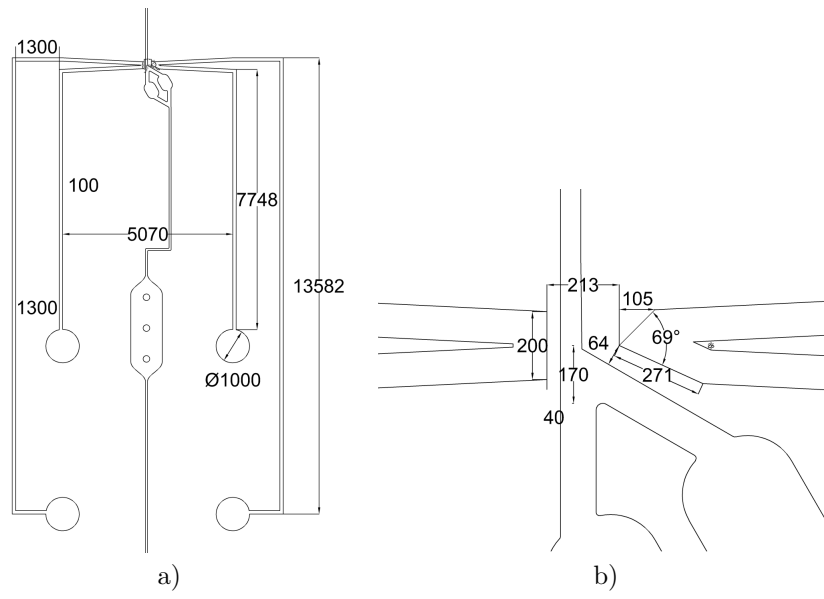
Figure A.4: a)Liquid electrodes geometry. b) close up at electrode's tip. All dimensions in microns.

Appendix B

Pneumatic Sorting

B.1   Supplementary Images
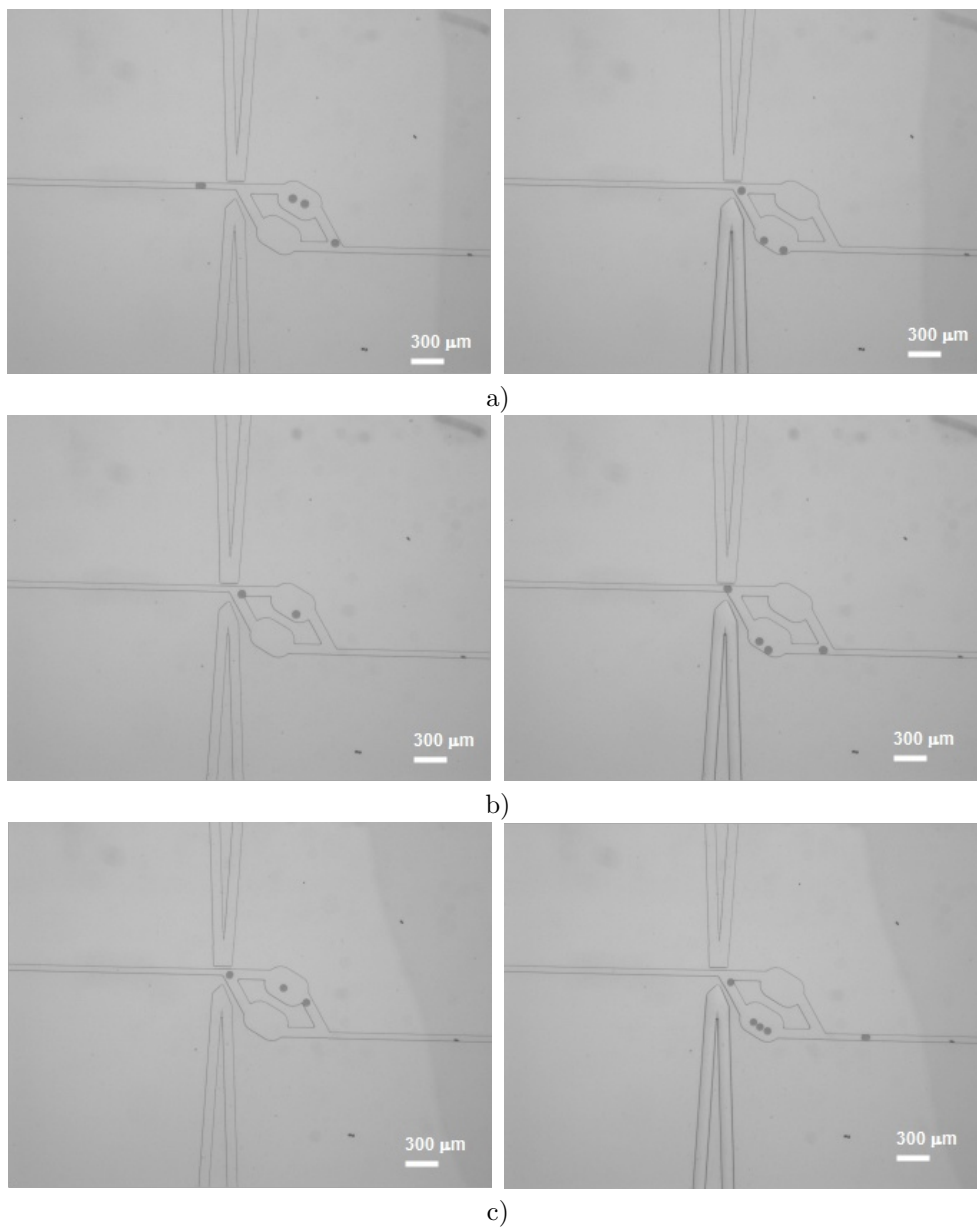
Figure B.1: Microscope images of pneumatic sorting for different flow rates. Left images show passive sorting, and the ones on the right show bottom valve actuation. a) $\phi_d = 0.06\ \mu l/min$; $\phi_c = 3.00\ \mu l/min$; b) $\phi_d = 0.07\ \mu l/min$; $\phi_c = 4.00\ \mu l/min$; c) $\phi_d = 0.17\ \mu l/min$; $\phi_c = 9.20\ \mu l/min$. Channel height: $40\ \mu m$. Valve pressure: 0.36 MPa.

B.2 Script for Droplet Counting

The script uses a Circular Hough Transform based algorithm to find circles in droplet's microscope images, by imfindcircles Matlab's function. VirtualDub Software was used to create image sequence from 120 fps microscope screen recording (with CamStudio Software). To calculate the real droplet's radius, r, inside microfluidic channels of h height from the radius inferred by the image, a, Equation B.1 was used. Obtained matching spheroid volume to sphere volume. Figure B.2 shows the analysis of frame, showing droplet recognition with blue circles, and false positives (yellow circles), with the two counting regions (blue and green rectangles), an histogram is updated showing radius distribution for each chamber, a table with average radius and a plot showing the sorting rate with time for each chamber.

$$r = \begin{cases} \sqrt[3]{\frac{a^2 h}{2}}, & a > h \\ r, & \text{otherwise} \end{cases} \tag{B.1}$$
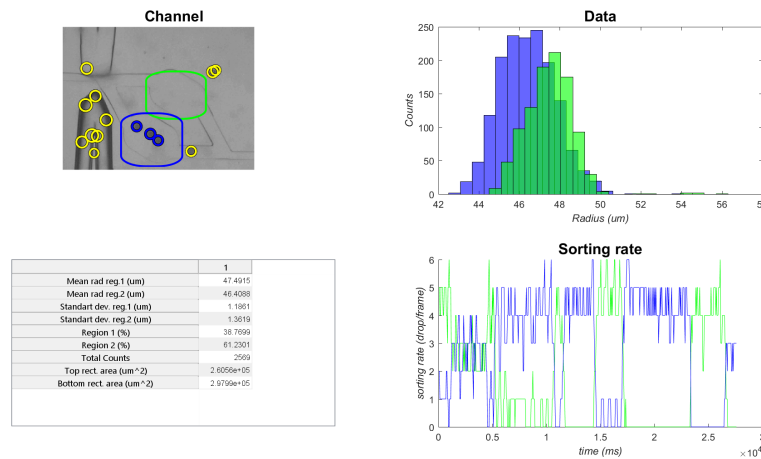
Figure B.2: Frame of image analysis.

It was guarantee that the same frame was not multiple times evaluated, and that at each frame all droplets were different. Radius were also confirmed by Imagej Software by area and diameter measurements as described by Guilherme Andrade[1]. To "blindly" apply the script, a validation study should first be performed. It wasn't done beacause results were in good agreements and time was scarce.

```
1  clearvars −global ___
2  clearvars time contagem1 contagem2
3
4  %**********************PARAMETERS TO USER EDIT
         ********************************
5  %filename to analise
6  name = '0p17_9p2';
7  framerate = 120;      %screen recording
8  firstframe = 36;      %first frame to analyse
9  lastframe = 6893;     %last frame to analyse
10 jump = 8;             %number of frames to jump in each analysis, avoids
         repeated droplet counting
11 tempopausa = 0.05;    %pause for visualization
12 altura = 40;          %channel height
13 escala = 1068/60;     %micron per pixel
14 %
         ***********************************************************************************
15 %**********************ANIMATION − OPTIONAL*******************
16 % writerObj = VideoWriter(sprintf('VideoResult_%s.avi',name));
17 % writerObj.FrameRate = 30;
```

```matlab
18   % open(writerObj);
19   %**********************END Animation**************************
20
21   %**** Adjustable parameters for droplet recognition ***
22   sensibilidade = 0.985; % More sensitivity catches more
23   thresholdborda = 0.43;% More treshold, will require more image contrast to
         detect
24   rmin=1;%minimum radius to detect in pixels
25   rmax=7;% minimum radius to detect in pixels
26   %Rectangles's Position
27   shifth = 24;
28   shiftv =-9;
29   % Bottom
30   x1=142+shifth;
31   y1=135+shiftv;
32   w1=27;
33   h1=28;
34   %Top
35   x2=158+shifth;
36   y2=109+shiftv;
37   w2=27;
38   h2=27;
39
40   reg1=[];
41   reg2=[];
42   f=figure;
43   t=uitable(f);
44   frame=0;
45
46   number = firstframe;
47   while number < (lastframe-jump) %loop for the frame range chosen
48
49       frame = frame + 1; %number of analysed frames
50       number = number + jump %number of the absolute frame in analysis
51
52
53
54       %gets frame and shows  it
55       rgb =  imread(sprintf('%s_%04d.png',name,number));
56       subplot(2,2,1);
57       hold on
58       title('Channel','FontWeight','bold','fontsize',16);
59       imshow(rgb)
60       xlim([130 245])
61       ylim([90 160])
62       pause(tempopausa);
63
64       %converts frame to gray scale, shows and analyses
65       gray_image = rgb2gray(rgb);
66       imshow(gray_image)
67       [centers,radii] = imfindcircles(rgb,[rmin rmax],'ObjectPolarity','dark'
             , ...
68       'Sensitivity',sensibilidade,'EdgeThreshold',thresholdborda)
69       h = viscircles(centers,radii,'Color','y');
70       hold on;
71
72
73       %Shows the rectangles where droplets are being counted.
```

```matlab
74          rectangle('Position',[x1,y1,w1,h1],...
75          'Curvature',[0.8,0.4],...
76          'LineWidth',2,'LineStyle','-','EdgeColor', 'g');
77          hold on;
78          rectangle('Position',[x2,y2,w2,h2],...
79          'Curvature',[0.8,0.4],...
80          'LineWidth',2,'LineStyle','-','EdgeColor', 'b');
81
82          x1max=x1+w1;
83          y1max=y1+h1;
84          x2max=x2+w2;
85          y2max=y2+h2;
86          centro1=[];
87          raio1=[];
88          centro2=[];
89          raio2=[];
90
91          %***************Conditions to detect online inside the rectangles****
92          for n=1: size(centers,1)
93              %Top Region
94              if (centers(n,1)>x1) && ( (centers(n,1)) < x1max) && (centers(n,2)
                    >y1) && (centers(n,2) < y1max)
95                  %saves center and radius
96                  centro1 = cat(1, centro1, centers(n,:));
97                  raio1 = cat(1, raio1, radii(n));
98              end
99              %Bottom Region
100             if (centers(n,1)>x2) && (centers(n,1) < x2max) && (centers(n,2)>y2
                    ) && (centers(n,2) < y2max)
101                 %saves center and radius
102                 centro2 = cat(1, centro2, centers(n,:));
103                 raio2 = cat(1, raio2, radii(n));
104             end
105         end
106
107         % Shows the detected droplets
108         viscircles(centro1,raio1,'Color','g')
109         viscircles(centro2,raio2,'Color','b')
110         pause(tempopausa);
111
112         %If diameters are bigger than height should be corrected by spheroid
113         %analysis
114         %First recatngle
115         for i = 1:size(raio1,1)
116             %diameter smaller than channel height
117             if 2*raio1(i)<= altura
118                 reg1 = cat(1,reg1, [centro1(i,:)  raio1(i)*escala]);
119             end
120             %diameter bigger than channel height
121             if 2*raio1(i)>= altura
122                 reg1 = cat(1,reg1, [centro1(i,:)  nthroot((raio1(i)*escala)*(
                        raio1(i)*escala)*altura/2, 3)]);
123             end
124         end
125         %Second rectangle
126         for i = 1:size(raio2,1)
127             %diametro menor que altura
128             if 2*raio2(i)<= altura
```

```matlab
129              reg2 = cat(1,reg2, [centro2(i,:)  raio2(i)*escala]);
130          end
131          if 2*raio2(i)>= altura
132              reg2 = cat(1,reg2, [centro2(i,:)  nthroot((raio2(i)*escala)*(
                     raio2(i)*escala)*altura/2, 3)]);
133          end
134      end
135
136
137      %************************** PLOTS SETTINGS **********************
138      %*********** Conditions to create table without data *************
139      if (isempty(reg1) && ~isempty(reg2))%Region one without counting
140          nnames = {'Mean rad reg.1 (um)','Mean rad reg.2 (um)', 'Standart
                 dev. reg.1 (um)','Standart dev. reg.2 (um)', 'Region 1 (%)','
                 Region 2 (%)',...
141          'Total Counts','Mean rad (um)', 'Standart dev (um)',...
142          'Top rect. area (um^2)','Bottom rect. area (um^2)',sprintf('Frame
                 number (over %d):',lastframe)};
143          d = [0 ; mean(reg2(:,3)); 0; std(reg2(:,3));...
144          0; 0;size(reg2,1);  mean(reg2(:,3)); std(reg2(:,3));...
145          w1*h1*escala*escala; w2*h2*escala*escala; number]
146      elseif (isempty(reg2) && ~isempty(reg1))%Region two without counting
147          nnames = {'Mean rad reg.1 (um)','Mean rad reg.2 (um)', 'Standart
                 dev. reg.1 (um)','Standart dev. reg.2 (um)', 'Region 1 (%)','
                 Region 2 (%)',...
148          'Total Counts','Mean rad (um)', 'Standart dev (um)',...
149          'Top rect. area (um^2)','Bottom rect. area (um^2)',sprintf('Frame
                 number (over %d):',lastframe)};
150          d = [mean(reg1(:,3)) ; 0; std(reg1(:,3)); 0;...
151          size(reg1,1)*100/(size(reg1,1)+size(reg2,1));  0;...
152          size(reg1,1)+size(reg2,1);  mean(reg1(:,3)); std(reg1(:,3));...
153          w1*h1*escala*escala; w2*h2*escala*escala; number]
154      elseif not(isempty(reg1))&& not(isempty(reg2)) %Both regions with
             counting
155          nnames = {'Mean rad reg.1 (um)','Mean rad reg.2 (um)', 'Standart
                 dev. reg.1 (um)','Standart dev. reg.2 (um)', 'Region 1 (%)','
                 Region 2 (%)',...
156          'Total Counts','Mean rad (um)', 'Standart dev (um)',...
157          'Top rect. area (um^2)','Bottom rect. area (um^2)',sprintf('Frame
                 number (over %d):',lastframe)};
158          d = [mean(reg1(:,3)) ; mean(reg2(:,3)); std(reg1(:,3)); std(reg2
                 (:,3));...
159          size(reg1,1)*100/(size(reg1,1)+size(reg2,1));...
160          size(reg2,1)*100/(size(reg1,1)+size(reg2,1));...
161          size(reg1,1)+size(reg2,1); mean(cat(1,reg1(:,3),reg2(:,3))); std(
                 cat(1,reg1(:,3),reg2(:,3)));...
162          w1*h1*escala*escala; w2*h2*escala*escala; number]
163      end
164      % *******************************************************
165      t.Data= d;
166      t.RowName = nnames;
167
168      %Plot droplet radius: histogram
169      delete(subplot(2,2,2))
170      subplot(2,2,2);
171      if not(isempty(reg2))
172          histogram(reg2(:,3),20,'FaceColor','b')
173      end
```

```matlab
174         hold on
175         if not(isempty(reg1))
176             histogram(reg1(:,3),20,'FaceColor','g')
177         end
178         title('Droplet Size','FontWeight','bold','fontsize',16);
179         xlabel('Radius (um)','FontAngle','italic');
180         ylabel('Counts','FontAngle','italic');
181         hold off
182
183         %shows the table
184         subplot(2,2,3);
185         hold on
186         pos = get(subplot(2,2,3),'position');
187         delete(subplot(2,2,3))
188         set(t,'units','normalized')
189         set(t,'position',pos)
190         title('Data','FontWeight','bold','fontsize',16);
191         hold off
192
193         time(frame) = frame*jump/framerate; % in seconds
194         contagem1(frame) = size(raio1,1);
195         contagem2(frame) = size(raio2,1);
196
197
198         %Plot sorting rate with time in plot
199         delete(subplot(2,2,4));
200         subplot(2,2,4);
201         hold on
202         title('Sorting rate','FontWeight','bold','fontsize',16);
203         xlabel('time (s)','FontAngle','italic');
204         ylabel('sorting rate (drop/frame)','FontAngle','italic');
205         plot(time, contagem1,'g',time, contagem2,'b')
206         hold off
207
208
209         % %****************** Save each analysis frame *************
210         if frame > 3   %first three have different sizes and aren't used
211             % filename = sprintf('Results%04d.png', n);
212             thisimage = f;%imread(filename);
213             writeVideo(writerObj, thisimage);
214         end
215         saveas(f,sprintf('Results_%s_%04d.png',name,frame))
216 end
217 %*********************END***************************
218 saveas(f,sprintf('Results_final.png',name))% save the final analysis
219 % close(writerObj);
220
221 %*************Save data into txt file ***********
222 fileID = fopen(sprintf('Results_%s.txt',name),'w');
223 fprintf(fileID,'Radius (reg1) (um)  | Radius (reg2) (um)\n');
224 fprintf(fileID,'%02f  %02f \n',reg1(:,3), reg2(:,3));
225 fclose(fileID);
226
227 %*** Create an ANIMATION with the analysis frames ***
228
229 writerObj = VideoWriter('YourAVI.avi');
230 writerObj.FrameRate = 30;
231 open(writerObj);
```

```matlab
232
233  for n = firstframe+2 : lastframe
234  % filename = sprintf('Results%04d.png', n);
235  % thisimage = imread(filename);
236  % writeVideo(writerObj, thisimage);
237  % n
238  end
239  close(writerObj);
```

Appendix C

Dielectrophoresis Sorting

C.1   Bill of Materials for HVAC

Resistors

$R_{1,2}$ 3.3 kΩ 50 W 5 %

R_8 50 Ω 5 %

R_9 100 Ω 5 %

R_{10} 10 Ω 5 %

R_{11} 100 Ω 5 %

R_{12} 2*620 Ω 5 %

R_{14} 10 Ω 5 %

R_{15} 10 Ω 5 %

R_{16} 2*620 Ω 5 %

There is an extra 100 Ω 5 % resistor from AC Source to ground

Capacitors

C_1 10 μF

C_2 1 pF

C_3 1 pF

C_4 1 pF

C_5 10 μF

C_6 10 μF 400 V

C_7 1 pF

Integrated Components

Op-Amp (×2) THS4631DR3

BJT NPN FJAFS1510A

External Sources

AC Source Agilent 33220A

VDD Source hp 6209B 0-320 V 0-0.1 A

Positive Op-Amp Supply hp E3612 60 V 0.5 A

Negative Op-Amp Supply hp E3612 60 V 0.5 A

C.2 COMSOL Simulations

Simulations were made in COMSOL Software 5.2 performing a stationary study using Electrostatics(es) module[1]. For electrodes infinite relative permittivity was setted ($\epsilon_r = 10^6$). And was not taking in consideration PDMS walls, it was consider all as oil with ($\epsilon_r = 5.8$). The fields obtained are over estimated, because PDMS as lower permittivity than oil ($\epsilon_r \sim 3$).

C.3 Mechanical Sealing

Figure C.1-a) shows the mechanical sealing of PDMS structures against glass. Two PMMA plates with 2 mm were milled to create space for screws and for microfluidic connections, and by screwing sealing was created with success. No screw torque was characterized, but was taken attention not bend to much the plates. Figure C.1-b) shows the channel electrode alignment.

a)   b)
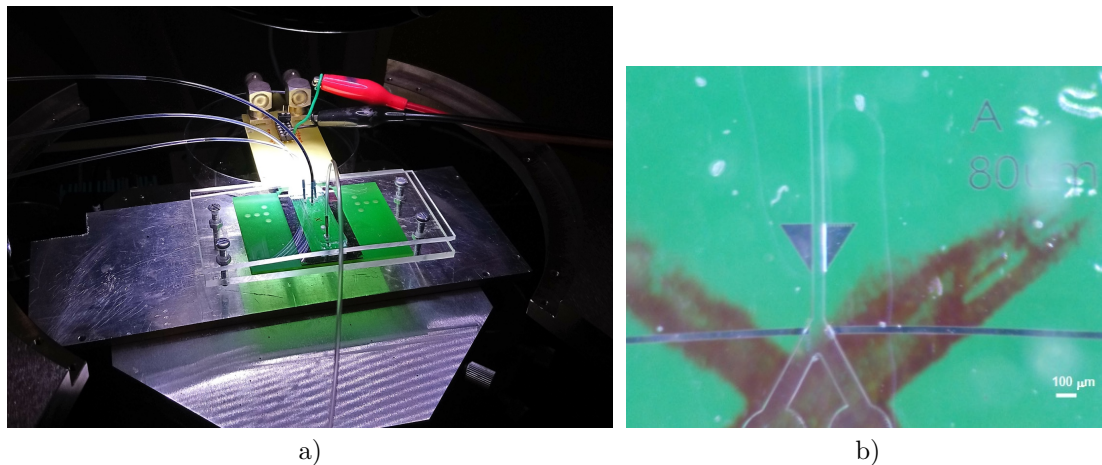
Figure C.1: a) PDMS structures mechanically sealed against electrodes on glass substrate. b) Electrodes and channel alignment.

C.4 Electrolysis and electrode dissolution

Electrolysis appeared when electrodes were in contact with fluids, even for oil. Figure C.2-b) shows air bubble formation when applied 583 V_{pp} 400 kHz. If aquous solution enters in contact with electrodes, they dissolve, as shown in Figure C.2-a).

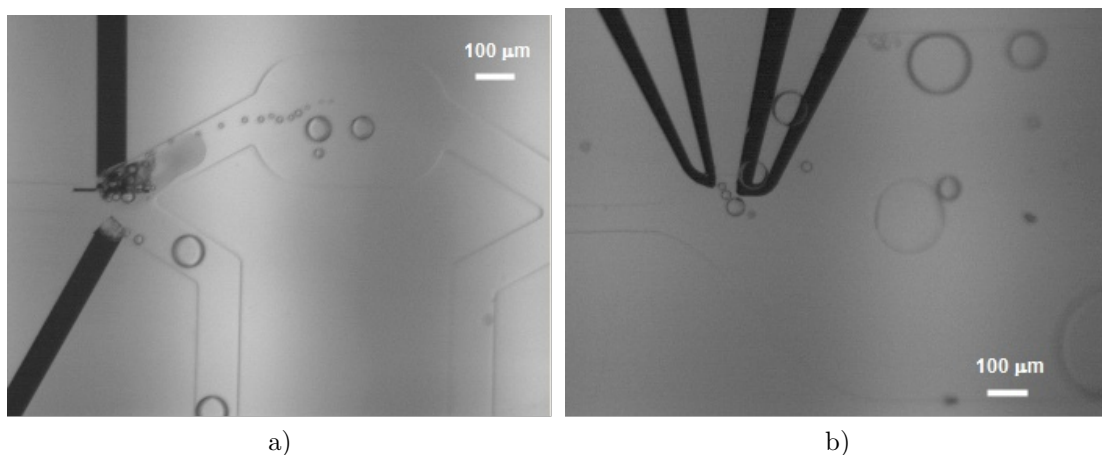a)   b)

Figure C.2: a) Movie frame of TiW electrode dissolving in 2 seconds when applied 656 V_{pp} 300 kHz. b) Electrolysis on oil (hfe 7500) when applied 583 V_{PP} at 400 kHz.

---

[1]For rigorous simulations they shoud be performed in AC, because the aim was to understand gradient variation with the geometry, simulation in DC simplified the simulations without major loss of information.

C.5 Electrodes Masks
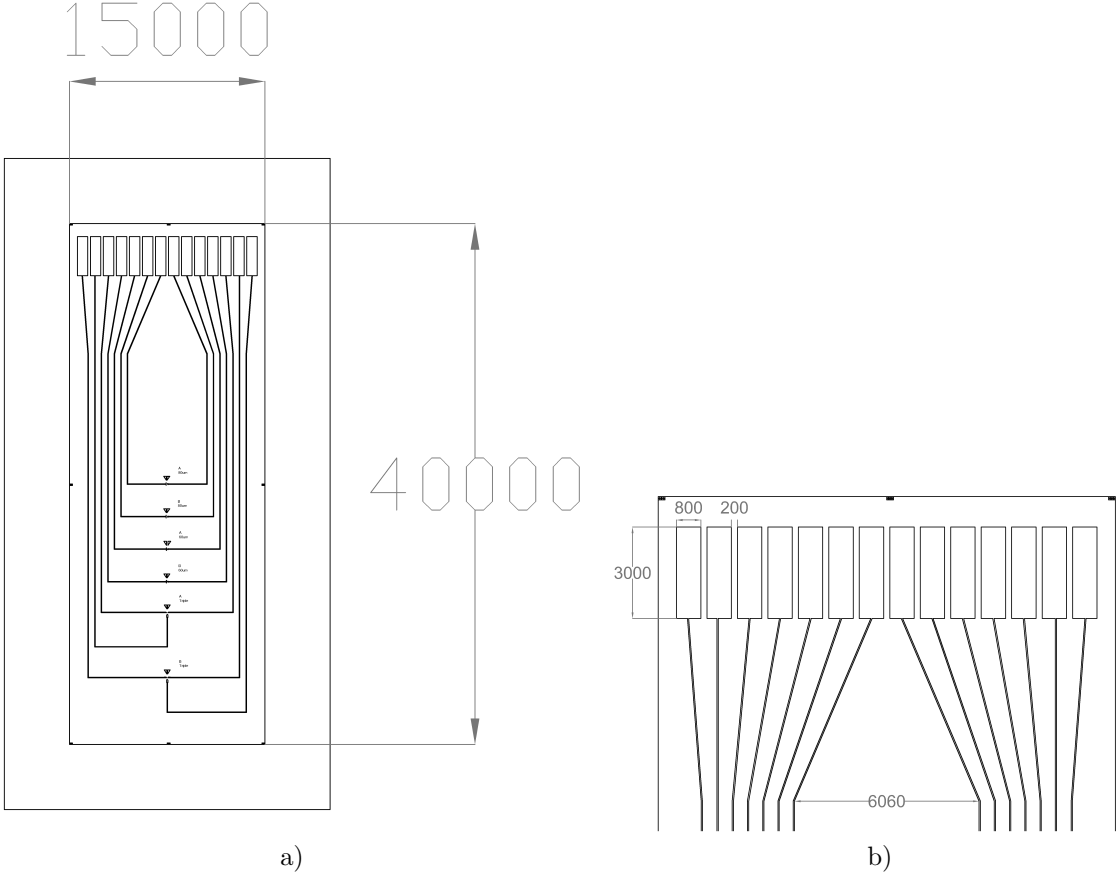
C.5.1 Overall View of First Electrode's Mask

Figure C.3: AutoCAD mask for the first TiW electrodes with simple geometry. b) Pads to wire bond with PCB.Dimensions in microns. Dimensions in microns.
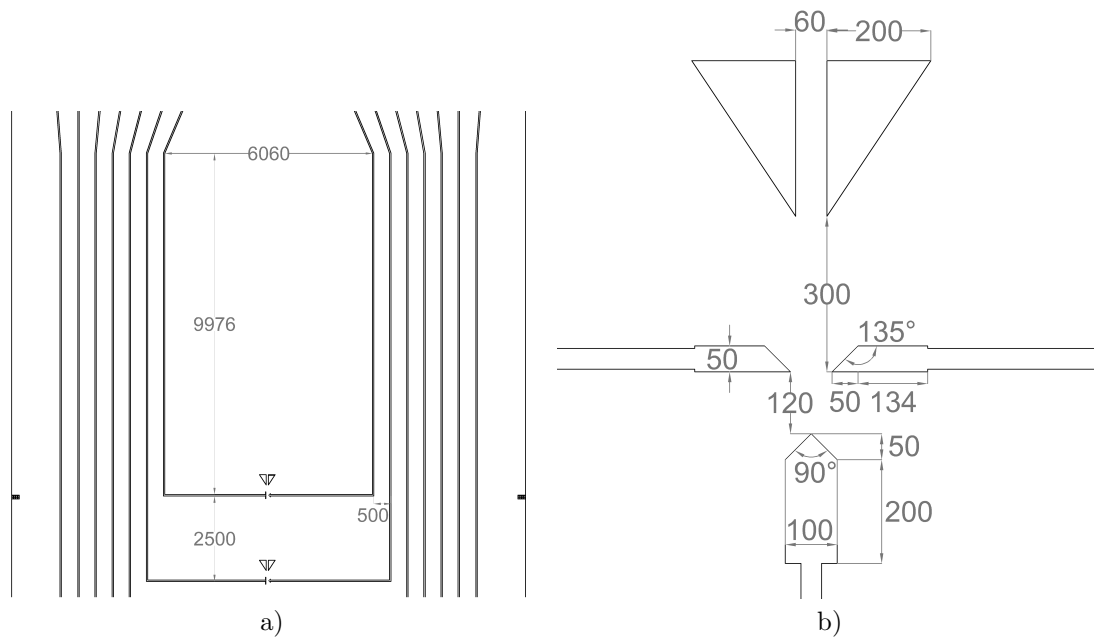
Figure C.4: a)Distance between high voltage lines that powers electrodes. b) Triple electrode design. Dimensions in microns.
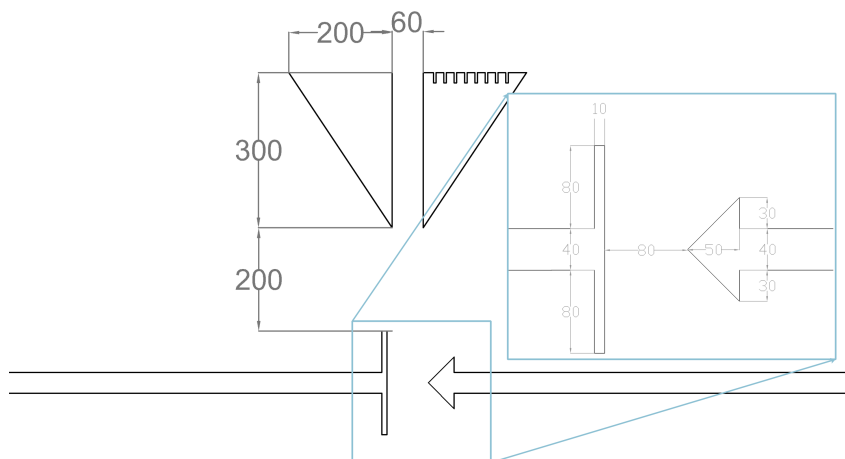

Figure C.5: AutoCAD mask for simple electrodes with alignment marks for microfluidic channels. Dimensions in microns.

C.5.2   Overall View of Second and Third Electrode's Masks

a)   b)
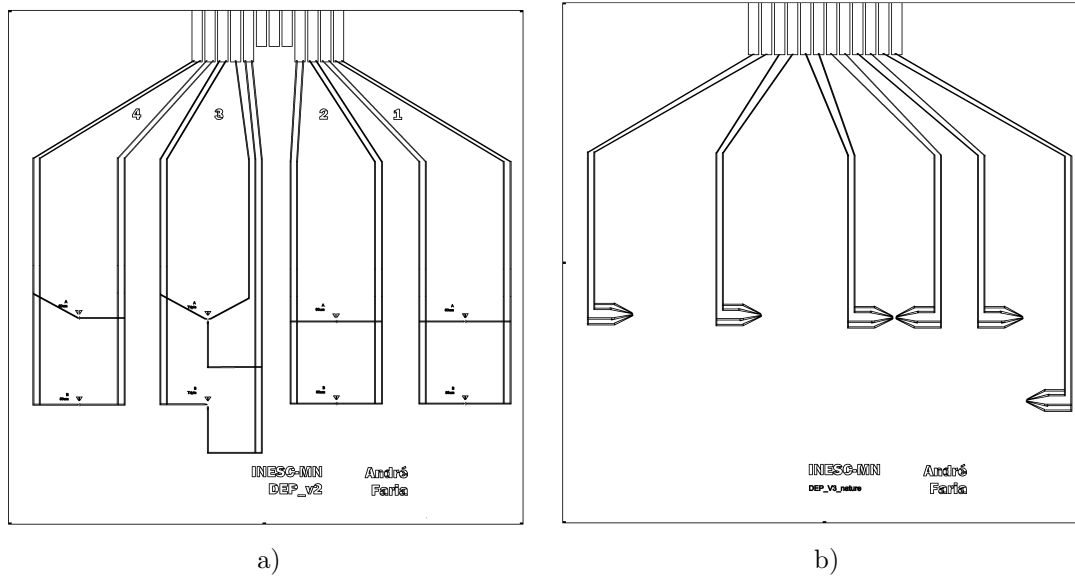
Figure C.6: Electrode AutoCAD masks for a) first, second geometries; and b) third geometries. Are inside a 4 cm × 4 cm square.

a)   b)
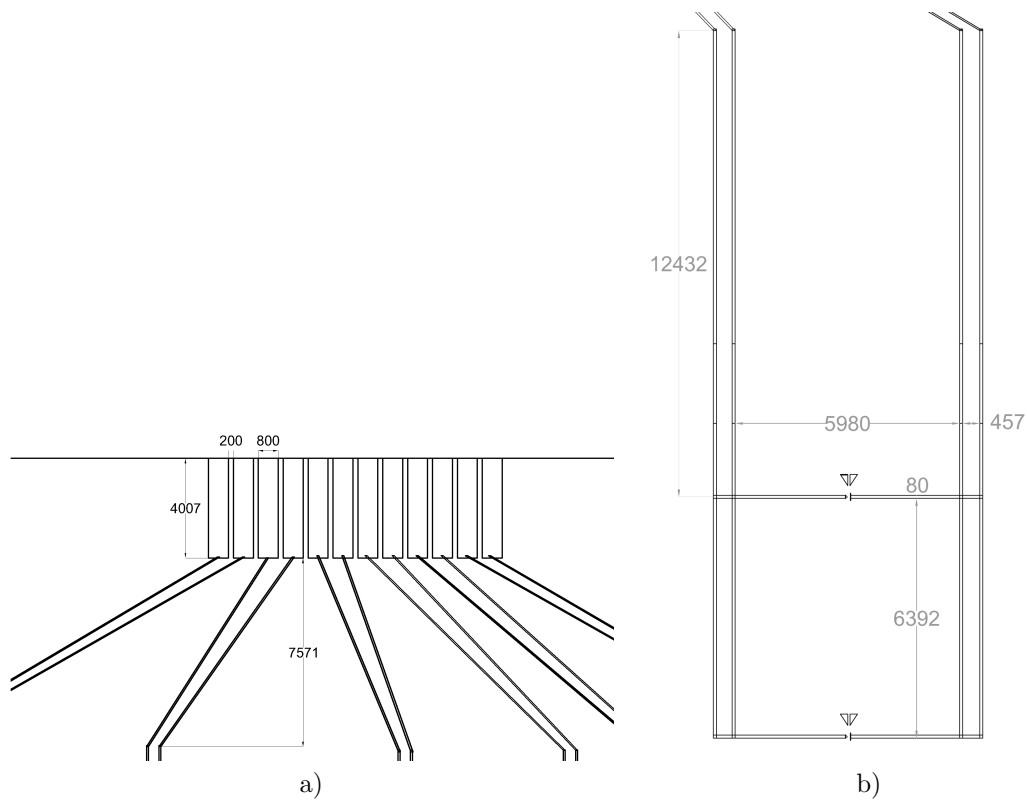
Figure C.7: a) Pads design for the masks in Figures C.6-a) and b). b) Double 80 μm lines and distances between electrodes and to pads. Dimensions in microns.
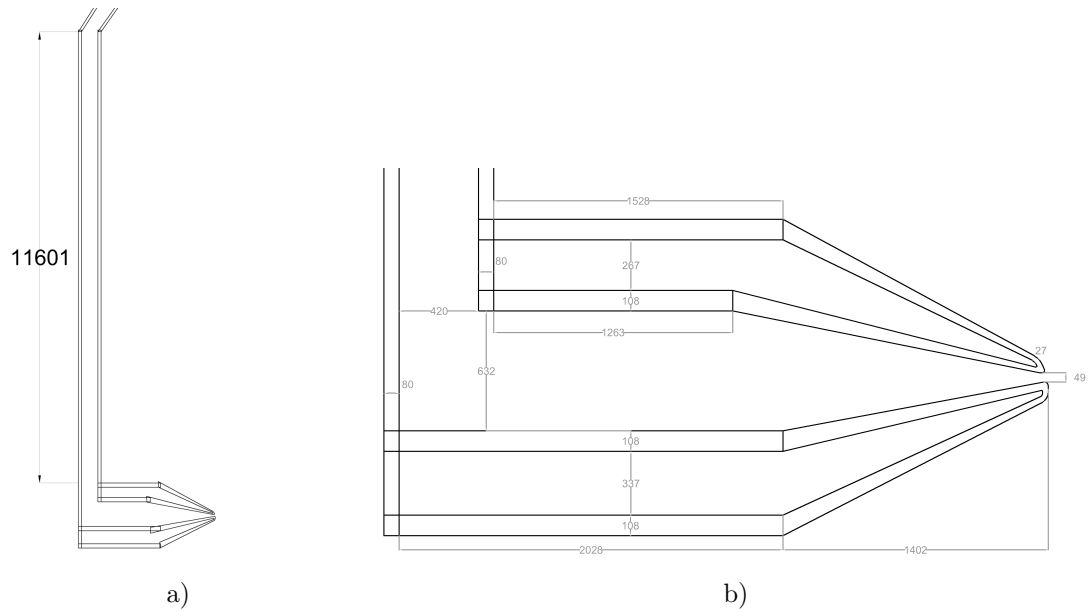
Figure C.8: a) Distance of parallel lines with high voltage for third planar electrodes geometry. b) Dimension of third geometry electrode. Dimensions in microns.

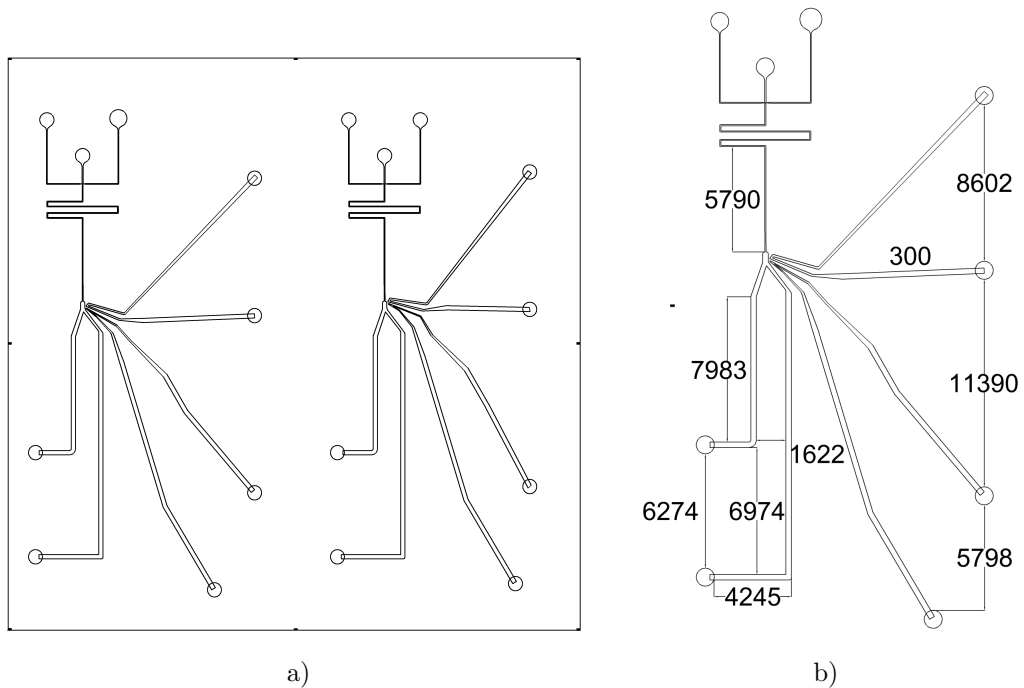## C.6   Overall View of New Mask Design and Design Iterations

Figure C.9: a) Overall view of final mask for sorting with liquid electrodes (on a 4 cm × 4 cm square). b) Some dimensions taken in account when designing the channels. Channels after bifurcation have 300 μm width. Dimensions in microns.
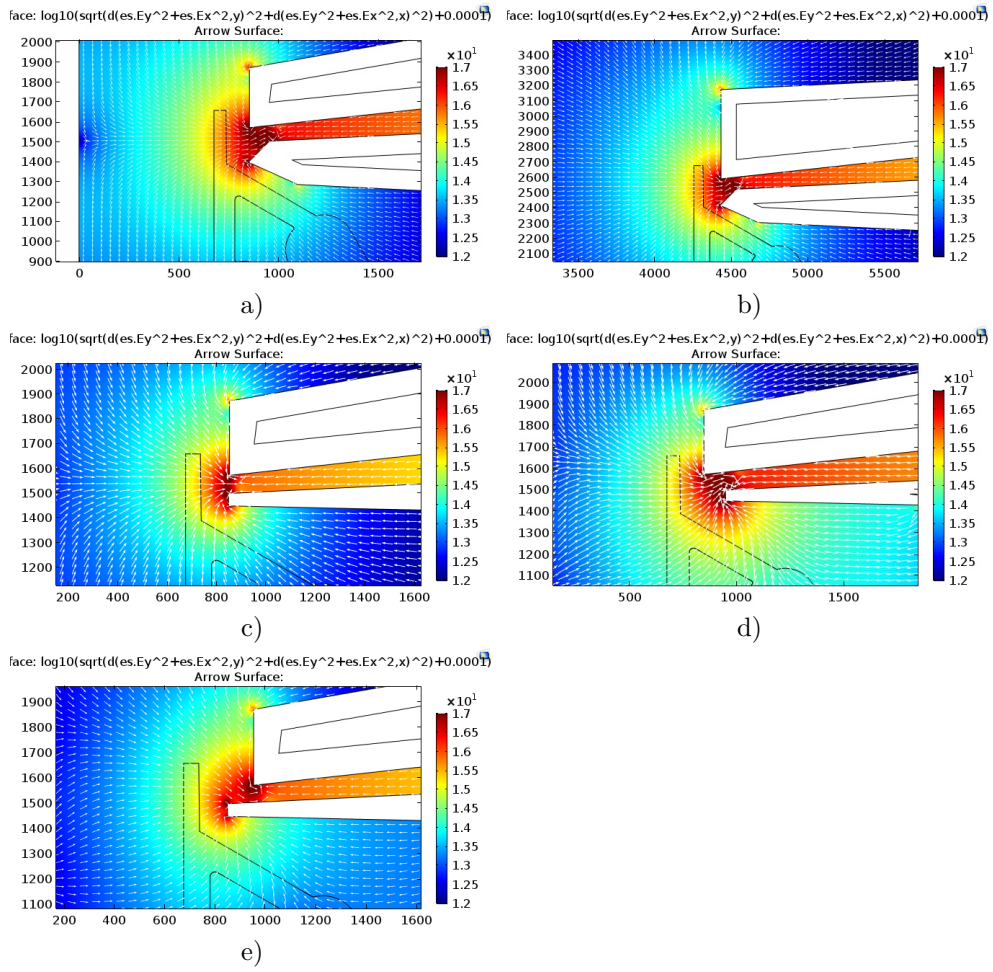
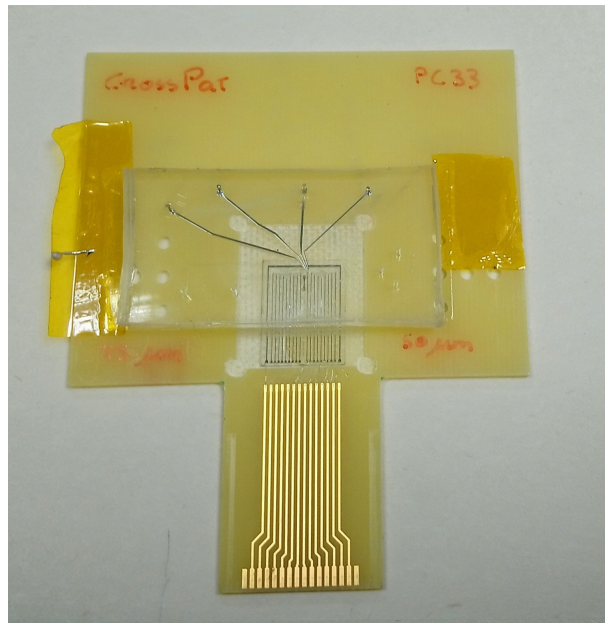Figure C.10: Iterative process till final sorting design with 3D electrodes.

Figure C.11: Microfluidic structures filled with liquid metal, aligned with photoconductors. Dimensions in microns.